

Development of an optical fiber probe for mercury detection

PhD Thesis

Javier Pérez Hernández

Supervisors

ICREA Professor Emilio Palomares Gil

Professor Xavier Correig Blanchar



UNIVERSITAT ROVIRA I VIRGILI

UNIVERSITAT ROVIRA I VIRGILI

DEVELOPMENT OF AN OPTICAL FIBER PROBE FOR MERCURY DETECTION

Javier Pérez Hernández

ISBN:978-84-691-9474-4/DL-T-2205-2008

UNIVERSITAT ROVIRA I VIRGILI
DEVELOPMENT OF AN OPTICAL FIBER PROBE FOR MERCURY DETECTION
Javier Pérez Hernández
ISBN:978-84-691-9474-4/DL-T-2205-2008

A mis padres

UNIVERSITAT ROVIRA I VIRGILI

DEVELOPMENT OF AN OPTICAL FIBER PROBE FOR MERCURY DETECTION

Javier Pérez Hernández

ISBN:978-84-691-9474-4/DL-T-2205-2008

*¿Qué podría atraerme de esta tierra,
salvo el deseo de quedarme?*

Imre Kertész, 1992

UNIVERSITAT ROVIRA I VIRGILI

DEVELOPMENT OF AN OPTICAL FIBER PROBE FOR MERCURY DETECTION

Javier Pérez Hernández

ISBN:978-84-691-9474-4/DL-T-2205-2008



UNIVERSITAT ROVIRA I VIRGILI

Departament d'Enginyeria Electrònica,
Elèctrica i Automàtica



Development of an optical fiber probe for mercury detection

Presented by Javier Pérez Hernández as a fulfillment of the
requirements for the Ph.D degree at Universitat Rovira i Virgili,
Tarragona, June 2008

UNIVERSITAT ROVIRA I VIRGILI

DEVELOPMENT OF AN OPTICAL FIBER PROBE FOR MERCURY DETECTION

Javier Pérez Hernández

ISBN:978-84-691-9474-4/DL-T-2205-2008



UNIVERSITAT ROVIRA I VIRGILI
Departament d'Enginyeria Electrònica, Elèctrica
i Automàtica



**INSTITUT CATALÀ D'INVESTIGACIÓ
QUÍMICA**

Prof. EMILIO PALOMARES GIL and Prof. **XAVIER CORREIG
BLANCHAR**, ICREA professor at the Institut Català d'Investigació
Química and Professor in the Departament d'Enginyeria Electrònica,
Elèctrica i Automàtica at Universitat Rovira i Virgili

CERTIFY:

The Doctoral Thesis entitled: “**DEVELOPMENT OF AN OPTICAL
FIBER PROBE FOR MERCURY DETECTION**”, presented by
JAVIER PÉREZ HERNÁNDEZ to receive the degree of Doctor of the
Rovira i Virgili University, has been carried out under our supervision, in
the Institut Català d'Investigació Química, and the results presented in
this Thesis were obtained in experiments conducted by the above
mentioned student.

Tarragona, May 2008

Dr. Emilio Palomares Gil

Dr. Xavier Correig Blanchar

UNIVERSITAT ROVIRA I VIRGILI

DEVELOPMENT OF AN OPTICAL FIBER PROBE FOR MERCURY DETECTION

Javier Pérez Hernández

ISBN:978-84-691-9474-4/DL-T-2205-2008

ACKNOWLEDGEMENTS

En primer lugar quiero dedicar un especial agradecimiento a Emilio Palomares en calidad de co-director de tesis y amigo. Gracias a él emprendí el viaje hacia Tarragona y me abrió las puertas al mundo de la química. Gracias Emilio por confiar en mí para este proyecto, dedicarme tu tiempo y buenos consejos, apoyarme en las decisiones y facilitarme todos los medios necesarios. Otro agradecimiento especial es para mi otro co-director de tesis Xavier Correig, gracias por creer en este proyecto desde el primer día, ofrecernos todos tus conocimientos en el área de sensores, que han sido imprescindibles para trazar la ruta que ha seguido esta investigación, y conciliar muchas veces entre conceptos del campo de la electrónica y la química.

Gracias a Eduard Llobet por tu colaboración en todo lo que concierne a la calibración multivariable, por guiarme en la planificación de los experimentos y la supervisión de los resultados.

Otra de las colaboraciones importantes se ha llevado a cabo en el Departamento de Ingeniería Eléctrica y Electrónica de la Universidad Pública de Navarra. Gracias a Patxi y Natxo por facilitarme vuestros conocimientos de sensores basados en fibra óptica y haberme guiado en todo el proceso de diseño y evaluación del dispositivo. Muchas gracias a los ‘Javieres’ Bravo y Goiko por explicarme con paciencia la manipulación de las fibras ópticas, y los almuerzos tan ricos que preparabáis. Mis dos estancias en Pamplona fueron de trabajo duro, pero

con lo bien que se come allí y el buen trato recibido, el esfuerzo es de sobra recompensado.

Un agradecimiento muy fuerte a Josep por su colaboración en este trabajo de investigación, aportando soporte y buenos consejos que me han ayudado a entender mejor la parte química. Puedo decir que el éxito de los logros de esta tesis no habrían sido posibles sin el apoyo de Josep.

A todos los compañeros de grupo, Amparo, Ana, Eugenia, Josep, Miquel, Ana, Toni, y a Eva, muchas gracias por mantener el buen ambiente de trabajo y por respetar mis momentos de concentración. Mikalet gracias por tus explicaciones doctas en las estructuras químicas, eres un fenómeno, y Toni, gran compañero de pedaleadas, te deseo que sigas con ese entusiasmo en tu trabajo de tesis.

Gracias a mis padres por haberme apoyado en todo momento. Y como no, gracias Ana por toda tu ayuda y apoyo que me has dedicado.

TABLE OF CONTENTS

ACKNOWLEDGMENTS	i
TABLE OF CONTENTS	iii
SUMARY	v
RESUMEN	viii
LIST OF ABBREVIATIONS	xii
1. INTRODUCTION	1
1.1 Background	2
1.2 Analytical methods for mercury detection	7
1.3 Aim of the work and thesis structure	8
1.4 References	10
2. OPTICAL CHEMICAL RECEPTORS FOR Hg²⁺ AND OTHER HEAVY METALS	13
2.1 Introduction to chemical sensors for heavy metals detection	14
2.1.1 <i>Electrochemical sensors</i>	18
2.1.2 <i>Mass-sensitive sensors</i>	25
2.2 Opto-chemical sensors	26
2.2.1 <i>Optical measurement techniques</i>	28
2.3 Optodes for heavy metal detection	37
2.4 Mercury detection with opto-chemical probes	48
2.4.1 <i>Chromogenic mercury detection</i>	50
2.4.2 <i>Fluorimetric mercury detection</i>	54
2.4.3 <i>Optical bio-detection of mercury</i>	65
2.4.4 <i>Optical mercury detection by advanced materials</i>	68
2.5 Colorimetric mercury determination by N719	74
2.6 References	79
3. MULTIVARIATE CALIBRATION: Hg²⁺ DETECTION AND THE ENHANCEMENT OF N719 SELECTIVITY	89
3.1 Introduction to multivariate calibration	90
3.1.1 <i>Partial least squares</i>	93
3.2 Enhancement techniques for multivariate linear regression	97
3.2.1 <i>Wavelet compression</i>	102
3.2.2 <i>Orthogonal signal correction</i>	104

3.2.3	<i>Variable selection</i>	105
3.2.4	<i>Genetic algorithms</i>	108
3.2.5	<i>Statistical feature selection (SFS)</i>	110
3.3	Selectivity enhancement and quantification of Hg ²⁺ with N719	113
3.3.1	<i>Study of interferences</i>	114
3.3.2	<i>Data sets</i>	119
3.3.3	<i>Pre-processing method adjustment</i>	122
3.3.4	<i>Results and discussion</i>	125
3.4	References	146
4.	IMMOBILIZATION OF THE MOLECULAR PROBE	149
4.1	Introduction to mesoporous metal oxide films	150
4.1	<i>Sol-gel method</i>	151
4.2	Optical support preparation and characterization	154
4.2.1	<i>Preparation of thin films</i>	155
4.2.2	<i>Physical characterization of Al₂O₃ films</i>	157
4.2.3	<i>N719 adsorption onto Al₂O₃ films</i>	165
4.2.4	<i>Stability of Al₂O₃ films</i>	167
4.2.5	<i>Sensitivity and detection limits</i>	171
4.2.6	<i>Response time</i>	174
4.2.7	<i>Temperature influence</i>	175
4.2.8	<i>Reversibility</i>	176
4.2.9	<i>Durability of the sensitized Al₂O₃ films</i>	178
4.3	N719/Al ₂ O ₃ film response characterization	179
4.3.1	<i>Data sets</i>	180
4.3.2	<i>Results and discussion</i>	183
4.4	References	188
5.	DEVELOPMENT OF THE OPTICAL FIBER MERCURY PROBE	189
5.1	Sensor operating principle	190
5.2	Optical fiber probe fabrication	197
5.3	Measurement set up	201
5.4	Results and discussion	202
5.4.1	<i>Working conditions</i>	203
5.4.2	<i>Reproducibility and multivariate calibration</i>	210
5.5	References	216
6.	CONCLUSIONS	219

SUMMARY

The organic form of mercury (*methylmercury*) is highly toxic, affecting the nervous system and even causing death. In the last years, human activities on coal combustion, waste incineration, gold mining and other industrial processes have raised the level of mercury in the atmosphere, rivers and other sources. Several public bodies have demonstrated that the direct detection of inorganic mercury (the precursor of *methylmercury*) will be beneficial in order to prevent mercury contamination. The detection of inorganic mercury through simple and low cost systems is possible by using colorimetric chemical sensors. Thus, several research groups worldwide have shown that the use of molecular probes, which change their optical properties upon the binding of inorganic mercury, is a promising topic for the development of detector devices for pollutant species.

This Thesis describes the most remarkable aspects in the development of an optical fiber probe designed for mercury determination in aqueous samples. The research arises from the discovery of a novel molecule (IUPAC name bis(2,2'-bipyridyl-4,4'-dicarboxylato) ruthenium(II) bis-tetrabutylammonium bis-thiocyanate) that upon mercury binding induces a color change from dark red-purple to orange in solution. The selectivity towards mercury of this ruthenium complex is high when compared to other known chemical reagents. Yet, in this work, we have been able to increase the selectivity through a fully multivariate calibration of the absorbance measurements. We have analyzed the mercury-containing

solutions under the co-existence of higher concentrations (19.5 mg L^{-1}) of other potential competitors such as Cd^{2+} , Pb^{2+} , Cu^{2+} and Zn^{2+} ions. Our experimental model is based on partial least squares (PLS) linear regression and other general techniques as wavelet, orthogonal signal correction, genetic algorithm and statistical feature selection that have been used to refine, *a priori*, the analytical data. In summary, we have demonstrated that the root mean square error of mercury prediction with statistical feature selection, as compared to the absence of pre-treatment, can be reduced from 10.5 to 5.2 percent, which improves the prediction ability of the calibration model by a factor of 2.

On the other hand, the possibility of working in solid-liquid phase increases the integration ability of the molecule in a device, making easier the measurement process. Nevertheless, the immobilization of the molecule onto a surface constitutes one of the challenges of this Thesis. Some preliminary works with the Ru(II) complex focussed on the immobilization of the molecule onto TiO_2 mesoporous thin films. However, some leaching problems were apparent when aqueous samples were analysed. Accordingly, we have improved the water stability of the molecule by anchoring the dye onto Al_2O_3 nanoparticles thin films treated with sulphuric acid. Moreover, the good optical properties of the alumina support allow a better transparency of the films, which translates in a higher amount of available spectral absorbance information.

A compact mercury read-out system has been achieved by coating an unclad optical fiber piece with Al_2O_3 paste. The proof-of-principle is

based on the optical changes of the reagent upon Hg^{2+} ions exposure, which modulates the light intensity transmitted through the optical core. There are many theoretical studies that explore a particular research case of the evanescent optical fibers. As the alumina cladding has higher refractive index than the core, both evanescent field and radiative mode may appear in the modified cladding. This Thesis exposes a brief explanation of this behavior in order to understand the mechanisms of the response of our mercury optical fiber probe. Moreover, several experiments have been carried out in mercury aqueous samples so as to find the proper working conditions, such as the optimum dye concentration adsorbed onto the alumina cladding, which has a great effect on the device performance. Finally, mercury quantification has been possible through multivariate calibration, direct partial least squares being the most robust procedure if we take into account the fact that the response of this kind of optical probes varies significantly from one to another. A root mean square error for mercury predictions of 11.5 percent has been achieved within a range from 0 to 6 mg L^{-1} of Hg^{2+} ions. Overall, this thesis work has illustrated all the steps that come into play in the design of an optical fiber chemical-based probe, providing a simplified measurement process and a lower cost if it is compared to traditional analysis equipment. As far as the author is concerned, an optical fiber probe for mercury determination is presented for the first time.

RESUMEN

El mercurio en su forma orgánica (metilmercurio) presenta una alta toxicidad, afectando al sistema nervioso e incluso pudiendo causar la muerte. En los últimos años, las actividades humanas basadas en la combustión de carbón, incineración de residuos, minería del oro y otros procesos industriales han aumentado el nivel de mercurio en la atmósfera, ríos y otras fuentes. Distintas organizaciones públicas han demostrado que la detección directa del mercurio inorgánico (precursor del metilmercurio) puede ser beneficiosa para la prevención de la contaminación de mercurio. La detección del mercurio inorgánico a través de sistemas simples y de bajo coste es posible gracias al empleo de sensores químicos colorimétricos. Por lo tanto, distintos grupos de investigación de todo el mundo han demostrado que el uso de sondas moleculares, las cuales cambian sus propiedades ópticas ante la interacción con el mercurio inorgánico, constituye un hecho prometedor para el desarrollo de dispositivos detectores de especies contaminantes.

Esta Tesis describe los aspectos más relevantes en el desarrollo de una sonda de fibra óptica diseñada para la determinación de mercurio en muestras acuosas. La investigación se plantea a partir del descubrimiento de una reciente molécula (bis(2,2'-bipyridyl-4,4'-dicarboxylato) ruthenium(II) bis-tetrabutylammonium bis-thiocyanate) que ante la interacción con el mercurio presenta un cambio de color desde un rojo púrpura oscuro hasta el naranja en solución. La selectividad hacia el mercurio de este complejo de rutenio es alta si se compara con otros

reactivos químicos conocidos. Es más, en este trabajo, hemos podido incrementar la selectividad a través de una calibración multivariable aplicada a las medidas de absorbancia. Hemos analizado soluciones que contienen mercurio bajo la presencia de concentraciones altas (19 mg L^{-1}) de otros competidores potenciales como son los iones de Cd^{2+} , Pb^{2+} , Cu^{2+} y Zn^{2+} . Nuestro modelo experimental está basado en la regresión lineal por mínimos cuadrados parciales (siglas en inglés PLS) junto con otras técnicas generales como wavelet, corrección ortogonal de la señal, algoritmo genético y selección de características estadísticas que han sido empleadas para refinar, a priori, los datos analíticos. En resumen, hemos demostrado que el error cuadrático medio de la predicción de mercurio con la selección de características estadísticas en comparación con la ausencia de pre-tratamiento, puede reducir del 10.5 al 5.2 por ciento, mejorando la habilidad del modelo de calibración en la predicción por un factor de 2.

Por otro lado, la posibilidad de trabajar en fase sólido-líquido incrementa la capacidad de integrar la molécula en un dispositivo, facilitando de este modo el proceso de medición. Sin embargo, la inmovilización de la molécula sobre una superficie constituye uno de los retos de esta Tesis. Trabajos preliminares con el complejo de Ru(II) se centraron en la inmovilización de la molécula sobre capas finas mesoporosas de TiO_2 . No obstante, las pérdidas del colorante son apreciables cuando se analizan muestras acuosas. Por consiguiente, hemos mejorado la estabilidad acuosa de la molécula anclando el colorante sobre capas finas

formadas por nanopartículas de Al_2O_3 tratadas con ácido sulfúrico. Además, las buenas propiedades ópticas del soporte de alumina permiten una mayor transparencia de los films, lo que se traslada en mayor información de absorbancia espectral disponible.

Se ha logrado un sistema compacto de detección instantánea cubriendo el núcleo de un trozo de fibra óptica con pasta de Al_2O_3 . El principio de funcionamiento se basa en los cambios ópticos del reactivo ante la exposición a iones de Hg^{2+} , modulando así la intensidad de luz que se transmite a través del núcleo óptico. Existen muchos estudios teóricos que exploran un caso particular de investigación de las fibras ópticas evanescentes. Al tener la cubierta de alumina mayor índice de refracción que el índice del núcleo, tanto el campo evanescente como el modo de radiación pueden aparecer la cubierta modificada. De manera que se puedan entender los mecanismos de la respuesta de nuestra sonda de mercurio basada en fibra óptica, la presente Tesis expone una breve explicación a dicho comportamiento. Además, varios experimentos se han llevado a cabo con muestras de mercurio acuosas con el fin de determinar las condiciones de trabajo, como la concentración óptima de colorante adsorbido sobre la cubierta de alumina, la cual tiene un efecto significativo sobre el funcionamiento del dispositivo. Finalmente, si tenemos en cuenta que la respuesta de este tipo de sondas ópticas varía significativamente de sonda a sonda, la cuantificación de mercurio ha sido posible a través de la calibración multivariable, siendo el método directo de mínimos cuadrados parciales el procedimiento más robusto.

De este modo, se ha conseguido un error cuadrático medio en la predicción de mercurio de un 11.5 por ciento, considerando un rango de 0 a 6 mg L⁻¹ de iones de Hg²⁺. En general, este trabajo de tesis ha ilustrado todos los pasos que conciernen al diseño de una sonda de fibra óptica, proporcionando un proceso de medida simplificado de bajo coste si se compara con el equipamiento de análisis tradicional. En lo referente al autor, este es el primer dispositivo con configuración de fibra óptica evanescente destinado a la determinación de mercurio en medio acuoso.

LIST OF ABBREVIATIONS

AAS	Absortion spectroscopy
AFM	Atomic force microscope
AFM	Atomic force microscope
ANFIS	Adaptative neuro-fuzzy inference systems
ASV	Anodic stripping voltametry
AuNPs	Gold nanoparticles
BET	Brunauer.Emmett-Teller
B-Rb	Britton Robinson
CCD	Charge-coupled device
ChemFET	Chemical-sensing field effect transistor
CMOS	Metal-oxide-semiconductor
CVD	Cold vapour deposition
DBET	Diameter of average particle size from BET
DF	Discrimination function
Dihizone	1,5-Diphenylthiocarbazone
DMF	Dimethylformamide
DNA	Deoxyribonucleic acid
EPA	Environmental Protection Agency
FET	Field effect transistor
FIA	Flow injection analysis
FIR	Finite impulse response
FTIR	Fourier transform infrared
FTIR	Fourier transform infrared
GA	Genetic algorithm
GLRS	Grating light reflection spectroscopy
HEMT	Electron mobility transistor
HEPES	4-(2-hydroxyethyl)-1-piperazineethanesulfonic acid
HOMO	Higher occupied molecular orbital

ICP-AES	Inductively coupled plasma atomic emission spectroscopy
ICP-MS	Inductively coupled plasma atomic mass spectroscopy
IIR	Infinite impulse response
INLR	Implicit non linear
IR	Infrared
ISFET	Ion selective field effect transistor
IUPAC	International Union of Pure and Applied Chemistry
LED	Light-emitting diode
LOD	Limit of detection
MEMS	Micro-electromechanical systems
MICT	Metal-induced intramolecular charge transfer
MTZ	2-mercapto-2-thiazoline
N719	bis(2,2'-bipyridyl-4,4'-dicarboxylato) ruthenium(II) bis-tetrabutylammonium bis-thiocyanate
NIR	Near infrared
OLED	Organic light-emitting diode
OSC	Orthogonal signal correction
PCA	Principal component analysis
PCR	Principal components regression
PLS	Partial least squares
PV	Polyvinyl chloride
PVC	Polyvinyl chloride
Q	Expression of the predicted cross-validated variance
QCM	Quartz crystal microbalance
QPLS	Quadratic PLS
REDOX	Reduction-oxidation
RMSEC	Root mean square error of calibration
RMSECV	Root mean square error of cross-validation
RMSEP	Root mean square error of prediction

RR	Ridge regression
SAW	Surface acoustic wave
SBET	Superficial area of particles from BET
SERS	Surface-enhanced Raman spectroscopy
SFS	Statistical feature selection
SMA	Subminiature A
SPR	Surface plasmon resonance
SWSV	Square wave stripping voltametry
TAN	1-(2-thiazolylazo)-2-naphtol
TAR	4-(2-thiazolylazo) resorcinol
TEM	Transmission electron microscopy
TEOS	Tetraorthoethylsilicate
THF	Tetrahydrofuran
TMAC	N-trimethoxysilylpropyl-N,N,N-trimethylammonium chloride
TPEN	(N,N,N',N'-Tetrakis-(2-pyridylmethyl) ethylenediamine)
TPPS	5,10,15,20-tetraphenylporphinetetrasulfonic acid ⁶⁸
TSM	Thickness shear mode
TXRF	Total reflection x-ray fluorometry
UV	Ultra visible
WHO	World Health Organization
XAD-4	Styrene divinylbenzene cross-linked copolymer
XRD	X-ray diffraction



1 Introduction

CONTENTS

- 1. 1 Background
- 1. 2 Analytical methods for mercury detection
- 1. 3 Aim of the work and thesis structure
- 1. 4 References

1.1 Background

Mercury has significant adverse effects on human health and wildlife. Mercury is toxic and it bio-accumulates on basic nutrients that appear at the base of the food pyramid and, hence, will be ingested later on by humans. In most global regions mercury is present in a wide variety of environments (water, soil, and aquatic biota). During the pre-industrial era, the problem was restricted to a limited number of sources of severe pollution, such as the carbon industry or mining wastes as well as natural sources such as the volcanic activity. But during last century mercury emissions have spread widely in the atmosphere and have lead to the formation of mercury deposits on the earth's surface inducing the contamination of aqueous systems (rivers, lakes etc...). As mentioned before, mercury is also emitted by natural sources: volcanoes, geothermal sources, geologic deposits, and the ocean. But, during the last 150 years, human activities have far doubled natural amounts of mercury in the atmosphere, this pollution being primarily released through coal combustion and waste incineration processes¹. Moreover, localised contamination also occurs through small-scale gold mining and other industrial processes. In addition, medical waste incinerators may have been responsible for as much as 10% of all mercury releases, being the greatest source of non-industrialized mercury vapour, around 53% including dental amalgam and laboratory medical devices². Recently, the European Union has announced the prohibition to manufacture mercury

thermometers, which represents the 1% of the total mercury production. Figure 1.1 depicts the relative contribution of the different emissions caused by human activity.

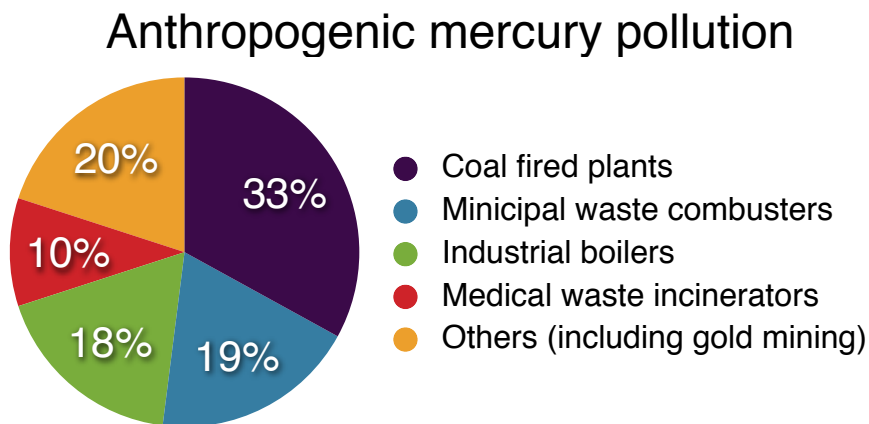


Figure 1.1. Mercury emissions caused by human activity.

Many industrial processes can release elementary mercury vapours, which are easily transported in the atmosphere. A part of this mercury emission is oxidized to Hg^{2+} and deposited in the soil, waters and accumulated in biota. A fraction of this Hg^{2+} is reduced to Hg^0 by microorganisms, including algae and cyanobacteria, and released back to the atmosphere. But the inorganic mercury that resides in underwater sediments can be converted to methylmercury or other organomercurial derivates. A microbial process that is controlled by certain bacteria, such as prokaryotes, and enhanced by organic matter and oxygen is responsible of the methylmercury formation. An illustration of the mercury emission process can be seen in Figure 1.2. Inorganic mercury is

generally poorly absorbed by the digestive track and therefore does not represent a high risk for humans. However, the real threat is its organic form, methylmercury. In fact, more than 95% of all mercury in fish is methylmercury, which is bioaccumulated when fishes eat aquatic plants or other fish. Moreover, the methylmercury can be encountered in other predators at high concentrations at the top of the food chain, like tuna fish.

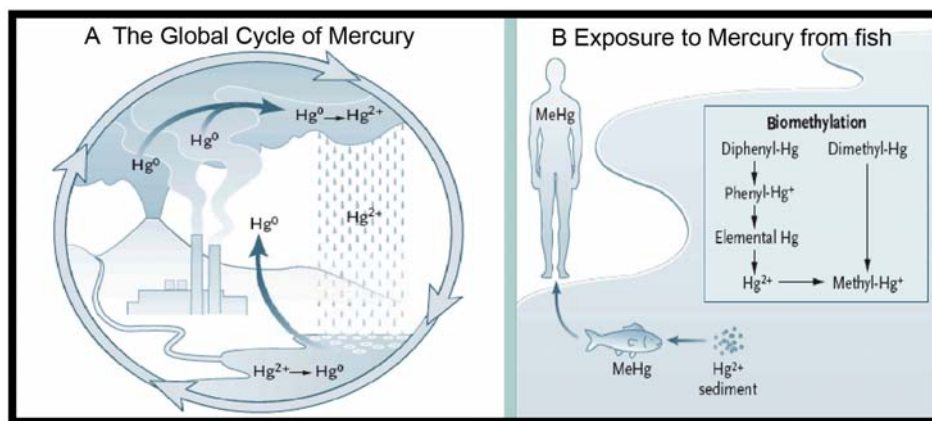


Figure. 1.2 The mercury emission process (A) and how the methylmercury is introduced into the food chain.

When adsorbed or ingested methylmercury provokes several adverse health effects as: tremors, impaired vision and hearing, paralysis, insomnia, emotional instability, development deficits during fetal development and attention deficit and slow development during childhood. The most infamous contamination occurred in 1950s in Japan. It is worldwide known as 'Minimata disease' and affected the towns of

Kumamoto, Kagoshima and Niigata, wherein about 3,000 people were contaminated. The pandemia was the result of the environmental pollution due industrial activities and the release of methylmercury on the harbour, where the people was fishing. As a consequence of the contamination, a congenital disease occurred. The congenital disease multiplied malformations in new born children whose mothers were exposed to methylmercury during pregnancy³.

The studies about mercury and its effects on the environment have increased in last years. It is readily available sufficient information related to the toxicity of mercury and the governments should pay attention to its potential risk. There are several studies of the effects of mercury exposure in children⁴, in blood and urine, and also for cadmium and lead⁵, as well as mercury contamination in fish, from gold mining areas⁶, etc...

As an example, the European countries have detected high mercury concentrations in fish, specially, in 11 marine species usually found in food. In Spain it is not difficult to find a contaminated fish in the supermarket with 1ppm of mercury per gram. The European Union is the main mercury provider in the world, as an example Spain closed Almaden in 2003 the biggest mercury mine, which still has wide areas of contaminated soil. Herein, the risk is due to the mercury accumulation in terrestrial plants and animals, and thus its incorporation into the human food chain⁷.

A recent United Nations report on the global distribution of mercury⁸ concluded that there is a definite need to improve the measurement of mercury in the environment, in fish and sea mammals, and in humans. Hence, there are potential applications where a simplified method to detect mercury could be addressed for, as an example, detection of mercury from coal burning power stations, testing water supplies for mercury, personal dosimeters and laboratory equipment, detection of mercury in fish and screening regional populations for mercury contamination. In Figure 1.3 we illustrate the requirements for the different analytical samples.

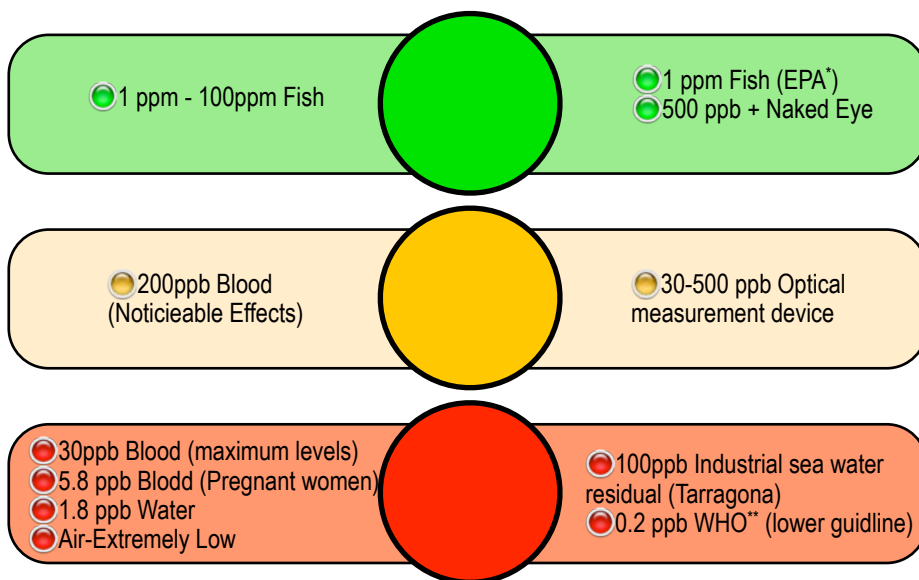


Figure 1.3. Some of the mercury levels and the required measurement sensitivity depending on the application.

1.2 Analytical Methods For Mercury Detection

There are several laboratory methods capable to determine heavy metals at very low concentrations, indeed some of them have a limit of detection in the order of parts per trillion. Many of the recommended procedures for the detection of heavy metals are photometric methods: atomic absorption spectroscopy (AAS), inductively coupled plasma atomic emission spectroscopy or mass spectrometry (ICP-AES, ICP-MS), total reflexion X-Ray fluorometry (TXRF). Apart from these, other techniques are anodic stripping voltametry (ASV), polarography and energy dispersive analysis via X-rays (EDAX). AAS is recommended by many protocols for mercury detection and the most representative apparatus is the mercury spectrometer RA-915⁺⁹. The advantages of all these equipments, apart from the high sensitivity, are the capacity to measure over many different types of samples (soils, liquids, gas), and some of them allow the multi-trace analyte. On the other hand, these equipments, generally determine only total metal concentration, and are not specific for the analyte of interest. Thus, some of them require sample pre-concentration and extraction procedure and this is time consuming and a potential source of error.

1.3 Aim Of The Work And Thesis Structure

Given the importance of the effects caused by mercury and its derivatives to humans, the motivation grows towards the design of new tools that are useful for the mercury detection in contaminated water. Moreover, the high cost and the voluminosity of the traditional laboratory equipment are some of the disadvantages for many applications, specially for those where the cost and field measurement are driving factors. The emerging technologies and new advances in the materials field make it possible to develop chemical sensors as a new tool for the detection of a variety of toxic species, and as an alternative device for on-line and field monitoring of compounds of interest. Accordingly, the starting point of this present thesis work arises from the recent discovery at Emilio Palomares group of a Ru(II) derivative which signals the presence of mercury by a color change. The selectivity of this chromogenic reagent is high if it is compared with the most known mercury molecular probes. However, there is still the challenge to improve the sensitivity of the molecular probe even in the presence of other metal ions. One of the objectives of this Thesis is to explore whether multivariate calibration coupled to some appropriate pre-treatment techniques can lead to an improvement in the quantification analysis of mercury. Another good features of this molecule is its capability to anchor to metal oxide films, which is one of the most important aspects towards the design of a

measurement device. Initial experiments showed the mercury detection through dyed mesoporous TiO₂ films, but leaching problems limited the mercury analysis to organic samples. We were therefore interested in extending the mercury detection to aqueous samples, for example by testing an alternative molecular support. A final system combining a good water stability and an optimal mercury response would make it possible to integrate it into a compact read-out system. In this context, the optical fiber-based technology constitutes the most exploited platform for chemical sensors, due to the low optical losses, immunity to electromagnetic interference, and manipulation easiness. Moreover, the few existing examples of evanescent optical fiber sensors for heavy metal detection promotes the exploration of this kind of topology in our device design. Therefore, we aim to obtain an optical fiber probe for mercury detection. The main issues of this Thesis are described in the following five chapters:

- ▶ Chapter 2 focuses on the introduction to chemical sensors. We explain the mechanisms of reaction, types of indicators and some examples of chemical sensors for heavy metal detection, in particular those based on optical detection.
- ▶ Chapter 3 affords a fully spectral characterization of the molecular probe studied in the Thesis: the Ruthenium complex N719. For this purpose, a multivariate model based on partial least squares is designed for the absorbance measurements, with

the aim of reducing the interference effects caused by other metal ions, even making possible the quantification of mercury in this case.

- ▶ In Chapter 4 we describe the work on the solid support. Working on solid state is possible by the immobilization of the reagent onto a mesoporous alumina film. A physical characterization of the Al₂O₃ nanoparticles is presented, followed by the analysis of the full response when mercury is present.
- ▶ Chapter 5 describes the design of an optical fiber probe, which integrates the sensitive films in a custom readout system for mercury detection. Some aspects of the operating principle and parameters design are discussed, as well as the fabrication procedure and the spectral response as a consequence of the optical changes induced by Hg²⁺ ions.
- ▶ Chapter 6 presents the conclusions and perspectives of the present work from the results shown in the previous chapters.

1.4 References

- (1) Brighman, M. E.; Krabbenhoft, D. P.; Hamilton, P. A. In *Fact Sheet*; U.S. Geological Survey, 2003.
- (2) In *WHO/SDE/WSH/05.08*; Department of Protection of the Human Environment; World Health Organization: Switzerland, 2005.

- (3) Honda, S. i.; Hylander, L.; Sakamoto, M. *Environmental Health and Preventive Medicine* **2006**, *11*.
- (4) Counter, A. S.; Buchanan, L. H. *Toxicology and Applied Pharmacology* **2004**, *198*.
- (5) Batariova, A.; Specvackova, V.; Benes, B.; Cejchanova, M.; Smid, J.; Cerna, M. *International Journal of Hygiene and Environmental Health* **2006**, *209*, 359.
- (6) Castilhos, Z. C.; Rodrigues-Filho, S.; Rodrigues, A. P.; Villas-Boas, R. C.; Siegel, S.; Veiga, M. M.; Beinhoff, C. *Science of the Total Environment* **2006**, *368*.
- (7) Molina, J. A.; Oyarzun, R.; Esbrí, J. M.; Higuera, P. *Environ Geochem Health* **2006**, *28*.
- (8) United Nations Environment Programme: Global Assessment of Mercury. UNEP Chemicals. Geneva, Switzerland, 2002.
- (9) Sholupov, S.; Pogarev, S.; Ryzhov, V.; Mashyanov, N.; Stroganov, A. *Fuel Processing Technology* **2004**, *85*, 473-485.

UNIVERSITAT ROVIRA I VIRGILI

DEVELOPMENT OF AN OPTICAL FIBER PROBE FOR MERCURY DETECTION

Javier Pérez Hernández

ISBN: 978-84-1291-912-9 *Development of an optical fiber probe for mercury detection*



2 Optical Chemical Receptors For Hg²⁺ And Heavy Metals Detection

CONTENTS

- 2. 1 Introduction to chemical sensors for heavy metals detection
- 2. 2 Opto-chemical sensors
- 2. 3 Optodes for heavy metals detection
- 2. 4 Mercury detection with opto-chemical probes
- 2. 5 Colorimetric mercury determination by N719
- 2. 6 References

2.1 Introduction To Chemical Sensors For Heavy Metals Detection

Recently, the advances in optoelectronic devices (light sources and detectors), microfluidics and arrays as well as microfabrication have reinforced the research in the field of chemical sensors. In general, the analyte, in our case heavy metals, can be directly or indirectly detected by a sensitive material (molecule, functionalized film, etc...). The direct detection refers to the monitoring of an intrinsic property of the analyte, such as, for example, absorption, luminescence, or mass that changes upon the binding of the analyte. On the other hand, the indirect detection is focused on the changes (optical, electrical, etc...) which are promoted by the use of an intermediate material, molecule or substrate, when the analyte is present, see Figure 2.1.

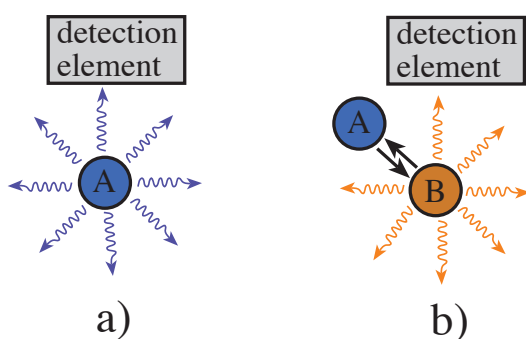


Figure 2.1. a) Representation of direct detection, wherein the analytical signal is inherent to the analyte A. b) It is called indirect detection when an intermediate material or reagent B is used for signaling the presence of analytes.

In most papers, the term sensor is inadequately used to refer a (molecular) probe or an indicator. Similarly, classical *chromoionophores*

are called *ion sensors*, and the common screening analyte technique is now referred as '*sensing*'. Hence, we believe that a definition of the terminology used is needed to overcome ambiguity. A well-established definition of sensor referred by Wolfbeis¹ could be the most appropriate: "*Chemical sensors are miniaturized devices that can deliver real-time and on-line information on the presence of specific compounds or ions in even complex samples*". This definition is close to what was described by Saliterman²: "*an ideal sensor operates continuously and without affecting the measurement, has appropriate sensitivity, is fast and with a predictable response (linear or non linear), has fully reversible behaviour, high reliability, selectivity, compactness, high signal-to-noise ratio, immunity to environmental conditions, and is easy to calibrate.*"

Fundamentally, the general characteristics that compose a sensor are:

1. Interaction with the analyte, which can be physical or chemical.
2. Transduction mechanism that converts this reaction into a readable signal (mainly optical or electrical).
3. Signal processing, which can include the signal conditioning (amplifying, filtering, etc.) to the proper values for a digital conversion, and a digital treatment for enhancing the analytical information.
4. Signal interpretation, which delivers the concentration of the analyte.

As used herein, those transducers, which do not follow the Saliterman definition will be considered as *probes*. Additionally, we refer as a molecular probe to a chemical powder which can be used as a sensitive reagent. The desired requirements that a molecular probe must fulfil to be a suitable sensor are: (a) high sensitivity traduced as a large change in the analytical signal caused by small concentration of analyte; (b) high specificity in order to distinguish the specie of interest; (c) excellent long term stability and reversibility. Fulfilling all these demands is possible, but most molecular probes still show several drawbacks including: insufficient long-term stability, interference of other species than the target and inadequate limit of detection. Yet advances in measurement systems and signal processing can overcome these disadvantages. As an example, the selectivity standards required can be solved by using pattern recognition methods as in the case of electronic nose and tongues³, wherein several molecules are disposed as an array of sensors with different partial responses to an analyte in such a way that, the cross response of all indicators serve as inputs for a multi-way modelling⁴. On the other hand, many of the currently available micro-fabrication tools (screen printing, cold vapor deposition (CVD), etc...) are applicable in the chemical sensor field, thus making a low cost mass production possible. In this case, if the manufacture of the opto-chemical transducer is low-cost, a modular design can lead to devices with easily interchangeable receptor modulus, which can advantageously be used in applications where the regeneration of the chemical probe is not possible

or where a remote monitoring is not necessary. Due to the growing demand of low-cost and hand held analytical systems, a proper application can be found for the use of the chemical sensors even with their initial limitations.

Actually, the use of chemical sensor has a wide range of applications. The measurement parameters can be molecules⁵, ions^{6, 7}, pH⁸⁻¹², and even temperature^{13, 14}. Moreover, there are chemical sensors suitable to work in gas, vapour or liquid phase. In this section we will only focus on chemical sensors that are used in liquid samples and, furthermore, with examples of heavy metal detection. Additionally, the difference from conventional analytical techniques as TXRF, AAS, etc... relies on a high degree in integration leading to handheld and low cost devices. It is important to remark, that the biosensor field may overlap with chemical sensors from several points of views. For example, the transduction can also lead in an optical or electrical signal, and many of the transduction schemes can either applied to biosensors or chemical sensors. Herein, this work is focused on chemical sensing, however, some examples of biosensors will be discussed if they are relevant for the work.

Basically, the operating principle of the chemical sensor can be: electrochemical, mass-sensitive sensors, and optical¹⁵.

2.1.1 Electrochemical sensors

The first devices that incorporated the concept of chemical sensor as the sensing mechanism to determine the presence of heavy metals were electrochemical. In this case, when the analyte reacts with the target material or solution a charge transport is produced. These electrical changes can be directly observed with the electrodes immersed in the solution under test or can be obtained by the interaction of a sensitive material with the analyte. Depending on the sensing mechanism the electrochemical sensors can be classified as potentiometric, conductimetric and voltammetric. Potentiometric sensors measure the potential difference between the working electrode and the reference electrode. Conductimetric sensors are based on the changes of electrical properties between electrodes, and these can be resistive or capacitive. Voltammetric sensors refer to the measurement current that results from the application of potential (amperometric detection) between the working electrode and the solution.

The miniaturized version of the electrochemical detection emerged with functionalized materials that allowed working in solid state. Moreover, a high degree in integration is achieved by incorporating the field effect transistor (FET) concept to the electrochemical sensing. The first examples of chemical-sensing field effect transistors (ChemFETs) appears in the seventies decade¹⁶. Basically, it consists in a functionalized membrane with electrodes that provides impedance measurements.

Normally, the thin film is deposited on a silicon substrate bringing the possibility of being integrated with electronic circuits in the same chip.

Electrochemical sensors are widely used in gas sensing, but ChemFETs are suitable for liquid measurements. Furthermore, the advances in the complementary metal-oxide-semiconductors (CMOS) technology have led into micrometer-sized transducers. Obviously, the measurements in liquids impose some restriction because the circuit part needs to be protected from any liquid but the sensing face must be in contact with the solution under test. But combining CMOS and micro-electromechanical systems (MEMS) technologies permits to develop a system on chip that incorporates the sensor with micro-fluidics part, amplifier, signal processing and microcontroller.

Next, some examples of electrochemical sensors for heavy metal detection are commented. For example, a method for amperometric detection of mercury is based on flow injection analysis (FIA), which is an alternative to the traditional instrumental methods at a lower cost. Handheld equipment is also possible with this technique. Detection of mercury vapour dissolved in aqueous solutions can offer detection limits below sub-ppb¹⁷. On the other hand, sample preparation and mercury reduction is necessary, and the measurement is influenced by the presence of other metal ions. Similarly, the potentiometric detection based on ion-selective electrodes offers simple instrumentation, reasonable selectivity, relative fast response and low cost. In this way,

Mazloum increases the selectivity of the electrodes towards mercury by the use a plasticized polyvinyl chloride (PV) matrix with sulfur-containing thio ligands¹⁸. The measurement has a limit of detection of 0.12 mg L⁻¹ and it is pH dependent. The integration of traditional electrochemical techniques is also possible due to the recent advances in microfluidics. In this sense, an “on-chip” mercury microelectrode has been proposed for metal ion detection¹⁹. The system is composed by a mercury droplet cavity, a counter electrode, a reference electrode, microchanel and a heater that drives the mercury flow through the microfluidic components. The whole device is fabricated using two glass layers, wherein the microcavities are etching-window patterning, see Figure 2.2. The analytical signal is obtained by square wave stripping voltammetry (SWSV).

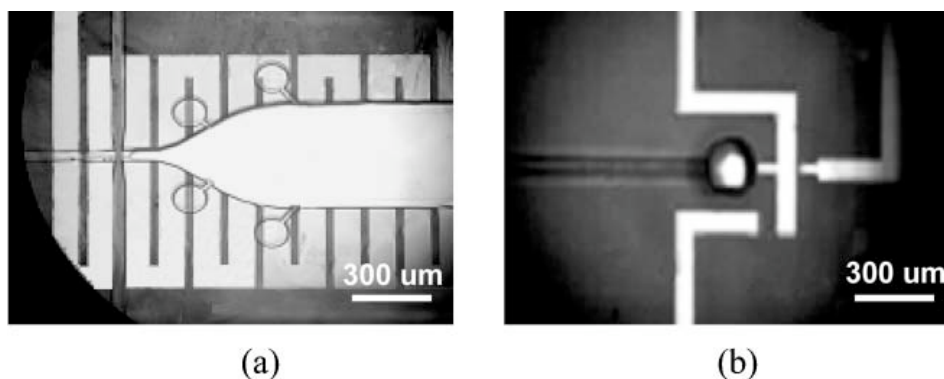


Figure 2.2. Example of electro-chemical device for metal ion detection with integrated microfluidics developed by Zhu¹⁹. a) Structure of the injection channels and cavities, b) electrodes for the electrochemical cell.

Finally, the device was tested for Cd²⁺ and Pb²⁺ ions. Multisensor arrays have been also explored with electrochemical techniques. For example, Kuhlman presents an electronic tongue based on anodic stripping voltametry (ASV)²⁰. The system can be miniaturized and 9 REDOX cells can compose it, see structure of the system in Figure 2.3a. Microelectronic fabrication methods as screen-printing and laser drilling have been employed on alumina support for the electrode layer and the cell array design respectively, see Figure 2.3b.

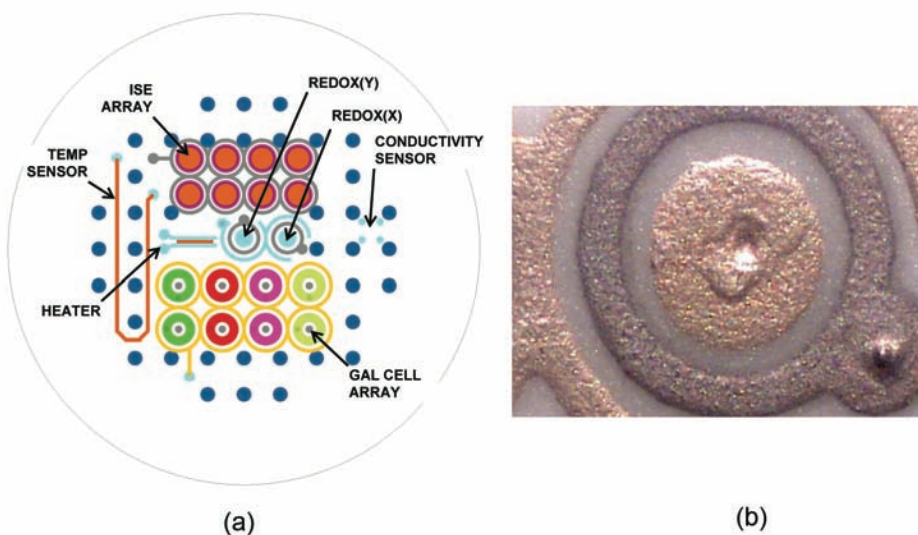


Figure 2.3. a) Scheme of electronic tongue with 20 sensors and one heater designed by Kuhlman²⁰ array. b) Photomicrograph of REDOX cell. The diameter center is 0.75 mm.

Interesting applications of mercury monitoring are based on the conductivity changes of a gold thin film upon exposure to mercury. Gold

has high affinity to mercury and the electrical resistance change is produced by the formation of an Au-Hg amalgam at the Au surface, herein the amalgam acts as a pre-concentrator. These systems are easy to fabricate in small dimensions, hand held and a fast response time. The sensitivity can be tuned by the thickness of the Au film, augmenting as the film thickness decreases. Moreover, microelectrode arrays allow for high sensitivities and best signal to noise ratio. In this sense, a voltametric method for mercury detection is presented based on a gold microelectrode array²¹. The on-chip system is fabricated by photolithographic techniques and presents a limit of detection of $3.2 \mu\text{g L}^{-1}$. Recent work attempts to increase the sensitivity by Au nanowires, thus the surface area to volume ratio is augmented, and consequently, the sensitivity is enhanced²². The results show that sensitivity is increased by a factor of two with the nanowire solution. A detection limit of 0.05 mg L^{-1} is observed for elemental mercury; meanwhile the sensitivity for Hg^{+2} is poorer. The exposure to Cu^{+2} , Mg^{+2} and Na^{+2} does not introduce appreciable resistance changes.

A high degree of integration can be achieved with ion selective field effect transistors (ISFET). These incorporate a sensitive membrane directly attached on the gate area of the transistor. Note in Figure 2.4 the structure of an ISFET and its difference from a generic MOSFET. The chemical interaction with the analyte creates a change in the charge density of the sensing membrane, thus increasing the current flow between the source and drain. There are many examples of

semiconductor devices that have been incorporated as bio/chemical transducers with slightly modifications in their structure. For example, platinum electrodes in contact with a film of ethyl 2-thienylglyoxalate compose an ISFET for Cu^{2+} ion²³ with a detection limit of 6.35 mg L^{-1} .

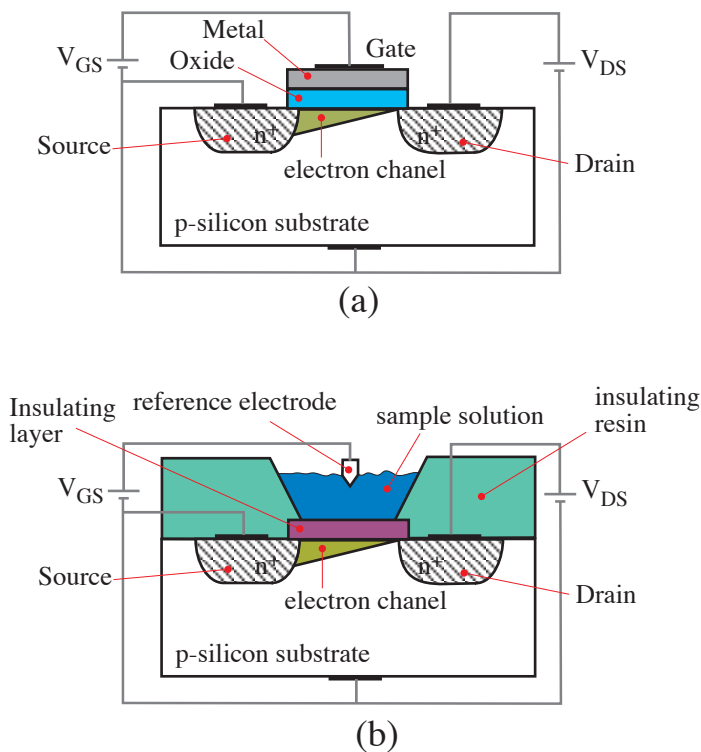


Figure 2.4. Schematic representation of a MOSFET a) and an ISFET structure b).

Apart from conventional semiconductor field effect transistors, electron mobility transistors (HEMT) have been widely used for gas and liquid sensors. Wang²⁴ exposes a functionalized AlGaN/GaN HEMT for the detection of metal ions. A thin gold film of 5 nm is deposited as gate

metal, which is functionalized with thioglycolic acid. A drain current change is observable when thiol groups interact with Hg^{+2} or Cu^{+2} . The selectivity is low and the authors recommended an array of this sensors in order to provide a cross response to several analytes.

Table 2-I summarizes some of the electrochemical sensors commented above.

TABLE 2-I. List of electrochemical sensors for heavy metal detection.

Analyte	Method	Pre-treatment	LOD (ppm)	Interference	Integration facility
Hg^0	FI-Amperometric detection ¹⁷	Yes	0.009	Ag^{+1} , Se^{+2} , Cu^{+2}	2 (0-5)
Hg^{+2}	Potentiometric ¹⁸	Yes	0.12	Ag^{+2}	3 (0-5)
Zn^{+2} , Pb^{+2} , Cu^{+2} , Mn^{+2}	ASV micro-cell array ²⁰	None	20	Apparently none	3 (0-5)
Hg^{+2}	Voltametric by gold microelectrode array ²¹	Yes	0.03	Apparently none	5 (0-5)
Hg^0 , Hg^{+2}	Conductimetric by gold nanowires ²²	None	0.05	Apparently none	4 (0-5)
Cu^{2+}	Potentiometric ChemFET	None	6.35	Ca^{2+}	5(0-5)
Cu^{+2} , Hg^{+2}	HEMT ²⁴	None	0.2	Hg^{+2} , Cu^{+2}	5 (0-5)

2.1.2 Mass-sensitive sensors

Mass-sensitive sensors detect the change of mass on a sensing layer. In the case of chemical sensors, the mass changes arise from absorption, evaporation, deposition, or erosion due to the chemical reactions. Several sensing structures have been employed to detect these mass changes, such as quartz crystal microbalance (QCM), thickness shear mode (TSM) and surface acoustic wave (SAW). Typically, these sensors offer high sensitive (in parts per billion). Miniaturized sensors have been achieved with mass-based sensors that use the resonant frequency shift of a cantilever beam to detect the change in mass. The cantilever is electrostatically actuated, and the resulting vibration of the cantilever produces a capacitance change. By appropriately modifying the cantilever surface, binding-induced changes can be monitored. Mass-sensitive sensors have been widely used for gas and vapour phase, but depending on the device and the type of wave generated detection in liquids is also possible^{25, 26}. On the other hand, liquid measurements require a well design to avoid unwanted disturbances from pressure shocks, turbulence, or temperature gradients²⁷. Microcantilevers functionalized with proteins have also been explored for heavy metal detection in water²⁸. Silicon nitride cantilever with gold on one side were used as sensing element after covalent bonding with the protein. Cantilever deflections were measured with an AFM (Atomic Force Microscope) head. Obviously, this design is a proof-of-principle and

further work is necessary to achieve a miniaturized device. In fact, this is not a simplest task due to the electronic complexity related with this kind of sensors. Figure 2.5 shows a prototype of cantilever micro-array fabricated by IBM.

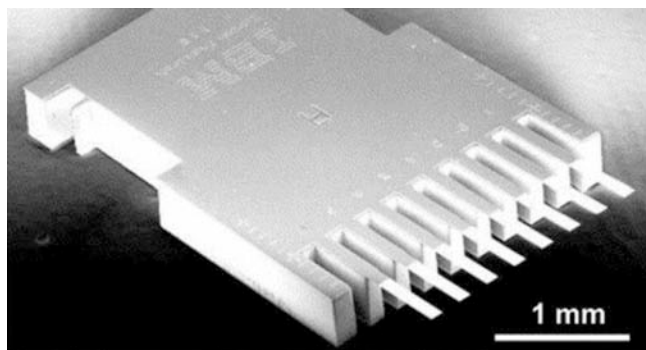


Figure 2.5. Scanning electron micrograph of a cantilever array.

2.2 Opto-Chemical Sensors

The information delivered by an opto-chemical sensor is constituted by an optical signal generated by the exposition of a molecule to an analyte. Therefore, the molecule acts as a transducer transforming the chemical interaction into an optical signal. Basically, a molecule absorbs light at particular wavelengths or energies ($h\nu$) corresponding to transitions between well-defined internal energy levels. These energy levels correspond to quantized states for three different types of transitions: rotational, vibrational and electronic. In the optical spectrum, electronic transitions are caused by the absorption by specific bonds and functional groups within the molecule. The absorption wavelength corresponds to energy of transitions between two states or electronic configurations. The

intensity of the absorption band, represented by the molar absorptivity (ϵ), depends on the probability of the transition and the polarity of the excited state²⁹. In general, a molecular probe has a receptor part formed by atomic groups which creates a charge density change when are in contact with an analyte, like an acceptor-donor system. This modification in the intra-molecular charge transfer can activate other atomic groups, which are responsible of signalling the exposition to the foreign element. In some cases, the last groups can be linked to the receptor acting as a label or indicator. The indicators can be categorized by their optical properties as *chromophores* or *fluorophores*. The *chromophores* have functional groups that absorb light in the ultraviolet and visible regions. There are many atomic groups causing different effects in the spectrum, for example some of them can enhance the absorption or shift the wavelength. On the other hand, the *fluorophores* are molecules with light emitting properties that can be changed when interact with the analyte. Moreover, there are switchable fluorophores, which can enhance (*'turn on'*) or quench the fluorescence (*'turn off'*) in the presence of analyte.

2.2.1 Optical measurement techniques

The most widely used techniques in optical chemical sensors are optical absorption and luminescence. But other sensors have been developed based on other techniques, such as refractive index and reflectivity. Moreover, the emerging optical techniques, such as plasmon surface resonance, are also promising techniques for the heavy metal detection.

There are an amount of optical transduction possibilities, which depending on the sensibility and complexity requirements can be elected. Below, it is exposed a brief explanation of optical measurement techniques suitable for using in an optical device, especially in liquid measurements.

2.2.1.1 Absorbance

Absorbance is the simplest technique for recording changes in the ultra-violet-visible-near infrared spectrum. The intensity changes due to absorption is related with the concentration of absorbing species via the Beer-Lambert relationship expressed as:

$$A = \log T = \log I_0/I = \epsilon d C \quad (2.1)$$

where A is the absorbance, T is the transmittance, I_0 is the incident light, I is the transmitted light, ϵ ($M^{-1} \text{ cm}^{-1}$) is the molar absorptivity, d (cm) is the path length traversed by the light, and C (M) corresponds to the concentration of the absorbing species. The main limitations of absorbance measurement are the small dynamic range and sensitivity. The Beer-Lambert Law establish a linear dependence between absorbance and concentration, but at high concentration of the absorbing species this is not accomplished. The sensitivity depends on the transversal optical path, thus when the molecule is immobilized on a film the sensitivity is reduced in order as the film is thinner. Thus, accurate measurements can be achieved working in liquid phase with low

concentrations of the absorbing species. On the other hand, the absorbance technique is the simplest way to analyze the response of a chemical probe, obviously, if this presents a spectral change. Spectral measurements are composed by: a source lamp (halogen, xenon, led, etc.), a photodetector as charge-coupled device (CCD) or photodiode array, and an optic element for the light decomposition: prisms, gratings, or wavelength-selective filters. Spectrometers with different levels of integration can be encountered, from heavy laboratory equipment to “on-chip” integration. Recently, optical sensing schemes with a high degree of miniaturization can be achieved combining organic light emitting diodes (OLEDs) and CCD or silicon photodiodes in a sandwich structure³⁰. Absorbance measurement covers from 250 to 1000 nm. Moreover, for the deep infra-red part of the spectrum Fourier transform can be used.

2.2.1.2 Scattering

Another phenomenon caused by the interaction of light with matter is the light scatter effect. Herein, the intensity of the scattered radiation can be related to the concentration of the scattering particles. Several well-known methods can be derived from scattering phenomenon. For example, reflectance measurements may be used when the optical surface under analysis is opaque or it transmits light only weakly. Two types of reflection occur on a surface. Specular reflection takes place at the interface of a medium with no transmission through it. When the light

penetrates the medium and subsequently returns after partial absorption and multiple scattering within the medium is named diffuse reflection. There are several models for diffuse reflectance based on the irradiative transfer theory that can be used depending on the type of the samples. A common technique for aqueous media is Raman scattering, wherein frequency shifts (spectrum) from scattered light reveal the characteristic vibration frequencies of the atoms, and hence, the chemical composition and structure of the material. SERS (Surface-Enhanced Raman Spectroscopy) is a technique that increases the Raman signal by up to 10^7 times. Typically, a thin layer of silver (50 to 100 nm) is deposited on a roughness surface and the analyte is evaporated from solution onto the silver layer.

2.2.1.3 Fluorescence

Fluorescence is a particular case of luminescence. Upon light absorption, the dye is excited and later the excited state can lose its energy by either the thermal deactivation or emitting light. The emission of photons accompanying de-excitation is then called *photoluminescence* (fluorescence, phosphorescence or delayed fluorescence). The fluorescence *quantum yield* is defined as the ratio of the number of photons emitted to the number of photons absorbed. When an analyte is fluorescent, a direct detection is possible by means of a spectrofluorometer operating at appropriate excitation and observation wavelengths. However, most ions and molecules are not fluorescent and

indirect methods needs to be used. Such methods can be obtained by the reaction of the analyte with a reagent leading to a fluorescent compound, or by the formation of a fluorescent complex, which is the basis of most methods of ion and molecule recognition. Fluorescence *quenching* is a result from the collision of the analyte or a *quencher* with a fluorescent compound, which is traduced either in a reduction of the fluorescence intensity, emission decay. The wavelength of the emitted luminescence λ_{em} is different from that of the exciting radiation λ_{ex} , which must be located preferable at the main peak of absorbance of the molecule. It is usually called *Stokes shift* to the spectral gap between the first absorption band and the maximum of the fluorescence spectrum. A remarkable effect occurs when several compounds are present and fluoresce simultaneously, thus their emission can be mutually attenuated by absorption of the exciting radiation. This phenomenon is called inner filter effect (IFE). The fluorescence is an extremely sensitive technique capable of determining very low analyte concentrations. On the other hand, fluorescence has a strong dependence with temperature. Generally, an increase in temperature results in a decrease in the fluorescence, because non-radiative processes are more efficient at high temperatures³¹. Fluorescence measurements are indeed more difficult than absorbance measurements and many parameters can affect the lifetimes (pH, temperature, presence of quenchers, etc.), which could lead to erroneous interpretations. Moreover, fluorescence requires a high degree of instrumentation, and also undesirable optical effects, such as light

polarization or possible scattered light, may degrade the fluorescence signal. A conventional fluorescent system, such as a fluorimeter, is composed by an exciting source, two monochromators, one for incident light and other for emission light, optical components (shutters, polarizers, beam spliter, etc.) and a photomultiplier or photodiode as detector. The main variables involved in fluorescence measurement are the quantum efficiency, the intensity of the fluorescence and its time dependence characterized by the fluorescent lifetime, and the emission decay. Moreover, several types of measurements can be applied to fluorescent sensors: intensity emission, lifetime, energy transfer, IFE and polarization.

2.2.1.4 Evanescent wave spectroscopy

The evanescent wave spectroscopy is a technique that emerges from the light propagation through a waveguide, first employed in communication systems, and later translated in the chemical sensor field. In a light guiding mode the electromagnetic waves are internally reflected at the boundary of two medias with different refractive index (n_1, n_2). The total internal occurs when the incident angle (θ_i) is greater than the critical angle ($\theta_c = \sin^{-1}(n_2/n_1)$). Particularly, under the condition of internal reflection a fraction of the light propagated in a waveguide penetrates a short distance into the second medium. In this situation, named evanescent field, the intensity of the electromagnetic wave decays

exponentially with distance from interface. Therefore, the electric field penetrates in the rare medium at a distance x with an amplitude of

$$E_x = E_0 \cdot e^{-\frac{x}{d_p}} \quad (2.2)$$

where E_0 is the electric field at the core-cladding interface and d_p is defined as³²:

$$d_p = \frac{\lambda}{2\pi\sqrt{n_1^2 \sin^2 \theta - n_2^2}} \quad (2.3)$$

Figure 2.6 shows a schematic graph of the light intensity distribution between two media with different refractive index (n_1, n_2).

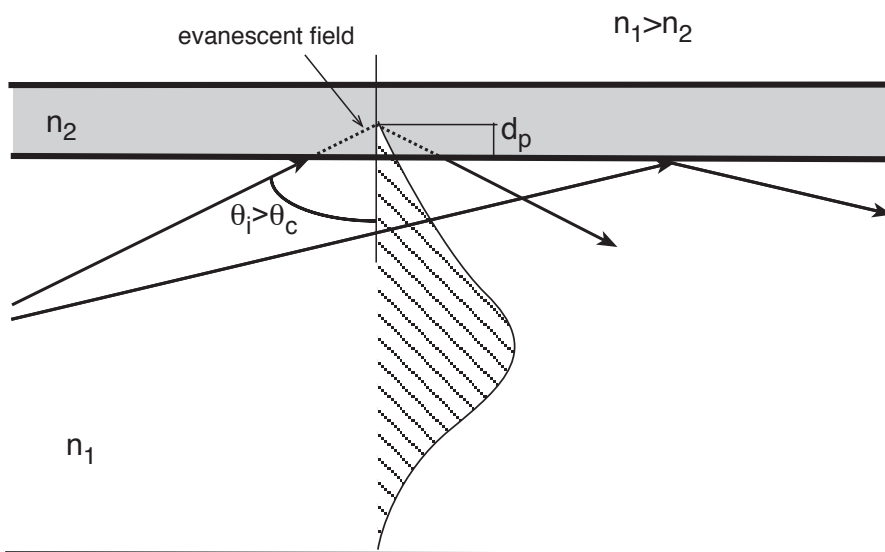


Figure 2.6. Schematic view of the light propagation between two media, being $n_1 > n_2$. All rays greater than the critical angle will be reflected at the medium n_2 and creates an evanescent field.

The evanescent field can be achieved from a slab guide, a planar integrated-optic guide, or an optical fiber. All this optical elements are composed by a core whereby the light is guided due to the internal reflections caused at the boundary of an outer medium named cladding, which usually has a minor refractive index than the core. Advantages of evanescent measurements can be traduced in a high sensitivity, due to the optical interactions are increased by a large optical path. The evanescent can be combined with other optical techniques in order to obtain gained measurements of absorbance, fluorescence, or refractive index. Essentially, the evanescent is applied to chemical sensors by some modification on the second medium, named clad. If the waveguide is unclad, the core of the waveguide is directly in contact with a reagent and measurements in liquid phase can be done. However, most interesting cases are when a doped clad surrounds the waveguide, wherein the molecular probe is bonded. In this case, the measurement is simplified since the analytical interaction occurs at the liquid-solid phase, and some steps in the reagent preparation can be overcome. There are amounts of materials that can serve as optical support for molecule probes in evanescent measurements. The most used are thin films of polymers and metal oxides obtained by sol-gel techniques. Therefore, the doped clad produces a modulation of the light propagated through the waveguide that is correlated with the analyte concentration. More details of optical support and immobilization techniques and its implementation

on optical fiber will be explained in Chapter 4 and Chapter 5 respectively.

2.2.1.5 Refractometry

This technique consists in the determination of the refractive index of liquids and gases. Moreover, this measurement is also related with the angle of refraction at the waveguide-sensing interface. The simplest measurement can be achieved by observing the intensity of light transmitted or reflected by the optical transducer, since light that exceeds the critical angle is lost into the external media, wherein the analyte interacts. Unfortunately, refractive index has a strong dependence with temperature and some corrections are necessary if high sensitivity is required.

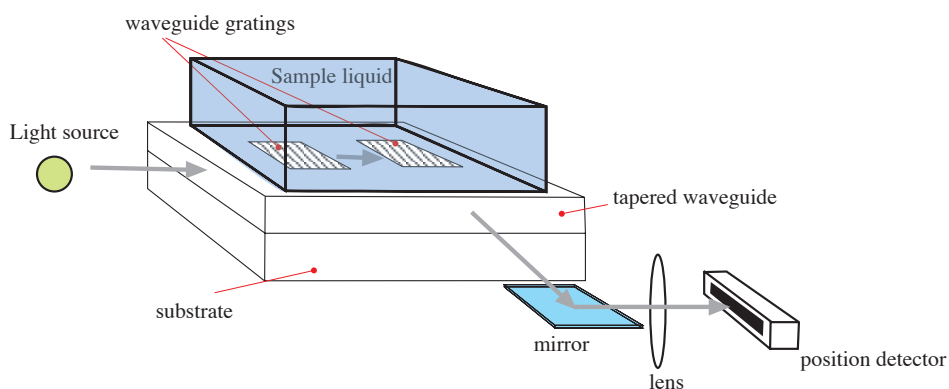


Figure 2.7. Example of a refractive sensor. A change in the refractive index of the liquid sample produce an angular variation of the output light beam.

2.2.1.6 Interferometry

In general, an optical interferometer detects the differences between coherent waves that travel in separate paths, but one of them is exposed to a significant change caused by the analyte. When these light beams are collected, a phase difference related with the analyte concentrations is observed. Different types of interferometers can be applied to chemical sensors. For example, in Figure 2.8 a Mach-Zehnder configuration is exposed, wherein two beams travel different paths, one for the analytical signal and the other for reference signal.

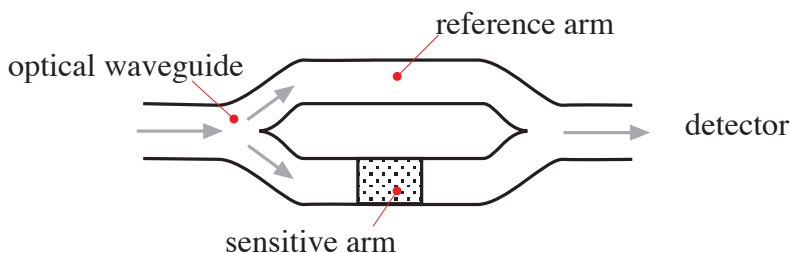


Figure 2.8. Configuration of a Mach-Zehnder interferometer on a planar waveguide.

2.2.1.7 Other optical techniques

Apart from the techniques explained above, it is important to comment other optical methods suitable to employ for chemical sensing, but with an increment of the circuitry complexity. For example, surface plasmon resonance (SPR) can be considered as an extension of evanescent wave spectroscopy. The difference is that the waveguide is covered with a thin

metal film (typically gold and silver), which suffers an oscillation at the dielectric/metal interface (free-electron plasma) when light is totally reflected. These oscillations are very sensitive to any change of this boundary. Consequently, this principle can be applied to detect adsorbed analytes onto the metal surface. Other technique that is emerging for spectroscopic analysis and sensing is named grating light reflection spectroscopy (GLRS). This method employs a diffraction grating in contact with the sample to be analyzed, wherein a light beam is directed on the grating. This grating consists in a highly reflective chrome mask layer deposited onto a silica support. Some of the diffracted orders are transformed from travelling waves to evanescent waves at a specific wavelength and angle of incidence, both of which are functions of the grating period and the complex index of refraction of the sample³³. Normally, the analytical signal corresponds to the intensities of some reflected orders that are correlated with the refraction index of the sample.

2.3 Optodes For Heavy Metal Detection

Due to the improvement of light sources and photodetectors the field of opto-chemical sensors begins to grow and develop further. The aim of the research field is the achievement of low cost alternative and miniaturized sensors in contrast to the heavy laboratory equipment. At the beginning, most applications with optical fibers were dedicated to the monitoring of

physical parameters, such as temperature, velocity, or simple spectrometers. Two years later, an amount of the optical sensors include some kind of functionalized membrane for a bio/chemical sensing. Since 2003, a great variety of spectrometers with reduced size are commercial available. These include optical fiber connexions allowing the combination of several types of light sources (halogen, led, xenon, laser, etc.). In general, these spectrometers employ CCD or diode arrays as photodetector element.

Basically, the optical fibers and the recent planar waveguides are the most known optical platforms for opto-chemical sensors. The election of the topology of the sensor is paramount for the sensing functionality, specially: sensitivity and stability.

In general, the term *optode* is used to describe the waveguide sensitive elements that form an opto-chemical sensor: optical waveguide, light source, and photo-detector. These optodes can be classified as extrinsic, when the analytical signal is launched in a zone that is not linked by any means to the waveguide, and only transports the optical signal. An optode is intrinsic if its waveguide element has been modified, for example, with a sensitive indicator. Therefore, the optical properties of the guided light are modulated by the presence of the analyte. Extrinsic optodes benefit from the relatively simple optical setup being such sensor configurations available as standard commercial, meanwhile the intrinsic optodes requires a further step in the fabrication procedure. In the last case, the

indicator and reagents are usually immobilized onto a thin film or membrane attached to the waveguide. Most of these intrinsic optical sensors are based on the evanescent field measurements. For example, in optical fibers, this may be achieved by replacing the cladding of the fiber over a portion of its length by a solid matrix that contains the reagent. On the other hand, in planar waveguides the sensing layer is directly attached on the top of the waveguide. This indirect sensing technique requires the reagent to be immobilized either in the liquid or solid phase. Recently, the tendency is to work on solid phase with thin films based on polymeric membranes or sol-gel matrixes. Obviously, working on solid films facilitates the integration process, but some problems may appear. A sensitivity reduction and an increment of the response time are inherently caused due to the diffusion coefficient of the material. Furthermore, dye leaching will degrade the stability of the sensor too. Figure 2.9a represents an example of extrinsic optode, wherein a multimode optical fiber illuminates and collects the reflected light that passes through a sensitive disc. This is one of the simplest configurations so as to integrate the sensitized solid material into an optical fiber platform. However, the formation of bubbles inside the cavity that can interfere with the measurement constitutes one of the main challenges in the cell design. Figure 2.9b shows a scheme of intrinsic optode, wherein an evanescent field occurs at the boundary between a sensitive layer and the optical core of a planar waveguide.

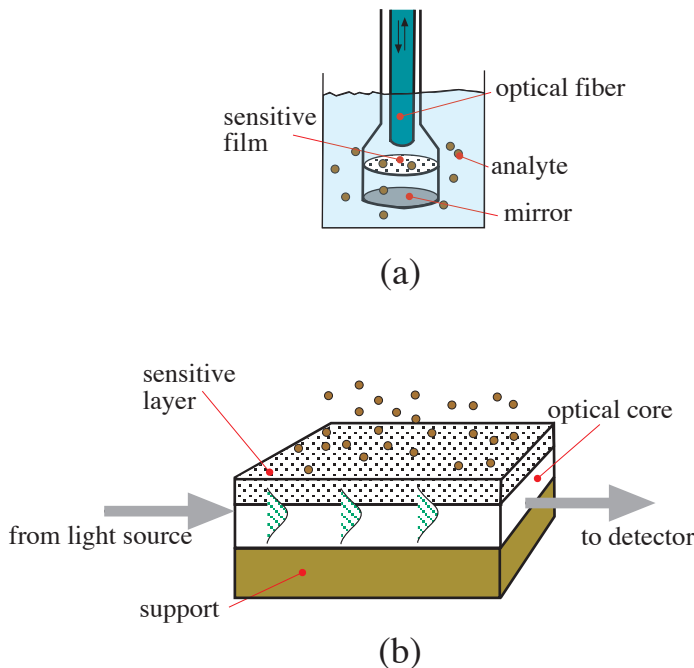


Figure 2.9. Schematic view of: a) an extrinsic optode with multimode optical fiber and a sensitive membrane of an optical fiber sensor, and b) an intrinsic optode composed by a planar optical waveguide coated with a sensitive layer.

In order to supply a better knowledge of the state of the art in opto-chemical sensors, in this work the term optode will refer to the reagent anchored onto a support and attached to the light guiding components. In other case, it will be considered as molecular probes with capabilities to be anchored onto an optical support. There are a lot of optical platforms suitable to achieve an opto-chemical sensor, but the major difference relies on the sensitive film deposited. It is only possible to achieve a performance of the optode if the materials are compatible. In some cases

the molecule can not be adsorbed onto a film, due to problems of leaching, binding, etc., thus the reagent is used in liquid form trapped in a cell, and fiber optics are responsible for the read out signals.

The most extended examples of optodes are based on absorbance measurements or colorimetric changes. Nowadays, a great effort is dedicated to the design of new molecular probes, which will increase the development of optodes based on luminescence, precisely fluorescence, in the next years. Optical fiber is the most wave-guided form employed for chemical sensors for its simplicity and the advantages that presents, which mainly include a wide bandwidth, resistant to electromagnetic interference, high sensitivity, electronic instrumentation can be remotely located from the measurement site, small size and low optical losses.

On the other hand, the planar optical waveguides due to the microfabrication advances constitutes an attractive platform for the opto-chemical sensors. Planar optical waveguides are suitable for sensor array at a high level of integration, which also can be combined with microfluidics³⁴. An advantage of this structure is its robustness when compared with a fiber-based system since the planar design facilitates the membrane deposition, and the fabrication process is compatible with the integrated circuit microelectronic technology. Therefore, many of these microfabricated planar waveguide optodes presents a multilayer structure, which are suitable for chemical sensing having high sensitivity, for example, in absorbance measurements³⁵. There are a vast number of

applications that employ fiber optics or planar waveguides for diverse applications, and combining diverse measurement techniques, for example, raman scattering³⁶, interferometry^{37, 38}, surface plasmon resonance³⁹, refractive index and reflection grating^{33, 40} detection are available in the literature.

Particularly, there are not as many examples of opto-chemical sensors for heavy metal detection as those for pH, temperature or humidity. The ongoing demand on sensing devices applied to diverse field, such as environmental monitoring, will increase the applications of chemical sensor with better performance such as stability, selectivity and sensitivity. The simplest way so as to use a molecular probe as an opto-chemical is the pool optode configuration, wherein the molecule is in liquid phase entrapped in a cell, usually with a flow injection system. For example, an extrinsic pool optode based on fluorescent measurement is proposed for Cd²⁺ and Zn²⁺ detection⁴¹. Other example of pool optode is developed by Kuswandi⁴² with safranin-iodide solution as reagent for mercury detection and a filter composed by a Nafion membrane, which is highly permeable to cations. The sensitivity is lower (limit of detection (LOD) = 1 mg L⁻¹) considering that the reaction takes place in liquid phase. In this sense, the sensitivity could be enhanced by the use of an evanescent wave configuration, wherein the optical path can be ten times higher. An example of this is a partially unclad fiber optic used for absorbance measurements in the chromium detection⁴³. A cylindrical glass tube incorporates the optical fiber with the unclad region inside and

provided with inlet and outlet for the liquid samples. Once the sample has delivered inside the glass tube, the reagent is added (solution of 1,5-diphenylcarbazide). Obviously, this configuration is an extrinsic optode and can be used to measure other contaminants in water. A minor level of integration is achieved with this arrangement, but it presents some advantages from the direct absorbance measurements. First, the sensitivity is increased by augmenting the optical path to 12 cm instead of 1 cm that corresponds to a standard cuvette. In this way, the sensitivity for chromium was increased 20 times when compared to the conventional spectrophotometric method. Second, due to the fact that the optical interactions on the evanescent field travel short distances, normally less than 1 micrometer in the visible spectrum, many problems in absorbance measurements related with scatter particles dispersed in the samples are not present in the evanescent measurements. Other extrinsic evanescent wave absorption fiber optic sensor was developed for Fe³⁺ detection in water⁴⁴. The iron detection was based on a solution of potassium thiocyanate and a fiber optic with an unclad length of 12 cm as the transduction mechanism. It was observed a detection limit of 1 µg L⁻¹, and an upper limit of 50 mg L⁻¹ of iron ions.

Immobilizing the reagent onto a film or membrane, with a signal acquisition performed by an extrinsic optode, does the next step in integration level. Madden⁴⁵ et al. described a flow cell extrinsic optode for the colorimetric determination of Ni²⁺. The measurement is based on absorbance measurements, wherein a reagent (1-(2-pyridylazo)-2-

naphthol (PAN)) is immobilized onto a transparent Nafion membrane. The cell has two apertures for optical fibers. One delivers light from a led-based source and the other guides the optical response through a home made spectrophotometer based on a photodiode. The metal binding is reversible with nitric acid and the interferential metal ions are Cu^{2+} , Pb^{2+} , Hg^{2+} and Zn^{2+} . Other example is the mercury determination carried out with 1-(2-thiazolylazo)-2-naphthol (TAN) immobilized in Nafion films⁴⁶. It was proposed two optode designs, one for absorbance measurements and the other for reflectance. In both cases, the film is localized inside a flow cell with fiber optics as light guide. The limit of detection was 0.01 mg L^{-1} , with Co^{2+} and Ni^{2+} ions as the main interferences. The mercury-TAN complexation was reversible with 0.1 M of HCl.

Moreover, Kuswandi experimented with other colorimetric optode for mercury detection with diphenylcarbazone as a reagent⁴⁷. Baldini⁴⁸ presents an absorption based optode for Hg^{2+} detection. The sensitive element is based on dye 2-(5-amino-3,4-dicyano-2H-pyrrol-2-ylidene)-1,1,2-tricyanoethanide (L') adsorbed on a cellulose paper. The light is guided by fiber optics and an opto-electronic unit was developed for the light source and detection system. Other home-made spectrometer is designed by Kuswandi and Narayanaswamy⁴⁹. The system is based on multi-LEDs and two photodiodes, and it was tested for Hg^{2+} ions using 4-(2-thiazolylazo) resorcinol (TAR) immobilized onto XAD-4 (styrene divinylbenzene cross-linked copolymer). The optode was formed by a

bifurcated fiber optic connected to a micro flow cell, wherein the membrane is localized. A kinetic method was employed for the mercury concentration predictions with a detection limit of 0.01 mg L⁻¹. The dye is regenerated immersing the optode in an acid solution of HCl. However, the TAR reagent is a non-selective complexing agent and a strong reflective response of the optode was observed for Ag⁺, Ni²⁺, Fe²⁺, Cu²⁺, and Co²⁺ ions.

Finally, the intrinsic optodes contribute to the compactness configuration with an easier, quick and accurate method to measure the water quality. Nowadays, there are few examples of intrinsic optodes dedicated to monitoring heavy metals in solution. Yeh⁵⁰ et al. designed an evanescent wave optical fiber with a functionalized silica cladding prepared by sol-gel processing. The entrapped reagent is propyl-ethylenediamine triacetate, which forms a colored complex with Cu²⁺ ions. The optode has a dynamic range of 0.5 -100 mg L⁻¹ and a limit of detection of 0.05 mg L⁻¹. As an example, a kinetic calibration was needed for the copper quantification in milk samples. Other intrinsic optodes based on evanescent absorbance measurements have been developed for the detection of Cu²⁺. In such cases, the fiber optic is dip coated with a mesostructured silica produced by a sol-gel process, and doped later on with Eriochrome Cyanine R⁵¹. The detection limit of copper ions was around 3 mg L⁻¹. Table 2-II shows a list of optodes designed for the heavy metal detection.

TABLE 2-II. Examples of optodes used for heavy metal detection.

Analyte	Reagent	Method	Pre-treatment	LOD (ppm)	Interferences	Integration facility
Hg ²⁺	safranin-iodide ⁴²	Reflectance pool optode (extrinsic)	pH	1	Fe ²⁺ , Ag ⁺	2 (0-5)
Hg ²⁺	1-(2-thiazolylazo)-2-naphthol ⁴⁶	Reflective and absorbance flow cell optode (extrinsic)	pH	0.01	Ni ²⁺ , Co ²⁺	3 (0-5)
Hg ²⁺	diphenylcarbazone ⁴⁷	Colorimetric optode (extrinsic)	--	0.04	--	3(0-5)
Hg ²⁺	2-(5-amino-3,4-dicyano-2H-pyrrol-2-ylidene)-1,1,2-tricyanoethanide (L') ⁴⁸	Colorimetric optode (extrinsic)	--	--	--	4 (0-5)
Hg ²⁺	4-(2-thiazolylazo) resorcinol ⁴⁹	Reflectance optode (extrinsic)	pH	0.01	Ag ⁺ , Ni ²⁺ , Fe ²⁺ , Cu ²⁺ , and Co ²⁺	4 (0-5)
Cu ²⁺	Eriochrome Cyanine R ⁵¹	Absorbance evanescent fiber optic (intrinsic)	pH	3	--	4 (0-5)
Cu ²⁺	propyl-ethylenediamine triacetate ⁵⁰	Absorbance evanescent fiber optic (intrinsic)	None	0.05	--	4 (0-5)
Ni ²⁺	1-(2-pyridylazo)-2-naphthol ⁴⁵	Colorimetric flow cell optode (extrinsic)	pH	1	Pb ²⁺ , Hg ²⁺ , Cu ²⁺ , Zn ²⁺	4 (0-5)
Cr ²⁺	1,5-diphenylcarbazide ⁴³	Absorbance evanescent fiber optic (extrinsic)	pH	0.01	--	3 (0-5)
Fe ³⁺	Potassium thiocyanate ⁴⁴	Absorbance evanescent fiber optic (extrinsic)	pH	0.01	--	3 (0-5)

Note that most of the examples are based on extrinsic optodes wherein the reagent is mixed with the same solution sample. There are just a few examples of intrinsic optodes aimed to detect heavy metals, what we believe constitutes one of the main challenges of this research.

Needless to say that the research on heavy metals detection is in continuous evolution, and new molecules with capabilities to be anchored into an optical support are emerging on the scientific literature. Table 2-III shows a list of known molecules for diverse cation detection; these examples have a close distance for their use as full optode for trace heavy metals in water.

TABLE 2-III. Some example of molecules supported on film for metal ion detection.

Analyte	Molecule	Film	Method	LOD (ppm)	Interferences	Reversibility
Pb ²⁺	N,N,N',N'-tetradodecyl-3,6-dioxaoctane-1-thio-8-oxodiamide ⁵²	Poly(vinyl chloride) (PVC) and bis(2-ethylhexyl) sebacate (DOS)	Absorbance	0.02	Cd ²⁺ , Cu ²⁺ , Hg ²⁺ , Ag ⁺	--
Pb ²⁺	3,3',5,5'-tetramethyl-N-(9-anthrylmethyl)benzidine ⁵³	PVC and DOS	Fluorescence	0.1	Hg ²⁺ , Ag ⁺ , Co ²⁺ , Ni ²⁺ , Cd ²⁺ , Cu ²⁺	HCl
Pb ²⁺	2-amino-cyclopentene-1-dithiocarboxylic acid ⁵⁴	triacetylcellulose	Absorbance	0.14	Ni ²⁺ , Cd ²⁺ , Cu ²⁺	--
Pb ²⁺	18-crown-6, dibenzo-18-crown-6, <i>tert</i> -butylcalixarene- <i>O,O',O'',O'''</i> -tetraacetic acid tetramethyl ester, and cryptand [2,2,2] ⁵⁵	PVC and 2-nitrophenyl octyl ester	Absorbance	1.65	Cu ²⁺	--

Analyte	Molecule	Film	Method	LOD (ppm)	Interferences	Reversibility
Cr ⁶⁺	1,5-diphenylcarbazide ⁵⁶	plasticized cellulose triacetate (CTA)	Absorbance	0.01	--	No
Cr ⁶⁺	Aliquat 336 and 4,5-dibromofluorescein octadecyl ester ⁵⁷	PVC, ortho-nitrophenyl octyl etherIII PVC NPOE	Absorbance	0.57	SCN ⁻ , ClO ₄ ⁻ , NO ₃ ⁻	Buffer (pH=4.5)
Cu ²⁺	sym-diphenylthiocarbazone (dithizone) ⁵⁸	triacetylcellulose PVC, Sodium	Absorbance	0.01	Hg ²⁺	Thiourea
Cu ²⁺	1-hydroxy-3,4-dimethyl-9H-thioxanthen-9-one ⁵⁹	tetraphenylborate and tributylphosphate (TBP)	Absorbance	0.02	None	HCl
Cu ²⁺	<i>meso</i> -tetraphenylporphyrin with bipyridine ⁶⁰	PVC and DOS	Fluorescence	0.31	Fe ³⁺ , Hg ²⁺	EDTA and buffer
Ga ³⁺	4-(<i>p</i> -nitrophenyl azo)-pyrocatechol ⁶¹	PVC and TBP	Absorbance	0.27	Fe ³⁺ , VO ²⁺ , Th ⁴⁺ , UO ₂ ²⁺ , Zr ⁴⁺	No
Zn ²⁺	Zincon-methytriocetylammmonium ⁶²	triacetylcellulose	Absorbance	0.01	Cu ²⁺ , Ni ²⁺ , Mn ²⁺	HCl

2.4 Mercury Detection With Opto-Chemical Probes

There is a great effort in the design, synthesis and characterization of mercury probes. The increasing number of articles related to this topic in the last years is remarkable. It is important to comment that Hg²⁺ is the

stable form of this metal ion. The detection of Hg⁰ could be of special interest for mercury monitoring emissions from unintentional anthropogenic release and from natural disasters. Detection of *methylmercury* has special interest for food quality control or *in vivo* toxicology studies. But, due to its high toxicity and the risk for the researcher, direct detection of this mercurial specie is less explored. Moreover, procedures for its extraction from organic matter and conversion to Hg²⁺ are available⁶³⁻⁶⁶.

Hg²⁺ ion has no optical spectroscopic signature, hence an indirect optical detection must be done. In this sense, small molecules designed to give read-outs of Hg²⁺ can lead into assay kits, commercial indicators and portable devices, making possible a rapid Hg²⁺ detection. The recognition process of ions can be carried out by synthetic or natural receptors, so called *ionophores* or *carriers*. Molecular recognition refers to the specific non-covalent bonding of a guest species by an organic host molecule. *Ionophores* for heavy metals take advantage of the high affinity of oxygen, nitrogen and sulfur donor atoms towards these ions. Moreover, the supramolecular chemistry allows combining a receptor part with a label responsible of emitting a readout signal. The label may be covalently attached to other molecules and can be chromogenic, fluorescence, chemiluminiscent, bioluminescence, or phosphorescence.

Some matters must be considered in the molecular probe design. First, the most important is the high selectivity towards Hg²⁺ over possible

competitions that will appear in the environmental or biological samples, including thiols, organic acids, and metal ions. Next, is the sensitivity, which it is desirable to achieve as sensitive as possible in order to fulfil water quality demands (the Environmental Protection Agency guideline establish a limit of 2 ppb for Hg^{2+}). In fact, the applications for mercury detection in food, for example fish, requires less sensitive sensors, since the limit of detection can be fixed to 500 ppb. Finally, the probe must contribute with a fast response to mercury ions. Yet, reversibility is also and important factor which must fulfil a molecular sensor.

Other factors, such as temperature and pH dependence, have an important role in a simple monitoring system and must be taken into account during the measurements when the molecular probe carries out its sensing in acidic or basic pH conditions.

2.4.1 Chromogenic mercury detection

The detection of chemical species based on colorimetric test is as well-known screening technique in the laboratories. There are several commercial approaches for mercury indicators based on test strips and assay kits. In this sense, there is a wide range of applications wherein the chromogenic probes have been supported in a piece of paper, film or membrane.

The 1,5-Diphenylthiocarbazone (dithizone) dye is one of the most widely used photometric reagents for colorimetric mercury detection. The metal

forms a complex with the sulfide moieties, which form coloured insoluble complexes with a large number of metal ions. Dithizone has a high sensitivity to mercury, with a detection limit of 2 $\mu\text{g L}^{-1}$ in liquid solution, and 20 $\mu\text{g L}^{-1}$ when it is immobilized on a triacetylcellulose film⁶⁷. Nonetheless, other metal ions as copper, cadmium and lead have a strong influence over the receptor response, and dithizone has also been used as an optode for copper ions⁵⁸. It is worthy to mention too that another drawback of dithizone is its pH dependence and a maximum response is observed at pH 2. Apart from other molecules, which have been implemented as optodes, or immobilized in membranes or films, and already commented in previous section, some efforts have recently done in order to achieve higher selectivity in the mercury probes. As an example, we can find on the bibliography the visual detection of Hg²⁺ based on a mesoporous silica supports treated with the chromophore 5,10,15,20-tetraphenylporphinetetrasulfonic acid (TPPS)⁶⁸. Previously, the silica is functionalized with N-trimethoxysilylpropyl-N,N,N-trimethylammonium chloride (TMAC) monolayer in order to bind the chromophore onto the solid support. A color change from orange to green is produced due to the formation of a charge transfer complex between TPPS and Hg²⁺. The results show that 5 $\mu\text{g L}^{-1}$ of Hg²⁺ can be detected by naked eye, being the colour change stable for more than 30 minutes. The spectrophotometric calibration reveals a detection limit of 3.5 $\mu\text{g L}^{-1}$ of mercury(II). The work conditions for such molecular probe were a response time of 5 minutes at pH 9, wherein an optimum color separation

is produced. Another important feature is that the functionalized films can be stored for a period of eight months with degradation parameters below 5%. In relation with the selectivity, concentration levels of Zn^{2+} , Ni^{2+} , Pb^{2+} , Cu^{2+} and Fe^{3+} can interfere the visual detection of Hg^{2+} and some pre-treatments are recommended so as to mask their interferences.

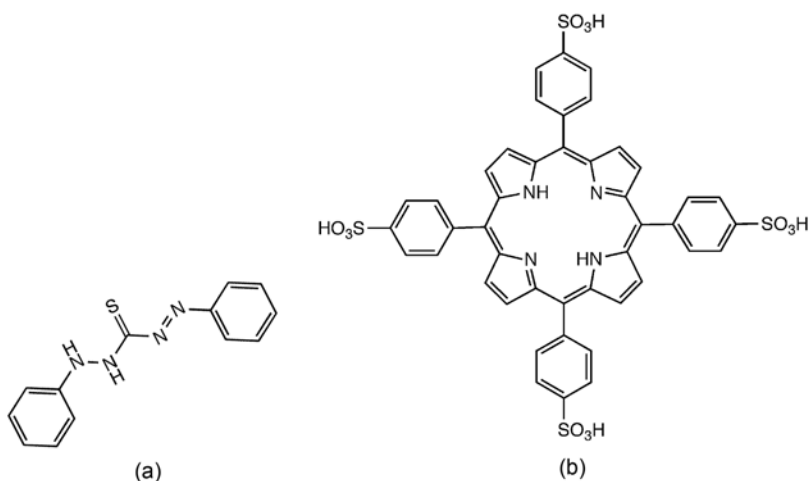


Figure 2.10. Structure of molecules for mercury recognition: (a) dithizone⁶⁷, and (b) TPPS⁶⁸.

Amini et al ⁶⁹ have designed a molecular probe with the aim of increasing both sensitivity and selectivity towards mercury ions. The detection system is based on the interaction of Hg^{2+} with the 2-mercapto-2-thiazoline (MTZ) ionophore. The selectivity has enhanced by the use of thiols groups in conjunction with a proton-selective chromoionophore in plasticized PVC matrix. The color of the membrane turns from blue to purple when mercury is present, being the mercury range of $40 \text{ ng L}^{-1} - 3 \text{ mg L}^{-1}$, with a detection limit of 10 ng L^{-1} . The membrane has a fast

response time (< 40 seconds) when it is compared with other methods and exhibits high selectivity to mercury, being silver the main interference metal ion. Moreover, immersing the membrane in nitric acid solution (0.1 M) can regenerate the color change.

On the other hand, several groups have explored the idea that amine groups can also be used as efficient mercury receptors based on the metal-induced intramolecular charge transfer (MICT) process between the amine group as an electron donor. For example, Fu et al. reported⁷⁰ that the titration of Hg²⁺ to solutions having a mixture of hydrazine hydrate and 4-(diethylamino)benzaldehyde results in a strong red-shift in the spectrum (from 400 to 500 nm). The color change is reversible by adding thiourea. Moreover, the molecule can be anchored to test strips providing a visual detection of 5 mg L⁻¹ of mercury in aqueous solution (pH 7). Other ions did not cause any detectable changes on the test papers for Hg²⁺.

Other approximation that relays in a high selectivity is using several several azo groups, which have been modified in order to exhibit substantial color changes upon complexation with Hg²⁺. The study is focussed on the orientation of *p*-methoxyphenylazo groups and its role in the mercury binding⁷¹.

In fact, some trends in the molecular design are focused on supramolecular chemistry in such a way to define platforms on which assemble various functional groups in a well-defined arrangement in the

space⁷². These structures could give rise to higher extraction efficiencies and selectivities than the individual ligands. Following that, Kuswandi⁷³ proposed a selective Hg^{2+} colorimetric method based on trityl-picolinamide as neutral ionophore. This compound has a tripodal structure and can be incorporated in plasticised PVC forming an ion sensitive layer. After immersing the membrane into a water sample (pH 4.7) for 5 minutes, a colour change from red to blue is produced by ion-exchange mechanism, and a detection limit of 0.1 mg L^{-1} for Hg^{2+} is observed. The main interference caused by foreign ions was promoted by the presence of Ag^+ , Pb^{2+} , Ni^{2+} , and Cu^{2+} . Moreover, the membrane response to Hg^{2+} was not fully reversible.

2.4.2 Fluorimetric mercury detection

The fluorescence mechanism of most of the luminescence based chemical probes can derive into three events: fluorescence quenching (“turn-off”), fluorescent enhancement (“turn-on”), and ratiometric fluorescence, which is a relative measurement when more than one emission band appears. The majority of fluorescent Hg^{2+} probes described to date are intensity based, providing a fluorescence turn-off or turn-on in presence of Hg^{2+} ions. Fluorescence turn-on is preferable to fluorescence quenching because it facilitates analyte tracking indeed in vivo monitoring, and multiple analyte analysis is possible with an array of fluorophores emitting at different wavelengths. Furthermore, ratiometric fluorescence monitoring involves a comparison of

fluorescence intensities at two different wavelengths. The fingerprint of the created complex in the fluorescence domain can improve the analyte quantification in inhomogeneous samples, and interferences may be reduced by chemometric analysis. Other important aspect is the water compatibility, because the fluorescence of most small molecular probes prefers polar solvent. Herein, only the examples that can work in aqueous media, or a mixture of water-organic solvent are commented, with exception of those reagents that are entrapped in micelles promoting a colloidal system (water-organic phases).

2.4.2.1 Turn-Off fluorescence Hg²⁺ detection

Porphyryns have been used as fluorescing reagents for the determination of metal cations, due to their high fluorescent quantum yield and large Stokes shift ($\Delta\lambda > 200\text{nm}$). Following that, Chan⁷⁴ utilized 5,10,15,20-tetraphenylporphyrin (H2tpp) for the selective detection of Hg²⁺. See the structure in Figure 2.10. This reagent exhibits a strong fluorescence, which is quenched via the metal ion complexation. Moreover, H2tpp can be immobilized in a plasticized PVC membrane, thus increasing the capabilities of this approach. The experiments related with the functionalized membrane demonstrated a reversible response to Hg²⁺ ions and possible interferential metal ions exhibits fluorescence changes below 5%. The response time was less than 5 minutes with a detection limit of 8 $\mu\text{g L}^{-1}$ of Hg²⁺ at pH 8. The reversibility is achieved by washing with blank buffer. Later, the same reagent but now immobilized

on sol-gel matrix as support film was described⁷⁵. As it was expected, the fluorescence intensity of the sol-gel film decreased upon addition of Hg^{2+} ions. Under the same conditions that the previous report, sol-gel membranes were tested obtaining similar results in terms of stability, reversibility and selectivity. On the other hand, the sensitivity was minor than PVC membranes, being now the detection limit of 0.7 mg L^{-1} . Another full reversible fluorescence probe was developed using 5,10,15-tris(pentafluorophenyl)corrole⁷⁶. A plasticized PVC membrane was prepared with the reagent showing a wide linear range of Hg^{2+} ($0.02 - 20 \text{ mg L}^{-1}$). The fluorescence quenching in presence of Hg^{2+} was reversible by washing the membrane with blank buffer (pH 6) during 2 minutes. After 100 measurements and regeneration cycles the intensity of the membrane decreased 4% from the initial value.

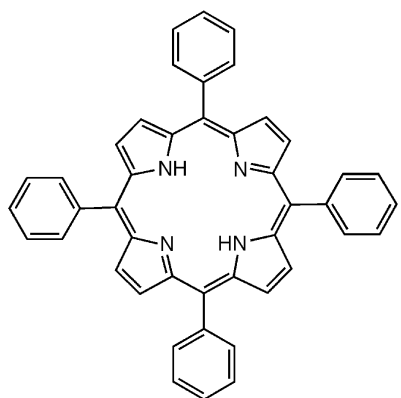


Figure 2.11. Structure of 5,10,15,20-tetraphenylporphyrin (H_2tpp)⁷⁴.

Anthracene⁷⁷ and calixarene⁷⁸ derivatives are also suitable intensity fluorescence-based compounds for Hg^{2+} detection. Additionally, thiacalix [4]arene derivative with 8-hydroxyquinoline were used as a selective ON-OFF type fluorescence probe⁷⁹. The detection limit for Hg^{2+} was

found to be 0.4 mg L⁻¹ in a mixed H₂O-THF solution. Ag⁺ ion was found as the most significant interferential ion.

2.4.2.2 Turn-On fluorescence Hg²⁺ detection

A considerable challenge is the design of fluorescence compounds with turn-on response and compatible with aqueous samples. Enhanced fluorescence probes have an important impact for *in vivo* monitoring. In this sense, the detection of mercury ions was performed on mouse muscle precursor cells and rat neurons by a rhodamine-based fluorescence probe⁸⁰. The dosimeter takes advantage of the Hg²⁺ promoted formation of 1,3,4-oxadiazoles from thiosemicarbazoles. This sensor is cell permeable and can be applied for *in vivo* monitoring. The only drawback is that the induced fluorescence is not reversible. Low Hg²⁺ levels can be detected around 0.02 mg L⁻¹ and high selectivity is observed among other metal ions, except for Zn²⁺ and Ag⁺, which gave slight fluorescence enhancement.

Thiocarbazone derivatives are also compounds that promote 'turn-on' on fluorescence when coordinate with Hg²⁺ ions. Consequently, Zhao assayed with tetra-2-pyridylthiocarbazone for the detection of Hg²⁺ in H₂O/CH₃OH (90:10, v/v) solution⁸¹. The selectivity study reveals that Cd²⁺ and Zn²⁺ increase the luminescence intensities at a separate band that differs 100 nm from the Hg²⁺ measurement signal. In fact, the only interference among several metal ions assayed exposed that Cu²⁺ ions create a quenching effect on the fluorescence emission when mercury is

present. The irreversible response of this compound restricts its use as a chemodosimeter. Difficulties with water-compatibility sometimes can be overcome by incorporating water-soluble groups into the receptor moiety. For instance, sugars can enhance the solubility of a relatively non-polar compound in aqueous media. Following that, D-glucosamine was linked to 2-quinolinecarboxaldehyde⁸². Upon addition of Hg^{2+} ions the intensity of emission was enhanced. The selectivity towards Hg^{2+} was screened for several cations. Only an excess of Zn^{2+} and Cu^{2+} induce slight changes on the fluorescence. The detection limit was 0.10 mg L^{-1} .

Martínez Máñez et al.⁸³ designed a highly selective molecular reporter for Hg^{2+} ions which combines a dual chromo- and fluorogenic (TURN ON) response when reacts with the target ion. The method is based on the thiophilic affinity of the Hg^{2+} ion and its interaction with 2,4-bis(4-dialkylaminophenyl)-3-hydroxy-4-alkylsulfanyl cyclobut-2-enone derivatives. The colorimetric response in water/acetonitrile (4:1 v/v, pH 9.6) solutions allows Hg^{2+} ions to be detected down to 20 ppb by using conventional spectrophotometer, meanwhile, detection limits lesser than 2 ppb can be done by fluorescence detection. Moreover, the molecule can be adsorbed onto polyethyleneterephthalate films, being possible a dipstick assay which can be regenerated by propanethiol.

Rhodamine-based dyes are good candidates for fluorescent molecules in the chemical recognition field. These molecules have large molar extinction coefficient and high emission quantum yield. Consequently, a report

describes Hg²⁺ detection by coupling a carbohydrazone block with Rhodamine 6G⁸⁴. Initially, this compound is colorless and non fluorescent, but the emission turns on when the mercury ion is bounded. Moreover, the solution exhibited a color change to pink when mercury is present. The system can detect Hg²⁺ concentrations of 2 µg L⁻¹ in mixtures of N,N-dimethylformamide (DMF) – H₂O (1:1,v/v). The results suggested that the emission of fluorescence was insensitive to the pH range from 5.0 to 10.0. The selectivity was tested in presence of high concentrations of foreign metals, and practically, it could be concluded that none interference was observed.

Similarly, Yoon proposes a bright fluorescence probe, which is fully compatible with water, and capable for mercury tracking in living cells⁸⁵. The metal ion reception part is carried out by a thioether-rich, which is bounded with a fluorescein derivative. The addition of Hg²⁺ triggers the fluorescence emission up to 44-fold, which constitutes the highest quantum yield with small molecules probes reported to date. The selectivity study concluded that Fe²⁺, Fe³⁺, Co²⁺ and Cd²⁺ cause slight variations in the Hg²⁺ detection. Detection mercury levels of 2 µg L⁻¹ in buffered aqueous solution (pH 7.0) can be achieved with this compound. Furthermore, the molecular probe was assayed in a series of fish establishing that it can distinguish safe and toxic levels of mercury according to the 0.55 mg L⁻¹ US EPA standard.

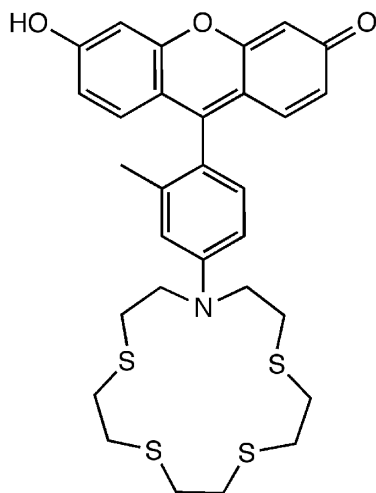


Figure 2.12. Structure of the molecule chromophore used by Yoon⁸⁴.

Other sensitive and selective Hg^{2+} chemodosimeter was developed by Yang⁸⁶. The Hg^{2+} detection mechanism is based on an irreversible desulfurization reaction of thiosemicarbazide moiety to form its corresponding oxadiazole, which it undergoes in a strong and fluorescence emission. Moreover, the results were compared with a synthesized rhodamine-based chemodosimeter. The authors concluded that fluorescein-based probe was more stable and displayed higher sensitivity. Exactly, a detection limit of $0.17 \mu\text{g L}^{-1} \text{Hg}^{2+}$ was achieved in ethanol-water solution (30/70, v/v). On the other hand, the response time of the fluorescein was 15-20 minutes to reach a stable signal, instead, 4 minutes required for rhodamine. The selectivity study of fluorescein probe remarked a high selectivity towards Hg^{2+} ions over other metal ions, wherein only Ag^+ showed very small fluorescence enhancement.

2.4.2.3 Ratiometric fluorescence Hg²⁺ detection

The ratiometric approach provides an enrichment spectrum of emitted luminescence, which leads to some advantages in the quantification process. Herein, chemometric methods may increase either selectivity or efficiency in the calibration process, due to several fluorescence bands contain different, useful, and correlated information with the analyte. Unfortunately, there are less ratiometric fluorescence compounds reported, which it brings new opportunities for the incoming research in the molecular sensors field. Two fluorescence emissions were found to be modulated by Hg²⁺ binding dithiocarbamates ligands linked to an anthracene group⁸⁷. The probes operate in aqueous mixtures of water-acetonitrile (1:1, v/v). Titration curves of Hg²⁺ ions exhibited an increase in the short wavelength emissive peaks and a correlate decrement in the long wavelength emissive peak at 525 nm. The authors estimate a detection limit of 2 µg L⁻¹ Hg²⁺. None fluorescence variations are observed upon pH changes above 3.2, meanwhile Ag⁺ ions interfere in the same order of Hg²⁺ the response of the probe.

Recently, Lippard has reported a ratiometric probe based on a seminaphthofluorescein compound which employs a thioether-rich as metal-binding unit⁸⁸. The features of the probe enclosed a turn-on and dual emission band fluorescence response to Hg²⁺ ions in purely aqueous solution between pH 7-9 range. The Hg²⁺ binding was reversible by adding TPEN (N,N,N',N'-Tetrakis-(2-pyridylmethyl)ethylenediamine) or

KI to the solutions. The study of selectivity showed that Cu^{2+} induces a strong interference by quenching the fluorescence emitted when mercury is present. A detection limit of $10 \mu\text{g L}^{-1} \text{Hg}^{2+}$ was observed.

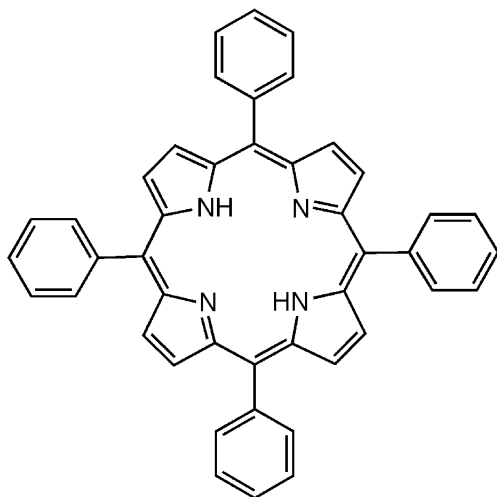


Figure 2.13. Structure of seminaphthofluorescein compound with thioether-rich as metal binding unit⁸⁷.

Furthermore, the molecular design promotes interesting features to small molecular probes, such as a dual-mode Hg^{2+} recognition mechanism, which it affords a colorimetric and fluorescence assay at the same time⁸⁹. For this reason, the authors designed a modular molecular system which was composed by boradiazaindacene fluorophore and two crown ether ligands with specific recognition ability to the Hg^{2+} ion. The working conditions were THF-water (30:70, v/v) buffered at pH 7.2. A blue shift in the absorption spectra was observed upon Hg^{2+} binding. Specificity experiments conducted in absorbance measurements concluded that no color changes were encouraged by the addition of other cations. Furthermore, a blue shift was also observed in the fluorescence emission

by the compound. The initial fluorescence peak at 668 nm decreased upon mercury addition, meanwhile a correlate emission band at 578 nm increased. The selectivity in the fluorescence domain also revealed that no significant changes on the fluorescence response were introduced by the presence of other metal ions. The limit of detection was approximately of 1.6 mg L⁻¹ and 3 mg L⁻¹ for fluorescence and absorbance measurements respectively.

2.4.2.4 Fluorescence probes for Hg²⁺ in micelles

The use of surfactant molecules dispersed in a liquid colloid, named micelles, has wide utilization in different fields: textile industry, mining process, etc... The main advantage of micelles is their possibility to offer a special phase, enclosed inside, distinct from the bulk solution. Most of the small molecule probes published are not able to work in aqueous media. In order to overcome this important trouble, surfactant chemistry offers the possibility to work in water confining separate hydrophobic fluorophores and quenchers in the lipophilic core of the same micelle. Therefore, the micelle acts as a container in water for assembling molecular probes in which, hydrophobic fluorophores and receptors/quenchers are kept together and communicate inside the micelle without the need to build a covalent structure⁹⁰. In this sense, a good example is dithizone, which is a hydrophobic dye, and thus solvent-extraction steps are required for the liquid dithizone-based detection methods. However, these extraction methods are lengthy, time-consuming, cost-intensive and

many of them require the use of toxic solvents. An approach proposed by Khan⁹¹ for the spectrophotometric detection of mercury is based on a micellar system and it makes the direct detection possible with dithizone, without the need of any clean-up procedure. The method shows a high sensitivity in presence of Hg²⁺ ions.

Later, Pallavicini⁹⁰ designed a system based on a pyrene fluorophore which fluorescence emission can be switched by the lipophilicity of the ligand. If the ligand is less lipophilic it will be confined inside the micelle Triton X-100, and thus it will quench the fluorescence. However, when the ligand binds with Hg²⁺ ions, the charged complex is released from the micelle and consequently the fluorescence will turn on. In the same paper, the authors presented other structure based on a turn off detection. In both cases the sensitivity was checked in the mg L⁻¹ Hg²⁺ concentration range and Ag⁺ ions acts as interferent. In the same manner, Zhao⁹² also employed micelles in order to overcome the deficiency of Dansyl group to be fluorescent in aqueous solution. The assay is focused on the Hg²⁺ detection and the influences over the sensitivity of the surfactants.

A complete study of fluorescent probe using micelles is reported by Wang⁹³. He employed three molecular probes derivated from 2-phenylbenzoxazole as hydrophobic fluorophore and a hydrophilic tetraamide Hg²⁺ ion receptor. These molecules can be incorporated into the hydrophobic sodium dodecyl sulfate micelle. The work is focused on

the behaviour of the micellar structures monitoring both UV/visible and fluorescence spectroscopy when Hg²⁺ binds in the three cases. This analysis revealed rather different spectrum both in absorbance and fluorescence. Moreover, the ratiometric fluorescence responses of two molecular probes described fingerprints for Hg²⁺. This characteristic was utilized so as to improve the selectivity by monitoring at a single wavelength ($\lambda = 380$ nm), wherein no signal changes from the presence of Cu²⁺ and Co²⁺ was observed. The authors concluded that sensitivity of the Hg²⁺ was amplified, and it was attributed to an increase in the presence of Hg²⁺ ion around the negatively charged micelle surface, which promotes complexation. Concentrations of Hg²⁺ can be detected in a range from 0.01 to 0.18 mg L⁻¹.

2.4.3 Optical bio-detection of mercury

It is relevant to comment the use of biomolecules, and especially, their role in the optical mercury detection. An advantage of biomolecules is their affinity to work in aqueous samples at neutral pH and under physiological conditions. Examples of mercury bio-recognition have been carried out by several types of receptors, including proteins, antibodies, DNA, oligonucleotides, and also bacterias. A strategy involving bio-detection is based on the principle that heavy metals ions can act as cofactors or inhibitors when they inter-actuate with proteins such as enzymes. A characteristic example is the inhibition of urease by mercury, wherein sulfhydryl groups bind with Hg²⁺. Thereafter, the

optical signal is labelled through catalytic activity of ureasa via pH or ammonia measurements. In this fashion, a sensitive dip-and-read test strip is disposed for mercury determination in aqueous samples⁹⁴. The strip is formed by a cellulose acetate membrane, onto which urease is immobilized, and a bottom layer is a pH indicator wafer that is impregnated with urea. A yellow spot on the pH indicator wafer disappears in the presence of mercury concentration. The response shows a low detection limit ($0.2 \mu\text{g L}^{-1}$) with a good selectivity in the presence of other metal ions. In the same manner, a monoclonal antibody functionalized with stilbenyl boronic acid cofactor is reported for a blue quenched fluorescence in presence of Hg^{2+} ions⁹⁵. Changes in the intensity emission at $\lambda=445 \text{ nm}$ are observable upper mercury levels of 0.8 mg L^{-1} . These fluorescent probe showed a high selectivity being only Pd^{2+} the most interferential ion.

DNA-functionalized gold nanoparticles have been assayed for a colorimetric mercury detection⁹⁶. The optical properties of this compound can be chemically programmed through the use of specific DNA interconnects, which allows to detect targets of interest. A reversible purple-to-red colour change is observable upon Hg^{2+} addition. The solutions are heated at $46 \text{ }^\circ\text{C}$ where the interaction with mercury is a maximum, being the detection limit around 0.02 mg L^{-1} of Hg^{2+} . The other metal ion that influences the response of the probe is Pb^{2+} .

The use of oligonucleotides as mercury receptors presents higher selectivity and sensitivity than most based on small molecular sensors. Another advantage of these receptors is that fluorescent emissions at several wavelengths can be used to indicate different metal ions through variation of the donor-acceptor combinations⁹⁷. Similarly, mercury ion detection has also been explored by the combination of a water-soluble conjugated polymer poly(3-(3'-N, N, N-triethylamino-1'-propyloxy)-4-methyl-2, 5-thiophene hydrochloride) with a mercury-specific oligonucleotide probe⁹⁸. The principle of detection takes advantage of the known ability of mercury ion to bind to thymine-thymine (T-T) dimers. Moreover, a combined optical detection of mercury ions can be done with the naked eye (LOD ~ 0.5 mg L⁻¹), and with more precision using a fluorimetric method (LOD ~ 8.4 µg L⁻¹). Water samples with concentrations of mercury induced a color change from red to yellow. Meanwhile, the colorimetric detection showed a very high selectivity to mercury without any appreciable disturbance of other ions, the fluorimetric response was slightly influenced by the presence of Zn²⁺, Co²⁺, Mn²⁺, Cu²⁺, and Pb²⁺.

The quantification of bioavailable mercury can also be afforded through a whole-cell, luminiscence-based bacterial sensor. The system is constructed at the genetic level by fusing a mercury inducible operon (which provides for the mercury recognition) with a mercury transport system (in order to increase the concentration of bioavailable mercury, therefore enhancing the sensitivity of the system) and a promoterless

luminescence gene (which provides for the luminescence response). In these bacterial sensors, the Hg^{2+} present in the environment is transported to the cytoplasm of the bacteria, wherein a modified genetic chain is responsible of the activation of a luminescent protein when mercury is present. The lowest detectable concentration of Hg^{2+} was 0.4 ng L^{-1} , so therefore the sensitivity of the system is below most common biosensors and molecular probes⁹⁹.

2.4.4 Optical mercury detection by advanced materials

Great advances in the field of new materials have allowed compensating most of the weakness of the chemical sensors. In the last years, several attempts to develop robust materials to overcome some of the chemical sensors disadvantages have been explored. A step forward has been achieved by the immobilization of dyes onto a support. Typically, the immobilization of the indicator is achieved by adsorption, chemical bonding or physical entrapment into the support materials, such as polymers, membranes, films, and functionalized nanoparticles. For example, test strips based in a cubic nanostructured cage-based optical probe have been designed in order to enhance the sensitivity and selectivity of the system, making possible the naked-eye detection at low level concentrations of heavy metal ions¹⁰⁰. Each cage incorporates spherical nanosized cavities with a high adsorption capacity of molecular

dyes among them dithizone. The structure allows a high diffusion, so that the times for metal ion determination decrease. A visual detection of Pb²⁺, Cd²⁺, Sb³⁺ and Hg²⁺ brings to colour changes of the test strips with a detection limit of 0.5, 1.5, 4.1, and 1.27 µg L⁻¹.

An emerging material with an extensive range of applications are quantum dots. These semiconductor nanocrystals have special optical properties, such as narrow and tunable fluorescence, strong emission and photochemical stability. They can be as small as 20 to 10 nanometers, and its surface can be functionalized with binding receptor moieties, being the fluorescence sensitive to those species adsorbed. Obviously, this fact makes the use of quantum dots an interesting platform for fluorescence transduction originated by molecular recognition. Therefore, Hg²⁺ detection has been carried out by quantum dots in several papers. First, Chen¹⁰¹ functionalized CdSe nanoclusters with L-cysteine which exhibited strong specific affinity for Hg²⁺. The diameters of the treated quantum dots were from 5 to 10 nm, being water-soluble, wherein a fluorescence quenching phenomenon was observed in the presence of Hg²⁺ ions. In comparison with conventional organic fluorophores, the quantum dots possessed strong luminescence and more stability against photobleaching. The limit of detection was 1.2 µg L⁻¹ Hg²⁺ in buffered aqueous solution at pH 7.75. The selectivity showed by the functionalized was quiet high and small fluorescence changes around 5% were observed in the presence of Cu²⁺ and Cd²⁺.

Recently, in a similar fashion Li and coworkers have reported luminescent quantum dots capped with L-carnitine for Hg^{2+} detection¹⁰². The authors suppose that the mercury acts as a quencher of the luminescence through electron transfer from surface traps of quantum dots to Hg^{2+} . Moreover, the surface ligands have effect over the fluorescence, and principally they take role in the selectivity, preventing influence from other metal ions. The detection limit of these nanostructures is $36.1 \mu\text{g L}^{-1}$ of Hg^{2+} , being only Ag^+ and Fe^{2+} the most interferential ions. The drawback of this method is that the quantum dots were only assayed in ethanol solutions and it is suspected that the optical nanoparticles properties are not stable in aqueous solution.

Gold nanoparticles (AuNPs) take an important role in the metal ion detection because they show greater quenching properties than typical small molecular quenchers. So that, in comparison with conventional fluorimetric detection of metal ions, these structures endow higher sensitivity. Consequently, the detection of Hg^{2+} in aqueous solution is afforded via Rhodamine B (RB) adsorbed on the surface of AuNPs¹⁰³. In this stage, the emission of RB is weak due to resonance energy transfer and collision with AuNP. The addition of Hg^{2+} releases RB molecules from AuNP and thus the fluorescent is enhanced. Several thiols ligands were proved with this structure in order to promote Hg^{2+} selectivity, and the detection limit was $2 \mu\text{g L}^{-1}$. In a subsequent work, the same receptor is further studied and applied to mercury detection in soil, water, and fish¹⁰⁴. An improved sensitivity is achieved by using a green laser ($\lambda =$

532 nm) as excitation light source, being possible the detection of 2 ng L⁻¹ of Hg²⁺ concentrations. Gold nanoparticle with Rhodamine 6G have also been used for Hg²⁺ detection¹⁰⁵. Reported results showed also very high sensitivity to Hg²⁺ ions, with a detection limit of 12 ng L⁻¹ and good selectivity appearing a weakly response to Cd²⁺ and Pb²⁺.

A further study reported by Huang¹⁰⁶ remarked a number of attractive optical properties of modified AuNPs for fluorescence emission. These nanoparticles exhibits size-dependent surface plasmon resonance when their dimensions are smaller than the electron mean free path (~20nm). Rarely, the fluorescence phenomena of AuNPs have been applied to chemical sensing, mainly because of problems associated with their chemical and fluorescence instability. The authors promote stable fluorescence properties by encapsulating AuNPs with polyamidoamine dendrimers. The dendrimer cage enhances the quantum yields and prevents from quenchers present in solution. Moreover, the addition of alkanethiol ligands onto the surface of 3 nm AuNPs can control the fluorescence properties (excitation and emission wavelengths, and quantum yield). Thereafter, by functionalizing protected AuNPs with 11-mercaptoundecanoic acid an assay for Hg²⁺ detection is carried out. Herein, Hg²⁺ ion acts as an induced quencher for fluorescence. The selectivity of the method was high except for Pb²⁺ and Cd²⁺ ions, and a detection limit of 1 µg L⁻¹ (Hg²⁺) was observed.

Table 2-IV resumes the examples exposed in this section for the mercury recognition by opto-chemical probes.

TABLE 2-IV. Mercury detection examples by opto-chemical probes

Reagent	Method	Working conditions	LOD (ppm)	Interferences	Reversibility
1,5-Diphenylthiocarbazone/triacetylcellulose ⁶⁷	Absorbance	pH 2	2×10^{-3} 2×10^{-2} (film)	Cu ²⁺	Yes, with KI
TTPS with TMAC on mesoporous silica ⁶⁸	Colorimetric	pH 9	3.5×10^{-3}	Zn ²⁺ , Ni ²⁺ , Pb ²⁺ , Cu ²⁺ , Fe ³⁺	--
2-mercapto-2-thiazoline and ETH5294 on plasticized PVC membrane ⁶⁹	Absorbance	pH 7	40×10^{-6}	Ag ⁺	Yes with HNO ₃
4-(diethylamino)benzaldehyde ⁷⁰	Colorimetric	pH 7	5	--	Yes, thiourea
Trityl-picolinamide on plasticized PVC ⁷³	Absorbance	pH 4	0.1	Ag ⁺ , Pb ²⁺ , Ni ²⁺ , Cu ²⁺	No
5,10,15,20-tetraphenylporphyrin on plasticized PVC ⁷⁴	Fluorescence TURN OFF	pH 8	8×10^{-3}	None	Yes, with blank buffer
5,10,15,20-tetraphenylporphyrin on sol-gel matrix ⁷⁵	Fluorescence TURN OFF	pH 8	0.7	None	Yes, with blank buffer
5,10,15-tris(pentafluorophenyl)corrole on plasticized PVC membrane ⁷⁶	Fluorescence TURN OFF	pH 6	0.02	--	Yes, with blank buffer
Thiacalix [4]arene derivative with 8-hydroxyquinoline ⁷⁹	Fluorescence TURN OFF	H ₂ O (10%)-THF solution	0.4	Ag ⁺	--
Thiosemicarbazole ⁸⁰	Fluorescence TURN ON	pH 7.4	0.02	Zn ²⁺ , Ag ⁺	No

Reagent	Method	Working conditions	LOD (ppm)	Interferences	Reversibility
Tetra-2-pyridylthiocarbazon ⁸¹	Fluorescence TURN ON	H ₂ O/ CH ₃ OH	--	Cu ²⁺	No
D-glucosamine linked to 2-quinolinecarboxaldehyde ⁸²	Fluorescence TURN ON	pH 5 – 7.5	0.10	Cu ²⁺	--
2,4-bis(4-dialkylaminophenyl)-3-hydroxy-4-alkylsulfanylcyclobut-2-enone ⁸³	Colorimetric and fluorescent TURN ON	water/acetone nitrile (4:1 v/v) pH 9.6	<20 ppb and <2 ppb	None	Yes, propane thiol
Carbohydrazone block with Rhodamine 6G ⁸⁴	Fluorescence TURN ON	DMF – H ₂ O, pH 5-10	2x10 ⁻³	None	--
Thioether-rich with rhodamine fluorophore ⁸⁵	Fluorescence TURN ON	pH 7.0	2x10 ⁻³	Fe ²⁺ , Fe ³⁺ , Co ²⁺ and Cd ²⁺	--
Thiosemicarbazide ⁸⁶	Fluorescence TURN ON	ETOH- H ₂ O (30/70, v/ v)	1.7x10 ⁻²	Ag ⁺	--
Dithiocarbamates ligands linked to an anthracene group ⁸⁷	Ratiometric fluorescence	water- acetonitrile (1:1, v/ v)	2x10 ⁻³	Ag ⁺	--
Seminaphthofluorescein with thioether-rich ⁸⁸	Ratiometric fluorescence	pH 7-9	1x10 ⁻³	Cu ²⁺	Yes, with TPEN or KI
Boradiazaindacene with two crown ether ligands ⁸⁹	Ratiometric fluorescent and absorbance	THF-H ₂ O, pH 7.2	1.6 (Fl.) 3 (Ab.)	None	--
2-phenylbenzoxazole with tetraamide derivatives ⁹³	Ratiometric fluorescence, micelles	Water pH 7.1 / sodium dodecyl sulfate	0.01	Cu ²⁺ , Co ²⁺	No
Urease on cellulose acetate ⁹⁴	Colorimetric, biodection	pH 7.6	0.2x10 ⁻³	Cu ²⁺	--
Antibody with stilbenyl boronic acid ⁹⁵	Turn off fluorescence, biodection-	pH 7.4	0.8	Pd ²⁺	No
DNA-functionalized gold nanoparticles ⁹⁶	Colorimetric, biodection	46°C	0.02	Pb ²⁺	Yes

Reagent	Method	Working conditions	LOD (ppm)	Interferences	Reversibility
Oligonucleotide probe with conjugated polymer ⁹⁸	Turn off Fluorescence and colorimetric, biodetection	pH 6	8.4x10 ⁻³ (Fl.) and 0.5 (Ab.)	Zn ²⁺ , Co ²⁺ , Mn ²⁺ , Cu ²⁺ and Pb ²⁺	No
E. coli XL1-Blue with plasmid pMQT ⁹⁹	Turn off Fluorescent, biodetection	--	0.4x10 ⁻⁶	None	No
Tetraphenylporphine tetrasulfonic acid on nanostructured cage ¹⁰⁰	Colorimetric, Advanced nanomaterial	pH 9	1.27x10 ⁻³	--	Partially with chelator
Quantum dots functionalized with L-cysteine ¹⁰¹	Fluorimetric, Advanced nanomaterial	pH 7.75	1.2x10 ⁻³	Cu ²⁺ and Cd ²⁺	--
Quantum dots capped with L-carnitine ¹⁰²	Turn off Fluorescence, Advanced nanomaterial	--	36.1 x10 ⁻³	Ag ⁺ and Fe ²⁺	--
AuNPs with Rhodamine B and thiols ligands ¹⁰⁴	Turn off Fluorescence, Advanced nanomaterial	--	2x10 ⁻⁶	--	--
AuNPs with Rhodamine 6G ¹⁰⁵	Turn off Fluorescence, Advanced nanomaterial	--	12x10 ⁻⁶	Cd ²⁺ and Pb ²⁺	--
Encapsulated AuNPs with polyamidoamine dendrimers ¹⁰⁶	Turn off Fluorescence, Advanced nanomaterial	--	1x10 ⁻³	Pb ²⁺ and Cd ²⁺	--

2.5 Colorimetric Mercury Determination By N719

The main purpose of the design of the N719 (=bis(2,2'-bipyridyl-4,4'-dicarboxylato) ruthenium(II) bis-tetrabutylammonium bis-thiocyanate) (see structure in Figure 2.14) was to optimise it for dye solar cell uses¹⁰⁷.

For these kind of applications, the molecule is anchored onto a TiO_2 film which acts as a semiconductor layer. In these systems the dye injects electrons to the semiconductor surface once light incides on it. The similitude of its structure to other receptors for mercury binding and its ability to be anchored onto metal oxide films encouraged Emilio Palomares et al. to explore the utility of N719 as a molecular probe for mercury ions. Consequently, they reported a naked-eye colorimetric dip-sensor for mercury in aqueous solution by using dye-sensitized nanocrystalline TiO_2 films¹⁰⁸.

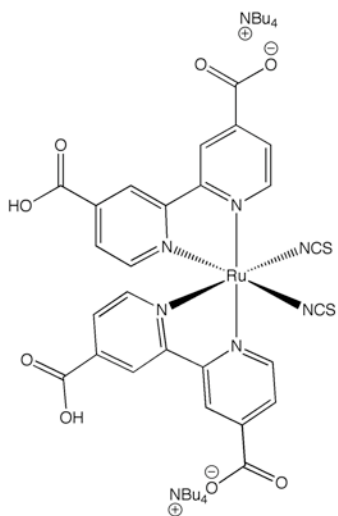


Figure 2.14. Structure of the Ru(II)-complex (N719)

The dye changes its colour from dark red-purple to orange in presence of mercury ions, and naked-eye detection is possible down to 20 mg L^{-1} of Hg^{2+} . The spectrophotometric detection allows to sense $\sim 0.5 \text{ mg L}^{-1}$ of Hg^{2+} when the dye is immobilized onto titania films, and even a limit of detection of $\sim 20 \text{ } \mu\text{g L}^{-1}$ of Hg^{2+} is possible, in N719 ethanol dissolution

and ideal conditions, in other words in absence of interference. The high performance of the chemical probe and its possibilities to explore a commercial application promoted to the authors to protect this mercury detection method with a patent¹⁰⁹.

Thereafter, a further study demonstrated that the colour change is indeed a consequence of the direct coordination of Hg^{2+} ions to the sulfur atoms of the NCS groups¹¹⁰. The photophysical interpretation could be based on that the NCS groups act as charge donors to the ruthenium(II) complex. A higher charge transfer produces an increment of the energy level corresponding to the higher occupied molecular orbital (HOMO), what can be interpreted as a minor energy differential. Upon interaction of mercury with NCS groups, a reduction of the charge transfer to ruthenium complex occurs and subsequently the energy differential increases. Accordingly to the relationship $E = h c/\lambda$, if energy increases, the spectrum shifts to lower wavelengths. This fact explains the new-formed mercury complexation band between $\lambda=425\text{-}500$ nm. Moreover, the colour change was found irreversible and persisting for several weeks. In Figure 2.15, the X-ray structure reflects how the mercury atoms are anchored to the sulphurs atoms. All thiocyanate ligands from the ruthenium complexes coordinate also to a mercury atom, with S1 coordinating only Hg1 positions, and with S2 coordinating either Hg1 or Hg2, depending on the local distribution. Figure 2.16 represents the sequence of mercury acetate additions (in aqueous solution) and the

spectral response of N719 registered in a Shimadzu 1700. The spectral absorbance shows a peak around $\lambda = 535$ nm which is responsible of the dark red-purple tone of the molecule, and when mercury is added this peak shifts to orange region ($\lambda = 470$ nm).

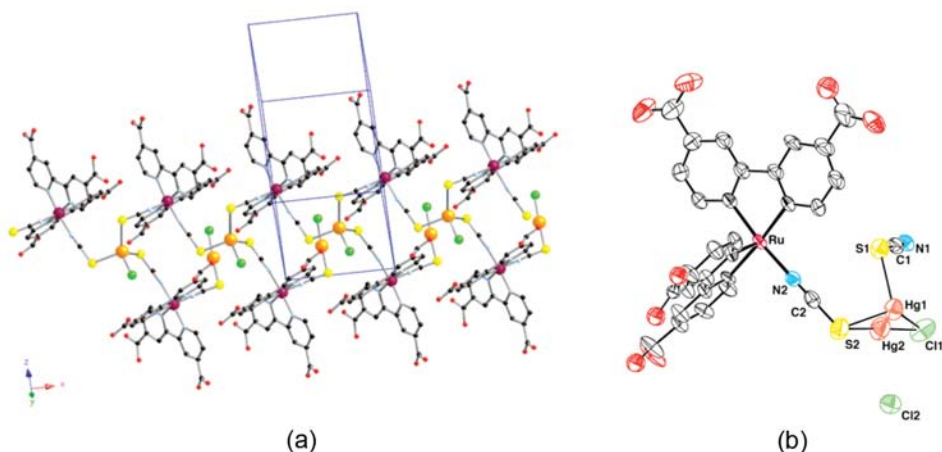


Figure 2.15. Three dimensional X-ray structure of the N719- $HgCl_2$ complex. (a) Representation of the $[Ru(N_2C_{12}O_4H_8)_2(NCS)_2HgCl]_n^{n+}$ chains, (b) asymmetric unit which shows the mercury coordinating to the sulfur of the NCS groups.

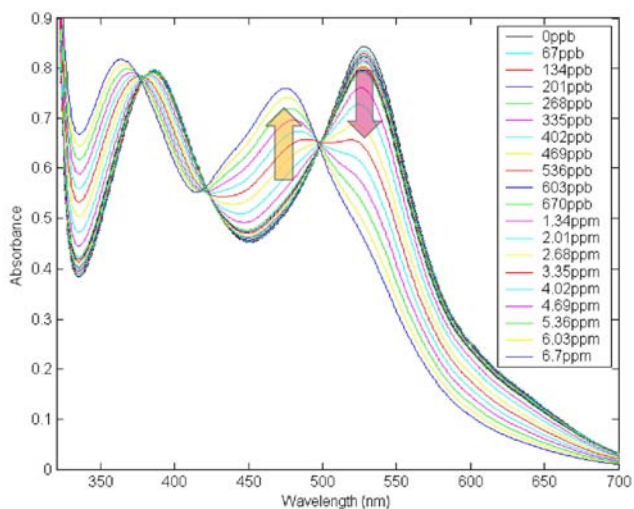


Figure 2.16. Spectral response of $Hg(II)$ titration in N719 ($10^{-4}M$) ethanol dissolution.

Afterwards, in depth studies allowed a mercury scavenging method with mesoporous TiO₂/N719 films¹¹¹. Mercury scavenging materials should accomplish several requirements which are similar to mercury sensors: (1) they have to be highly selective for mercury, (2) they have to be efficient even at low concentrations of mercury, (3) the scavenging material has to be cheap and easily prepared on a multi-gram scale, and (4) the mercury scavenging must be reversible. Herein, it is demonstrated the reversibility of the films using 10 mM KI solution, which can be used at least four times retaining more than 80% of the scavenging activity towards mercury even in the presence of other metal ions. The results showed a practical approach for mercury removal from water at a high efficiency.

Afterwards, Nazeeruddin noted that some leaching of the reported Ru(II) complexes-titania films occurred upon exposure to water. Thus, they developed a modified ruthenium complex based in amphiphilic sensitizers¹¹². These chains act as linkers between carboxylate groups and the oxide surface, thus the resulted molecule is hydrophobic and does not desorb from titania surface. Moreover, they presented fluorometric and electrochemical properties of the new compound. Another approach in order to solve the de-absorption problems, is to assay other metal oxides. This way, the recent advances made at Institute of Chemical Research of Catalonia have shown the good optical properties of functionalized Al₂O₃ nanoparticles, with practically no dye desorption. This is a promising method that will open good possibilities towards a full-integrated optical

probe. As a first step, a good approach is to study in depth the possibilities of the spectral analysis and later compare the several effects introduced by for example optical supports, ionic interference or other non-linearities. Accordingly, the next chapters explain an experimental procedure and chemometric methods in order to improve the selectivity of N719 dissolution towards mercury ions, even in presence of potential interferents.

2.6 References

- (1) Wolfbeis, O. S. *Analytical Chemistry* **2006**, 78, 3859-3873.
- (2) Saliterman, S. *Fundamentals of bioMEMS and medical microdevices*; SPIE- The International Society for Optical Engineering: Bellingham, Washington, 2006.
- (3) Vlasov, Y. G.; Legin, A. V.; Rudnitskaya, A. M.; D'Amico, A.; Di Natale, C. *Sensors and Actuators, B: Chemical* **2000**, B65, 235-236.
- (4) Skov, T.; Bro, R. *Sensors and Actuators, B: Chemical* **2005**, B106, 719-729.
- (5) Naganawa, R.; Hirayama, K.; Noda, K.; Kurosawa, S.; Tao, H. *Chemical Sensors* **2004**, 20, 672-673.
- (6) Yajima, S.; Suzuki, K.; Kimura, K. *Analytical Sciences* **2000**, 16, 899-900.

- (7) Senillou, A.; Jaffrezic-Renault, N.; Martelet, C.; Griffe, F. *Materials Science & Engineering, C: Biomimetic Materials, Sensors and Systems* **1998**, *C6*, 59-63.
- (8) Safavi, A.; Maleki, N.; Rostamzadeh, A.; Maesum, S. *Talanta* **2007**, *71*, 498-501.
- (9) Wang, E.; Chow, K.-F.; Kwan, V.; Chin, T.; Wong, C.; Bocarsly, A. *Analytica Chimica Acta* **2003**, *495*, 45-50.
- (10) Sohn, B.-K.; Kim, C.-S. *Sensors and Actuators, B: Chemical* **1996**, *B34*, 435-440.
- (11) Butler, T. M.; MacCraith, B. D.; McDonagh, C. M. *Proceedings of SPIE-The International Society for Optical Engineering* **1995**, *2508*, 168-178.
- (12) Basheer, M. P.; Grattan, K. T. V.; Sun, T.; Long, A. E.; McPolin, D.; Xie, W. *Proceedings of SPIE-The International Society for Optical Engineering* **2004**, *5586*, 144-153.
- (13) Dong, B.; Yang, T.; Lei, M. K. *Sensors and Actuators, B: Chemical* **2007**, *B123*, 667-670.
- (14) Guo, H.; Tao, S. *IEEE Sensors Journal* **2007**, *7*, 953-954.
- (15) Joo, S.; Brown, R. B. *Chemical Reviews (Washington, DC, United States)*, ACS ASAP.
- (16) Buck, R. P.; Hackleman, D. E.; Kenan, W. R., Jr. *Analytical Chemistry* **1977**, *49*, 2315-2321.
- (17) Amini, N.; Cardwell, T. J.; Cattrall, R. W.; Kolev, S. *Analytica Chimica Acta* **2005**, *539*, 203-207.
- (18) Mazloun, M.; Amini, M. K.; Mohammadpoor-Baltork, I. *Sensors and Actuators, B: Chemical* **2000**, *B63*, 80-85.

- (19) Zhu, X.-s.; Gao, C.; Choi, J.-W.; Bishop, P. L.; Ahn, C. H. *Lab on a Chip* **2005**, *5*, 212-217.
- (20) Kuhlman, G. M.; Keymeulen, D.; Buehler, M. G. *IEEE Aerospace Conference Proceedings* **2004**, 363-367.
- (21) Ordeig, O.; Banks, C. E.; del Campo, J.; Munoz, F. X.; Compton, R. G. *Electroanalysis* **2006**, *18*, 573-578.
- (22) Keebaugh, S.; Kalkan, A. K.; Nam, W. J.; Fonash, S. J. *Electrochemical and Solid-State Letters* **2006**, *9*, H88-H91.
- (23) Ben Ali, M.; Homri, T.; Korpan, Y.; Abdelgani, A.; Ali Maaref, M.; Liu, L.; Jaffrezic-Renault, N.; Martelet, C. *Materials Science & Engineering, C: Biomimetic and Supramolecular Systems* **2006**, *26*, 149-153.
- (24) Wang, H. T.; Kang, B. S.; Chancellor, T. F., Jr.; Lele, T. P.; Tseng, Y.; Ren, F.; Pearton, S. J.; Dabiran, A.; Osinsky, A.; Chow, P. P. *Electrochemical and Solid-State Letters* **2007**, *10*, J150-J153.
- (25) Martin, S. J.; Granstaff, V. E.; Frye, G. C. *Analytical Chemistry* **1991**, *63*, 2272-2281.
- (26) Eichelbaum, F.; Borngraeber, R.; Lucklum, R.; Hauptmann, P.; Roesler, S. *Technisches Messen* **1998**, *65*, 434-444.
- (27) Hartmann, J.; Auge, J.; Lucklum, R.; Roesler, S.; Hauptmann, P.; Adler, B.; Dalcanale, E. *Sensors and Actuators, B: Chemical* **1996**, *B34*, 305-311.
- (28) Cherian, S.; Gupta, R. K.; Mullin, B. C.; Thundat, T. *Biosensors & Bioelectronics* **2003**, *19*, 411-416.
- (29) Boisdé, G. *Chemical and Biochemical Sensing With Optical Fibers and Waveguides*; Artech House: Norwood, 1996.

- (30) Savvate'ev, V.; Chen-Esterlit, Z.; Aylott, J. W.; Choudhury, B.; Kim, C. H.; Zou, L.; Friedl, J. H.; Shinar, R.; Shinar, J.; Kopelman, R. *Applied Physics Letters* **2002**, *81*, 4652-4654.
- (31) Valeur, B. *Molecular Fluorescence: Principles and Applications*; Wiley-VCH, 2001.
- (32) Snyder, A. W. *Optical Waveguide Theory*; Chapman and Hall: London, 1983.
- (33) Kelly, M. J.; Sweatt, W. C.; Kemme, S. A.; Kasunic, K. J.; Blair, McNeil, J. R.; Burgess, L. W.; Brodsky, A. M.; Smith, S. A. In *Sandia Reports*; Sandia National Laboratories: Alburqueque, Livermore, 2000.
- (34) Sohn, Y.-S.; Goodey, A.; Anslyn, E. V.; McDevitt, J. T.; Shear, J. B.; Neikirk, D. P. *Biosensors & Bioelectronics* **2005**, *21*, 303-312.
- (35) Puyol, M.; Valle, M. d.; Garces, I.; Villuendas, F.; Dominguez, C.; Alonso, J. *Analytical Chemistry* **1999**, *71*, 5037-5044.
- (36) Lucotti, A.; Zerbi, G. *Sensors and Actuators, B: Chemical* **2007**, *121*, 356-364.
- (37) Yuan, L.-B.; Zhou, L.-M.; Wu, J.-S. *Sensors and Actuators, A: Physical* **2000**, *A86*, 2-7.
- (38) Zhang, Y.; Shibru, H.; Cooper, K. L.; Wang, A. *Optics Letters* **2005**, *30*, 1021-1023.
- (39) Sharma, A. K.; Gupta, B. D. *Photonics and Nanostructures - Fundamentals and Applications* **2005**, *3*, 30-37.
- (40) Arregui, F. J.; Matías, I. R.; Cooper, k. L.; Claus, R. O. *IEEE Sensors Journal* **2002**, *2*, 482-487.
- (41) Ertas, N.; Akkaya, E. U.; Yavuz Ataman, O. *Talanta* **2000**, *51*, 693-699.

- (42) Kuswandi, B.; Narayanaswamy, R. *Sensors and Actuators, B: Chemical* **2001**, *B74*, 131-137.
- (43) Suresh Kumar, P.; Thomas Lee, S.; Vallabhan, C. P. G.; Nampoore, V. P. N.; Radhakrishnan, P. *Optics Communications* **2002**, *214*, 25-30.
- (44) Lee, S. T.; Kumar, P. S.; Unnikrishnan, K. P.; Nampoore, V. P. N.; Vallabhan, C. P. G.; Sugunan, S.; Radhakrishnan, P. *Measurement Science and Technology* **2003**, *14*, 858-861.
- (45) Madden, J. E.; Cardwell, T. J.; Cattrall, R. W.; Deady, L. W. *Analytica Chimica Acta* **1996**, *319*, 129-134.
- (46) Kuswandi, B.; Narayanaswamy, R. *Journal of Environmental Monitoring* **1999**, *1*, 109-114.
- (47) Kuswandi, B.; Narayanaswamy, R. *Quimica Analitica (Barcelona)* **2000**, *19*, 87-93.
- (48) Baldini, F.; Falai, A.; Flamini, A.; Mencaglia, A. A. *Proceedings of SPIE-The International Society for Optical Engineering* **1999**, *3540*, 191-195.
- (49) Kuswandi, B.; Taib, M. N.; Narayanaswamy, R. *Sensors and Actuators, A: Physical* **1999**, *A76*, 183-190.
- (50) Yeh, T.-C.; Tien, P.; Chau, L.-K. *Applied Spectroscopy* **2001**, *55*, 1320-1326.
- (51) Miled, O. B.; Sanchez, C.; Livage, J. *Journal of Materials Science* **2005**, *40*, 4523-4530.
- (52) Antico, E.; Lerchi, M.; Rusterholz, B.; Achermann, N.; Badertscher, M.; Valiente, M.; Pretsch, E. *Analytica Chimica Acta* **1999**, *388*, 327-338.


- (53) Chan, W.-H.; Yang, R.-H.; Mo, T.; Wang, K.-M. *Analytica Chimica Acta* **2002**, *460*, 123-132.
- (54) Ensafi, A. A.; Isfahani, Z. N. *IEEE Sensors Journal* **2007**, *7*, 1112-1117.
- (55) Takahashi, Y.; Hayashita, T.; Suzuki, T. M. *Analytical Sciences* **2007**, *23*, 147-150.
- (56) Scindia, Y. M.; Pandey, A. K.; Reddy, A. V. R.; Manohar, S. B. *Analytica Chimica Acta* **2004**, *515*, 311-321.
- (57) Gueell, R.; Fontas, C.; Salvado, V.; Antico, E. *Analytica Chimica Acta* **2007**, *594*, 162-168.
- (58) Safavi, A.; Bagheri, M. *Sensors and Actuators, B: Chemical* **2005**, *B107*, 53-58.
- (59) Yari, A.; Afshari, N. *Sensors and Actuators, B: Chemical* **2006**, *B119*, 531-537.
- (60) Luo, H.-Y.; Zhang, X.-B.; Jiang, J.-H.; Li, C.-Y.; Peng, J.; Shen, G.-L.; Yu, R.-Q. *Analytical Sciences* **2007**, *23*, 551-555.
- (61) Safavi, A.; Sadeghi, M. *Talanta* **2007**, *71*, 339-343.
- (62) Rastegarzadeh, S.; Rezaei, V. *Sensors and Actuators, B: Chemical* **2008**, *129*, 327-331.
- (63) Cabanero Ortiz, A. I.; Madrid Albarran, Y.; Camara Rica, C. *Journal of Analytical Atomic Spectrometry* **2002**, *17*, 1595-1601.
- (64) Cava-Montesinos, P.; Dominguez-Vidal, A.; Cervera, M. L.; Pastor, A.; de la Guardia, M. *Journal of Analytical Atomic Spectrometry* **2004**, *19*, 1386-1390.
- (65) Pereiro, I. R.; Wasik, A.; Lobinski, R. *Journal of Analytical Atomic Spectrometry* **1998**, *13*, 743-747.

- (66) Yallouz, A. V.; Calixto de Campos, R.; Paciornik, S. *Fresenius' Journal of Analytical Chemistry* **2000**, 366, 461-465.
- (67) Safavi, A.; Bagheri, M. *Sensors and Actuators, B: Chemical* **2004**, B99, 608-612.
- (68) Balaji, T.; Sasidharan, M.; Matsunaga, H. *Analyst (Cambridge, United Kingdom)* **2005**, 130, 1162-1167.
- (69) Amini, M. K.; Khezri, B.; Firooz, A. R. *Sensors and Actuators, B: Chemical* **2007**, doi:10.1016/j.snb.2007.12.008.
- (70) Fu, Y.; Li, H.; Hu, W. *European Journal of Organic Chemistry* **2007**, 2459-2463.
- (71) Ho, I. T.; Lee, G.-H.; Chung, W.-S. *Journal of Organic Chemistry* **2007**, 72, 2434-2442.
- (72) Gruener, B.; Mikulasek, L.; Baca, J.; Cisarova, I.; Boehmer, V.; Danila, C.; Reinoso-Garcia, M. M.; Verboom, W.; Reinhoudt, D. N.; Casnati, A.; Ungaro, R. *European Journal of Organic Chemistry* **2005**, 2022-2039.
- (73) Kuswandi, B.; Nuriman; Dam, H. H.; Reinhoudt, D. N.; Verboom, W. *Analytica Chimica Acta* **2007**, 591, 208-213.
- (74) Chan, W. H.; Yang, R. H.; Wang, K. M. *Analytica Chimica Acta* **2001**, 444, 261-269.
- (75) Guo, L.; Zhang, W.; Xie, Z.; Lin, X.; Chen, G. *Sensors and Actuators, B: Chemical* **2006**, B119, 209-214.
- (76) He, C.-L.; Ren, F.-L.; Zhang, X.-B.; Han, Z.-X. *Talanta* **2006**, 70, 364-369.
- (77) Kwon, J. Y.; Soh, J. H.; Yoon, Y. J.; Yoon, J. *Supramolecular Chemistry* **2004**, 16, 621-624.

- (78) Chen, Q.-Y.; Chen, C.-F. *Tetrahedron Letters* **2004**, *46*, 165-168.
- (79) Praveen, L.; Ganga, V. B.; Thirumalai, R.; Sreeja, T.; Reddy, M. L. P.; Varma, R. L. *Inorganic Chemistry (Washington, DC, United States)* **2007**, *46*, 6277-6282.
- (80) Ko, S.-K.; Yang, Y.-K.; Tae, J.; Shin, I. *Journal of the American Chemical Society* **2006**, *128*, 14150-14155.
- (81) Zhao, Y.; Lin, Z.; He, C.; Wu, H.; Duan, C. *Inorganic Chemistry* **2006**, *45*, 10013-10015.
- (82) Ou, S.; Lin, Z.; Duan, C.; Zhang, H.; Bai, Z. *Chemical Communications (Cambridge, United Kingdom)* **2006**, 4392-4394.
- (83) Ros-Lis, J. V.; Marcos, M. D.; Martinez-Manez, R.; Rurack, K.; Soto, J. *Angewandte Chemie, International Edition* **2005**, *44*, 4405-4407.
- (84) Wu, D.; Huang, W.; Duan, C.; Lin, Z.; Meng, Q. *Inorganic Chemistry* **2007**, *46*, 1538-1540.
- (85) Yoon, S.; Miller, E. W.; He, Q.; Do, P. H.; Chang, C. J. *Angewandte Chemie, International Edition* **2007**, *46*, 6658-6661.
- (86) Yang, X.-F.; Li, Y.; Bai, Q. *Analytica Chimica Acta* **2007**, *584*, 95-100.
- (87) Cheung, S.-M.; Chan, W.-H. *Tetrahedron* **2006**, *62*, 8379-8383.
- (88) Nolan, E. M.; Lippard, S. J. *Journal of the American Chemical Society* **2007**, *129*, 5910-5918.
- (89) Yuan, M.; Li, Y.; Li, J.; Li, C.; Liu, X.; Lv, J.; Xu, J.; Liu, H.; Wang, S.; Zhu, D. *Organic Letters* **2007**, *9*, 2313-2316.

- (90) Pallavicini, P.; Diaz-Fernandez, Y. A.; Foti, F.; Mangano, C.; Patroni, S. *Chemistry--A European Journal* **2006**, *13*, 178-187.
- (91) Khan, H.; Ahmed, M. J.; Bhangar, M. I. *Analytical Sciences* **2005**, *21*, 507-512.
- (92) Zhao, Y.; Zhong, Z. *Organic Letters* **2006**, *8*, 4715-4717.
- (93) Wang, J.; Qian, X.; Qian, J.; Xu, Y. *Chemistry--A European Journal* **2007**, *13*, 7543-7552.
- (94) Guo-quing, S.; Guibin, J. *Analytical Sciences* **2002**, *18*, 1215-1219.
- (95) Matsushita, M.; Meijler, M. M.; Wirsching, P.; Lerner, R. A.; Janda, K. D. *Organic Letters* **2005**, *7*, 4943-4946.
- (96) Lee, J.-S.; Han, M. S.; Mirkin, C. A. *Angewandte Chemie, International Edition* **2007**, *46*, 4093-4096.
- (97) Ono, A.; Togashi, H. *Angewandte Chemie, International Edition* **2004**, *43*, 4300-4302.
- (98) Liu, X.; Tang, Y.; Wang, L.; Zhang, J.; Song, S.; Fan, C.; Wang, S. *Advanced Materials (Weinheim, Germany)* **2007**, *19*, 1471-1474.
- (99) Omura, T.; Kiyono, M.; Pan-Hou, H. *Journal of Health Science* **2004**, *50*, 379-383.
- (100) Balaji, T.; El-Safty, S. A.; Matsunaga, H.; Hanaoka, T.; Mizukami, F. *Angewandte Chemie, International Edition* **2006**, *45*, 7202-7208.
- (101) Chen, J.; Gao, Y.; Xu, Z.; Wu, G.; Chen, Y.; Zhu, C. *Analytica Chimica Acta* **2006**, *577*, 77-84.
- (102) Li, H.; Zhang, Y.; Wang, X.; Gao, Z. *Microchimica Acta* **2008**, *160*, 119-123.

- (103) Huang, C.-C.; Chang, H.-T. *Analytical Chemistry* **2006**, *78*, 8332-8338.
- (104) Darbha, G. K.; Ray, A.; Ray, P. C. *ACS Nano* **2007**, *1*, 208-214.
- (105) Chen, J.; Zheng, A.; Chen, A.; Gao, Y.; He, C.; Kai, X.; Wu, G.; Chen, Y. *Analytica Chimica Acta* **2007**, *599*, 134-142.
- (106) Huang, C.-c.; Yang, Z.; Lee, K.-H.; Chang, H.-T. *Angewandte Chemie, International Edition* **2007**, *46*, 6824-6828.
- (107) Graetzel, M.; Nazeeruddin, M. K.; (Ecole Polytechnique Federale de Lausanne (EPFL), Switz.). Application: WO 93-EP2221 9404497, 1994.
- (108) Palomares, E.; Vilar, R.; Durrant, J. R. *Chemical Communications (Cambridge, United Kingdom)* **2004**, 362-363.
- (109) Coronado, E.; Galan-Mascaros, J. R.; Marti-Gastaldo, C.; Palomares, E.; Durrant, J. R.; Vilar, R.; Gratzel, M.; Nazeeruddin, M. K. *Journal of the American Chemical Society* **2005**, *127*, 12351-12356.
- (110) Durrant, J.; Palomares, E.; Vilar, R.; (Imperial College Innovations Limited, UK). Application: US 2005-169881 2006144720, 2006.
- (111) Li, X.; Perez-Hernandez, J.; Haque, S. A.; Durrant, J. R.; Palomares, E. *Journal of Materials Chemistry* **2007**, *17*, 2028-2032.
- (112) Nazeeruddin, M. K.; Di Censo, D.; Humphry-Baker, R.; Gratzel, M. *Advanced Functional Materials* **2006**, *16*, 189-194.



3 Multivariate Calibration: Hg²⁺ Detection And The Enhancement Of N719 Selectivity

CONTENTS

- 3. 1 Introduction to multivariate calibration.
- 3. 2 Enhancement techniques for multivariate linear regression.
- 3. 3 Selectivity enhancement and quantification of Hg²⁺ with N719.
- 3. 4 Discussion.
- 3. 5 References.

3.1 Introduction To Multivariate Calibration

In order to provide quantitative information for the target analyte, it is necessary to create a relationship between an analytical signal and the concentration of the analyte. This correlation is established by a calibration model, wherein the quantitative information for the target analyte denotes the independent variable in a linear model. The spectral characterization of compounds or analytes constitutes a wide area in analytical chemistry. This chapter is focussed on the calibration of the optical response of N719 for mercury determination by recording its UV-Visible absorbance spectra. The measured spectral absorbance fits a linear model, known as Lambert-Beer's Law. In most cases, the typical choice for spectral response calibration of a molecular probe is to observe the absorbance at a single wavelength and its changes versus analyte addition. This is known as **univariate calibration** and the model is constructed through a simple linear regression, for example, between the absorbance measured at a discrete wavelength and the corresponding concentration of the analyte. This method, however, has several limitations. In the case of univariate calibration, the model can only provide accurate results where no contributions from other sources are present. Hence, only the analyte of interest should contribute to the measured signal¹.

In a typical absorption spectrum there is a multiple number of registered wavelengths, for example in our case, N719, between $\lambda=400$ and $\lambda=800$ we can record the changes in absorption every nanometer, which implicates 400 measurements points that can be used for a better analytical characterization. The **multivariate calibration** takes into account all the spectral variables providing a good behaviour of the chemical system, which can lead to several advantages, for example, a signal-to-noise ratio reduction due to the redundant information involved in the calibration process. Another benefit is that the model can perform an excellent quantification even though the presence of other chemical or physical variables that could possibly interfere the measure. Therefore, in the design of the chemical receptor it is not necessary to pay attention primarily on selectivity, as this can be accomplished by mathematical processing by multivariate calibration. Since the spectral absorbance of a receptor provides slightly different patterns when it is exposed to various substances, observing the whole spectra it is possible to quantify more than one analyte. Additionally, a set of measurements must be selected as representative of the samples containing the species of interest. Consequently, the multivariate calibration can build a model that compensates for the interfering species, but anything causing a response at the measured wavelength must be known and included in the model. To build the model, a set of representative mixtures measurements (calibration set) are needed wherein the analyte concentration vary independently in known concentrations.

There is a number of calibration techniques that can build a multivariate model or some processing technique to distinguish species. Nowadays, it has become popular the use of an approximation called multivariate linear regression model, particularly partial least squares (PLS), principal components regression (PCR) and ridge regression (RR). Other multivariate methods can be found in the literature, although these methods are employed to a lesser extent, and many of them are based on statistical modelling: feed-forward neural network, neural networks with robust backpropagation algorithm², adaptative neuro-fuzzy inference systems (ANFIS)³, bayessian classifiers, etc.

In this way, Dieterle et al. presented⁴ an algorithm for growing neural networks which strength was to resolve mixtures of two refrigerants provided by a plasmon resonance device. An approach to multivariate calibration and instrumental drift correction employing a Kalman filter was presented by Andrew and co-workers⁵. The Kalman filter is a recursive technique used in dynamic systems, for example in target tracking applications (predictions of position and velocity of an object), in which the filter coefficients are updated using an stochastic model. In this fashion, Kalman filter was used for the determination of metal mixtures in solution. The results concluded that the Kalman model cannot match the performance of the PLS when significant physical or chemical interference effects are present.

3.1.1 Partial least squares

Multivariate calibration methods using linear regression models come with the initial assumption that there is a linear relationship between the spectral observations and some of the characteristics to be predicted. Basically the linear regression methods establish a model as a linear polynomial:

$$y = b_0 + b_1x_1 + b_2x_2 + \dots + b_nx_n + e \quad (3.1)$$

wherein b_0 is an offset, b_n are regression coefficients, x_n denotes the response measured at n wavelength and e is a residual and y is the predicted variable. A more compact equation is represented by

$$\mathbf{y} = \mathbf{X}\mathbf{b} + \mathbf{e} \quad (3.2)$$

\mathbf{y} being a column vector of $i=1, \dots, N$ measured responses of the calibration set. \mathbf{X} has dimensions $m \times (n+1)$ for m measures at n wavelengths and the size of \mathbf{b} is $(m+1) \times 1$. In order to obtain the regression vector \mathbf{b} it is necessary that the inverse $(\mathbf{X}^t\mathbf{X})^{-1}$ exists, thus the determinant of $(\mathbf{X}^t\mathbf{X})$ must not be zero. This includes the following constraint: the number of measures must be equal or higher than the number of wavelengths involved in the calibration set. In contrast to this, in biased methods such as partial least squares (PLS), principal component regression (PCR), ridge regression (RR), etc., this requirement is not strictly applicable⁶.

Partial least squares has become one of the most widely used methods for spectral analysis. The PLS performs a linear regression when the response matrix \mathbf{X} is decomposed in a similar manner to principal component analysis, generating a matrix of scores and PLS factors or latent variables. The goal of PLS is to model the relationship between the scores of the \mathbf{X} data to the scores of the \mathbf{Y} data. This can be interpreted as a projection in a new coordinate system with lower dimensions than the original space of independent variables. The PLS factors are determined by the maximum variance of the independent variables that are relevant for predicting the dependent variable(s). There are various algorithms for PLS. The most common are SIMPLS and NIPALS algorithms. The second is more intuitive and the mathematical approach can be represented according to

$$\mathbf{X} = \mathbf{TP}' + \mathbf{E} \quad (3.3)$$

$$\mathbf{Y} = \mathbf{UQ}' + \mathbf{F} \quad (3.4)$$

with \mathbf{E} and \mathbf{F} as residual matrices, \mathbf{T} and \mathbf{U} as scores matrixes, and \mathbf{P}' and \mathbf{Q}' as loading or factor matrixes. The goal of PLS is to model all the constituents in order to produce the residuals near to zero. A set of vectors known as weights \mathbf{W} , is constructed and establishes a relationship between the scores of the \mathbf{X} block and the scores of the \mathbf{Y} block:

$$\mathbf{U} = \mathbf{TW} \quad (3.5)$$

The latent vectors are calculated for both blocks independently, but an only weak relation exists between them. The inner relationship is improved by exchanging the scores, \mathbf{T} and \mathbf{U} , in an iterative calculation. The addition of weights in PLS is required to maintain orthogonal scores. Usually the column of \mathbf{Y} with the greatest variation is chosen.

Once the complete model is calculated, the resulted combined matrix of regression vectors is

$$\hat{\mathbf{B}} = \mathbf{P}(\mathbf{P}^t\mathbf{P})^{-1}\mathbf{W}\mathbf{Q}^t \quad (3.6)$$

$$\mathbf{Y} = \mathbf{X}\hat{\mathbf{B}} \quad (3.7)$$

SIMPLS gives exactly the same result as NIPALS when univariate y prediction is taken into account, but a slightly different solution for multivariate \mathbf{Y} . The explicit objective of SIMPLS is to maximize covariance. Moreover, SIMPLS is faster and slightly better results can be obtained because this method is based in a covariance criterion, whereas NIPALS is not. More details of SIMPLS and NIPALS algorithms can be encountered in a paper by Jong and co-workers⁷ and the PLS Toolbox 4.0 Manual⁸ respectively.

Another aspect is that the model of equation (2) can be expressed to include other target analytes. In this case, the model expands to

$$\mathbf{Y} = \mathbf{X}\mathbf{B} + \mathbf{E} \quad (3.8)$$

where \mathbf{Y} is an $m \times a$ for a analytes and \mathbf{B} has a column of regression coefficients for each analyte. In this situation a wavelength selection corresponding to the most representative variables for each target analyte is recommended.

Usually, the estimated parameters for calibration models are chosen following error criteria. There are three expressions for determining the level of prediction error for a model: (1) the root mean square error of calibration (RMSEC), (2) the root mean square error of prediction (RMSEP), also known as RMSEV for validation, and (3) the root mean square error of cross-validation (RMSECV). The RMSEC corresponds to the agreement between the response of the calibration model (\hat{y}_i) and the true values for the calibration samples (y_i) used to obtain the model. The equation is

$$RMSEC = \left[\frac{1}{m - n - 1} \sum_{i=1}^m (y_i - \hat{y}_i)^2 \right]^{1/2} \quad (3.9)$$

The results of RMSEC are very optimistic because the noise involved in the standards is normally modelled by the estimated parameters. To obtain the RMSEP, the validation samples are prepared and measured independently from the calibration set. It is recommended that the samples (p) reflect all sources of variability in the calibration method. The RMSEP is calculated by

$$RMSEP = \left[\frac{1}{P} \sum_{i=1}^P (y_i - \hat{y}_i)^2 \right]^{1/2} \quad (3.10)$$

The cross-validation method is the most known criteria for evaluating the number of latent variables to be used. There are several methods to obtain this estimation. The most common one is performed by estimating n calibration models and leaving a calibration sample out in each model. The left out sample is taken as an independent validation sample and is useful to obtain the prediction ability of each y_i value, \hat{y}_i , where the notation indicates that the i th sample was left out during model estimation. A similar way to perform the cross-validation based on the same procedure, but splitting the data into different groups of approximately the same size and a group is left out on each cycle to serve as an independent validation sample set. This process is repeated until all of the calibration samples have been left out. The RMSECV can be also estimated by the equation 3.10.

3.2 Enhancement Techniques For Multivariate Linear Regression

There are many undesirable variations that can disturb the multivariate calibration procedure. Usually, the first step is to pre-process the data before running the calibration modelling. Typically, digital filters can be

applied to reduce the noise, baseline and other effects maybe caused by the measurement or electronics. Some examples of the most common digital filters for de-noising spectral signals are based on *finite impulse response (FIR)*, *infinite impulse response (IIR)* and polynomial moving-average (Savitsky-Golay) filters. But often non-related information in the analytical signal appears, causing variance, which in the worst cases can be greater than the desired signal. In this case, the application of general filters is far from solving this problem. Furthermore, it is known that the multivariate linear regression is a good approximation when the model to fit is linear. The nonlinearities may be of widely different nature and they can distort the results of the model predicted by a linear regression. Linear models fail if all independent variables show similar nonlinear relationships with the dependent variables, or if variables show interactions often observed in mixtures of analytes. The strong nonlinearity is difficult to overcome and some errors in the experimental design can easily introduce nonlinearities in the model⁹. There are several methods that try to overcome the nonlinearities. Some of them take into account the experimental design. The basis of these methods consists in a screening design aimed to find out the conditions in which the signal delivers as much information as possible with a minimal experimental effort. This way appoints to an optimized model from a point of view of the proper calibration set. These techniques are mainly based on response-surface modelling and are generally divided into three areas: the design of experiments, model fitting and process optimization.

Accordingly, Real and co-workers¹⁰ employed *d-optimal* design for an exchange algorithm of samples in order to select those experiments that can provide better results. Thus, the performance of the PLS is improved even when the interference ions are present in mixtures for chromium determination.

Sometimes, a theoretical model can be extracted from the assay in a deterministic way, and thus, a linear relationship could be achieved by applying a mathematical transformation. For example, the spectral absorbance is a representation of the transmittance, which is nonlinear by definition. It can be referred as a local transformation when each variable is transformed without looking at its neighbours. For example, when the transformation is applied over independent and dependent variables by taking powers, logarithms, etc... On the other hand, a global transformation makes use all variables at ones, such as Fourier or Wavelet transformation. Many of the popular regression algorithms are very sensitive to those samples deviated from the model suggested by the major part of the data. Such observations are called *outliers* and can be caused by some errors made in the measures and consequently they do not fit the model well. To overcome this problem, outlier identification is necessary, so that none representative measures can be removed from the calibration data set in order to maintain a good performance of the model. Many techniques for the outlier detection apply the classical method to construct the model followed by the computation of several diagnostics that are based on the resulting residuals. Most diagnostics are based on

distance criteria of the samples projected over the subspace of principal components¹¹. On the other hand, robust methods are obtained by using a robust covariance matrix and a robust regression method, both highly susceptible to outliers. Moeller et al. described an overview of robust methods for multivariate analysis that can be interesting especially for chemometric tools based on PCA and PLS¹². Similarly, the regression model can be updated by a sample-weighted procedure, in order to take into account new sources of variances introduced by those outlying samples. Several methods have been developed to select the most relevant new incoming samples, wherein the most different samples from the initial calibration set are selected for an efficient updating of the model. Thereafter, the new samples are weighted when they are incorporated into the calibration set¹³. Furthermore, advanced optimization algorithms are applied to search for the best sample weights¹⁴.

Another way to minimize the nonlinearities is to extend linear models to overcome the nonlinearities. One example is quadratic PLS (QPLS), wherein a quadratic term for the inner relation is used instead of a linear term. The implicit nonlinear PLS (INLR) adds squared terms and interaction terms to the input variables and tries to account for nonlinear relationships. A comparison of several techniques for the multivariate calibration of nonlinear sensors is presented by Dieterle¹⁵, wherein the performance of the QPLS and INLR are compared with other linearization procedures and neural networks. Finally, Dieterle remarked

QPLS as the best choice when the needs are focused on speed and easy usage. On the other hand, neural networks showed better performance for the nonlinearities, but with a higher complexity and computational time.

Hence, in the present work, we provide a comparison between several pre-treatment techniques with the aim to improve the prediction ability of the method taking into account the presence of interferential effects. The methods that we have selected intend to solve the problem from different points of view, in particular: signal compression, signal correction and variable selection. Figure 3.1 represent the most used techniques for enhancing the performance of the linear regression model. The next sections explain briefly the methods used in this work for this purpose such as wavelet, orthogonal signal correction, genetic algorithm and statistical feature selection.

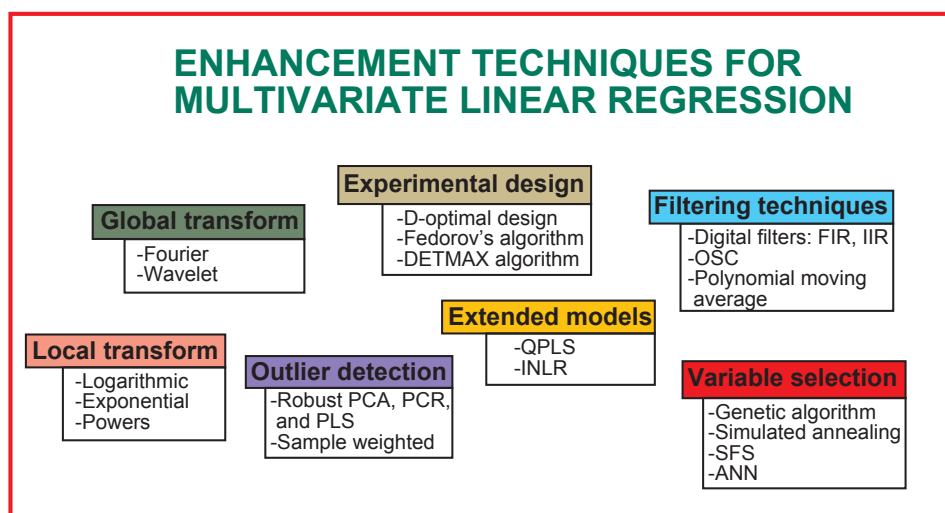


Figure 3.1. Some pre-treatment techniques that may improve the prediction ability of the linear regression model.

3.2.1. Wavelet compression

An advantage of the compression is to reduce the amount of original data by preserving the most relevant information and maintaining a good signal-to-noise ratio. In the present work, signal compression is carried out by discrete wavelets. A wavelet is a mathematical function which can be scaled and translated in order to match a specific signal, and thus, the compression is given by this mathematical approximation. The goal of the discrete wavelet transform is to take the initial data sequence, which represents a chosen length of the discrete input signal $f(x)$, and convert it into a new sequence of real numbers $CW(x)$. These numbers define the vertical size of the wavelets at each of the set horizontal scales and positions in such a way that the addition of all the wavelets taken together faithfully reproduces the original signal. The shapes of the components corresponding to the decomposed signal depend on the shape of the analysing wavelet.

Figure 3.2 illustrates an example of wavelet decomposition wherein *scales* describes frequency components of analytical signal such as an absorbance spectrum. There are a variety of families that can be used depending on the nature of the analytical signal. A narrow wavelet is used for detecting sharp features and a wider wavelet is useful for uncovering general signal properties. In this work, three orthogonal wavelet functions: Daubechies-4, Coiflet-4 and Symlet-8 were selected due to their good properties regarding the compression of smooth signals¹⁶ (see

their forms in Figure 3.3). Wavelet analysis has previously been employed in NIR applications^{17, 18}, and denotes a good compression ratio while preserving the data variance.

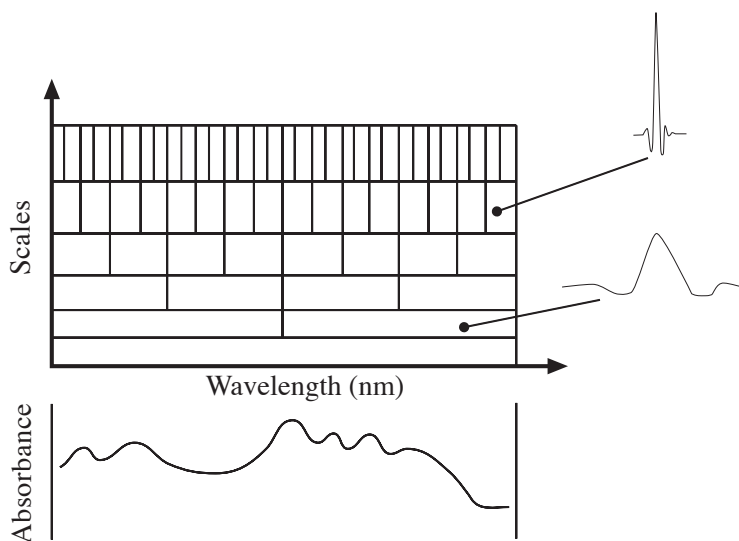


Figure 3.2. Representation of wavelet transformation.

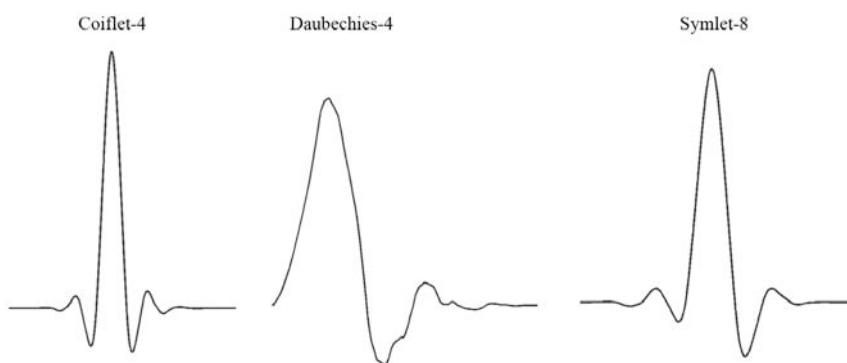


Figure 3.3. Wavelet *mother* functions employed for spectral analysis.

3.2.2 Orthogonal signal correction

The orthogonal signal correction (OSC) and its application in spectroscopic analysis¹⁹ attempts to remove those parts of the spectral range that are not related to the quantification process. This can be accomplished by removing the bilinear components from \mathbf{X} without affecting relevant information. Moreover, this fact matches with our assumption of that the interferential metals present in the aqueous matrixes will cause non-related effects in the mercury-N719 complexation and hence, some co-linearity can be removed. For this purpose, a related PCA/PLS solution is proposed. According to this solution, the weight vector (\mathbf{w}) is modified targeting $\mathbf{t} = \mathbf{X}\mathbf{w}$ orthogonal to \mathbf{Y} , instead of searching the maximum covariance. In a first step the optimal linear relationship of \mathbf{X} is obtained by representing its first principal component in a vector \mathbf{t} . Subsequently, \mathbf{t} is forced to be orthogonal to \mathbf{Y} by algebraic manipulation. The process is repeated until the calculated weights (\mathbf{w}) are as close as possible to the orthogonal expression of the scores (\mathbf{t}^*). After convergence, a loading vector \mathbf{p} is computed, and then the filtered signal is calculated by removing $\mathbf{t}^*\mathbf{p}'$ from \mathbf{X} . The resulted filtered signal is used as input in the calculus of the next 'OSC component'. The final filtered matrix and \mathbf{Y} are used in a PLS regression in order to obtain the calibration model. More details in the OSC algorithm can be found in Wold's paper¹⁹. If the number of variables is larger than the number of training samples it is always

possible to find a solution otherwise is not always possible. Moreover, a unique solution is not guaranteed, but rather there are infinite solutions. This is a drawback of the OSC that needs to be improved. Since the scaling of the original X-data influences the result of the OSC, the use of non-scaled data seems to be more appropriate for an OSC application. However, a *mean centering* of the calibration data is recommended before the signal correction for the proper performance of the internal PLS in OSC function. Some examples of application of OSC can be found in NIR spectra analysis; for example, a model from corrected spectra has been improved for the discrimination between coffee varieties²⁰. Moreover, the OSC has been combined with wavelet and their rolls in compressing and filtering data have been explored. Some precedents of this implementation were described in Erikson²¹ and Esteban-Díez²² papers.

3.2.4. Variable Selection

Although PLS was considered for many years to be almost insensitive to noise, it has been shown in the last years that a feature selection can be highly beneficial, since the predictive ability of the model improves while its complexity decreases. Consequently, an approach to improve the performance of the linear regression models is based on a variable selection, wherein the variables responsible of the maximum information are selected in front of those more affected by noise or nonlinearities. The purpose of the variable selection techniques is to find a subset of

variables that is reasonably linear with the phenomenon to model and to discard the variables that are more affected for the noise or nonlinearities. This can be considered as a previous treatment before applying a linear regression modelling. Once the proper calibration subset has been selected, a model calibration such as PLS or PCA can be performed. By selecting the most informative variables with maximum signal to noise ratio, the goodness of model prediction can considerably increase. Another benefit of the variable selection is the compression of the amount of data by reducing the number of variables, and thus, the complexity of the model is minimized.

Most variable selection approaches are based on minimizing a prediction-error criterion. The variables are successively added or removed depending on the algorithm and they will form part of the final subset if some criteria are accomplished. For example, the RMSEP or RMSECV is used as a criterion for evaluating selected variables and choosing the final model. The main drawback of these methods is that a suboptimal subset can be chosen and the result can easily converge to a locally optimal combination of variables, which does not spot on the global subset. There are many examples that apply a variable selection to carry out the quantification task. For example, a hierarchical Bayes formulation was proposed in order to provide a new way to achieve a tuning variable selection process, according to which, the probabilities model provides a global solution efficiently²³. The method assigned priorities for each candidate model and parameters associated to the models. Thereafter, a

bayesian formulation was used to resolve the analytical approximation for all candidate models. Another inferential procedure²⁴, also based in bayesian variable selection, provided a selection of discriminating variables, by estimating the number of clusters and sample allocations, and performing a class prediction for future observations. Furthermore, a Fuzzy method was proposed to identify the set of the most important wavelengths for a chemical component of interest²⁵.

Other studies remark that if one wavelength contains useful information for quantitative analysis, it is very likely that wavelengths in its neighbourhood also contain such information. Therefore, selecting spectral intervals rather than only selecting very few separate wavelengths could provide more stable and reliable models. Accordingly, an advanced interval PLS model presented by Norgaard et al²⁶ consisted in a graphical oriented procedure for interval selection and its repercussion on the model prediction. Recently, Lu Xu and co-workers have introduced an improvement to prevent the model from losing useful information and overfitting²⁷. The proposal is based on a machine learning method where the model is constructed by the linear combination of interval PLS models. The spectral intervals are selected automatically by combining the cross validations of the sub-models. Monte Carlo cross validation is used to validate the interval models and stacked regression is applied to find the combination coefficients that minimize RMSECV.

Neural networks have also been applied for the variable selection procedure, in which their variable structure makes possible their adaptation to solve several problems. For example, the information generated using these methods may serve to interpret the influence of the selection carried out in the experiment under study, in those cases wherein the nature of the relationship is not known and susceptible to non-linearity. Following that, a further study of variable influence and selection using neural networks was reported by Andersson²⁸.

3.2.5 Genetic algorithms

Various approaches have been used to define a variable selection with the goal of performing the quantification task in spectral analysis. Among them, the most known methods are based on a stochastic search such as *genetic algorithms* (GA) and also *simulated annealing*²⁹. These algorithms have been applied to extremely complex problems in several areas. Herein, this brief introduction focuses on genetic algorithm and the basis of its adaptation to resolve the variable selection technique is exposed, more precisely its application in the spectral wavelength selection. The fundamentals of genetic algorithm are inspired by the theory of the evolution, according to which the best individuals have a greater chance to survive and a greater probability to extend their genomes by reproduction. Two winner individuals cause the mixing of their genomes, which may result in a better progeny.

There are different versions of genetic algorithms that perform well on spectral analysis. All these versions have in common the fact that a chromosome can be subdivided into genes or bit-fields, each one encoding the value of a different variable (wavelength). Some divergence of the algorithm can be specially found in the reproduction step, which consists in duplicating the chosen chromosomes on the basis of a probabilistic approach. In the selection procedure, the parent generation and descendant chromosomes are selected depending on a probabilistic criterion. Further approaches propose methods for exchanging the genes between chromosomes towards redundancy elimination. GA must balance the number of variables to consider and the number of test objects, meanwhile, if the number of tested objects increases the resulted model has more probabilities to be *over-fitted*, which it means that the model will generate bad results for new incoming events (measurements). In the present work, the method introduced by Leardi has been selected³⁰. In this approach, the reduction of the over-fitting risk prevails. Leardi considers that the final model approaches a global solution taking into account the results of 100 short independent runs. The process learns from the previous runs due to the fact that the frequency of variable selection modifies a probability vector associated with the chromosomes. Therefore, it is possible, according to this approach, to concentrate efforts mainly on the most correlated spectral regions, without discarding the possibility of a global exploration. For this reason, the data is separated into p groups, forming each one a

training set wherein the genetic algorithm described in Figure 3.4 is performed. Thus, the genetic algorithm itself is run p times, and the subset of variables found are validated by the prediction of its associated model.

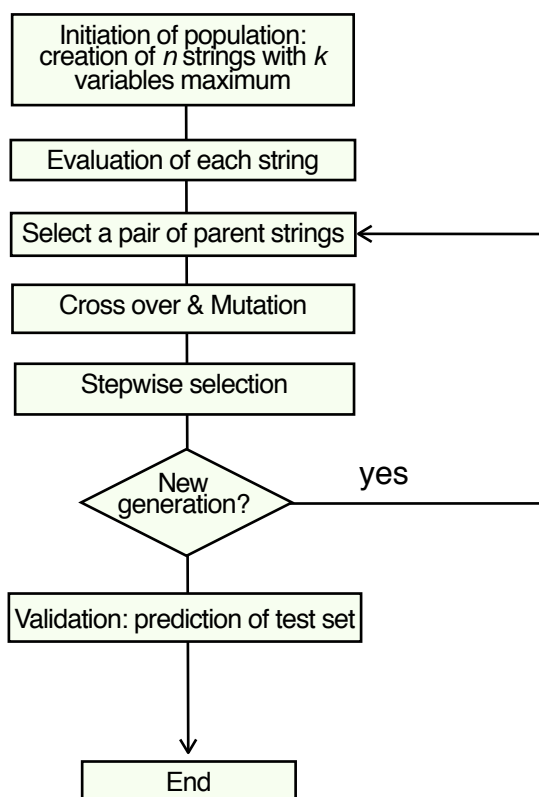


Figure 3.4. Flow diagram of genetic algorithm.

3.2.6 Statistical feature selection (SFS)

If the calibration process can be understood as a statistic process, it is conceivable that a pure statistic pre-treatment that correlate better with the observable fact will yield better results. Consequently, the statistics

may provide additional information making feasible an estimation of the error sources, the goodness of the experimental data set and outlier detection. Herein, the proposal is based on the method proposed by E. Llobet et al.³¹ for the removal of non-informative and noisy features mass spectrometry for electronic nose applications. This method, named *statistical feature selection (SFS)* can be adapted for absorbance spectral analysis with a high efficiency at a very low computational cost, even when a large number of wavelengths are present in the data set. Basically, the method is based on a discrimination rate applied over the variables (wavelengths), the less correlated variables being penalised in such a way that they cannot take part in the calibration set. As a previous step, the calibration samples are classified into categories (for example each category corresponds to an analyte concentration level). The criterion is based on a variance ratio called discrimination function (DF) that is obtained from the intra-category and inter-category variances for each wavelength of the spectra. The intra-category variance σ_{tra}^2 is defined as

$$\sigma_{tra,jk}^2 = \frac{\sum_{i=1}^{n_k} (Ab_{ji} - \mu_{jk})^2}{n_k - 1} \quad (3.11)$$

where Ab is the absorbance spectra of the k measures, n_k is the total measures within the category, j represents the wavelength variable and μ_{jk} is the mean of each variable j over the n_k measures.

The overall intra-category variance considering d categories is defined as:

$$\sigma_{overtra,j}^2 = \frac{\sum_{k=1}^d n_k \sigma_{tra,jk}^2}{\sum_{k=1}^d n_k} \quad (3.12)$$

Consequently, the inter-category variance is expressed as:

$$\sigma_{ter,j}^2 = \frac{\sum_{i=1}^d (\mu_{jk} - \bar{\mu}_j)^2}{d - 1} \quad (3.13)$$

where $\bar{\mu}_j$ is the mean value over the μ_{jk} .

The discrimination factor over the spectral range is defined as follows:

$$DF_j = \frac{\sigma_{ter,j}^2}{\sigma_{overtra,j}^2} \quad (3.14)$$

As expected, the result is a wavelength selection of the variables with a major correlated variance in front of those variables more influenced by noise or other type of interference. A fine adjustment of the discrimination factor can modify the number of the wavelengths selected

from different regions of the spectra and a comparison between several DF factors and PLS performance is recommended.

Up to this point, the statistical procedure explained above can be understood as a univariate pre-treatment. Consequently, one should evaluate the risk of eliminating those synergetic variables that have low discrimination ability if considered individually. The method proposed to prevent this problem is based on the same statistical rules depicted above but considering all pair combinations of the spectral variables. Although ternary, quaternary and further spectral combinations could be also considered, the high computational cost would make the processing unfeasible.

3.3. Selectivity Enhancement And Quantification of Hg^{2+} With N719

The ideal case in sensor design is to achieve specificity for a single analyte, but in real life this situation is rarely found. In the best cases, selective systems can be obtained which not only recognise the analyte of interest, but also other compounds. The present study tries to explore the behaviour of the **N719**[bis(2,2'-bipyridyl-4,4'-dicarboxylate)ruthenium (II) bis(tetrabutylammonium) bis(thiocyanate)] in the determination of mercury, even in presence of its potential interferences. For that purpose, the ions that interfere to a larger degree have been determined, and those

with more relevance in a real application have been considered, in other words the metal ions with a highest toxicity and more probability to be present in real samples have been evaluated. Therefore, the mercury quantification in this environment requires an especial treatment: first, the choice of the training samples and second, a calibration method with the necessary robustness to provide adequate prediction values. Obviously, this requirement needs to be solved by multivariate calibration.

Next, it will be discussed the physical and chemical interferences that can affect the chemical probe. Thereafter, the calibration samples and the calibration strategies will be configured.

3.3.1 Study of interferences

3.3.1.1 Effect of temperature and pH

A deficiency of the chemical receptor is related to its influence response under physiological interferences. First of all, the influence of pH and temperature was tested. All the experiments were carried out in aqueous/ethanol solvent mixtures. Accordingly to the pH effect observation, four stock ethanol solutions were prepared at pH 2, 4, 6 and 8. A Britton Robinson (B-Rb) buffer was used for the pH 2, 4 and 6 solutions, while the pH 8 solution was based on HEPES buffer. Moreover, N719 was added to each of the buffered stock solutions up to a final concentration of 0.1 mM. Separately, a 1 mM mercury(II) acetate solution in deionized

water was prepared. Four mercury titrations were recorded for each N719-buffer dissolution, the absorbance was measured using a double beam Shimadzu UV-2401PC spectrometer. The sensing response towards mercury ions at different pH was evaluated. A lack of response was clearly observed at pH 2, whereas for any other pH value slight variations in the entire spectrum were observed, which could influence the measurements in the calibration procedure. The experiment showed that the molecular response was enhanced in the basic range between pH 6 and pH 8 (see Figure 3.5).

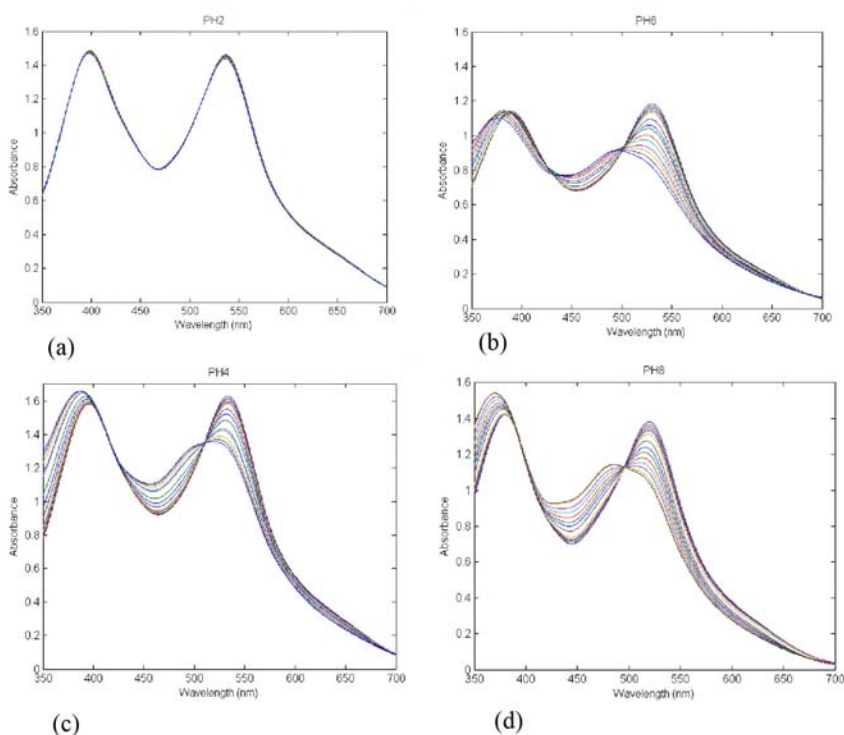


Figure 3.5. Effect of the pH over the N719 spectral response versus Hg^{2+} titration, (a) pH 2, (b) pH 4, (c) pH 6, and (d) pH 8.

Following the same procedure as described above in the context of pH influence evaluation, several mercury titrations were made in 0.1 mM N719 ethanol solutions at different temperatures, covering a range from 5 to 35°C. The results showed slight variations in the whole temperature range that are fewer than the errors introduced in the sample preparation. Therefore, we consider that the temperature effect on the measurement can be ignored. Figures 3.6 and 3.7 show the relative response of N719 respect to the molecule blank upon addition of mercury under the influence of pH and temperature respectively.

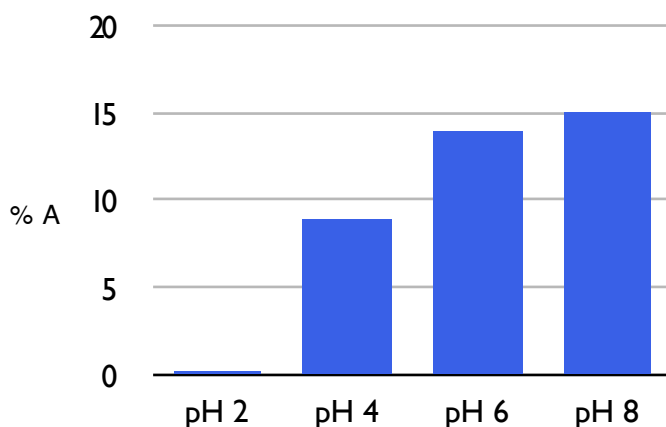


Figure 3.6. Influence of the pH and the relative absorbance response of N719 ($\lambda=520, 530$ nm) at 3.29 mg L^{-1} of Hg^{2+} concentration.

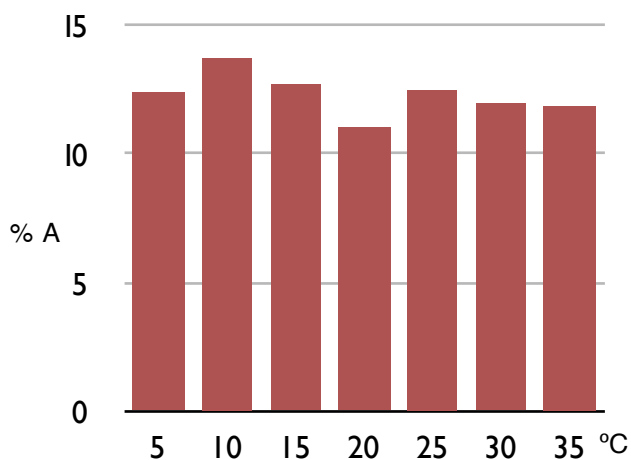


Figure 3.7. Relative absorbance response ($\lambda=530$ nm) of N719 at 2.64 mg L^{-1} of Hg^{2+} concentration in the $T= 5\text{-}35^\circ\text{C}$ range.

3.3.1.2 Other metal ions

The color change of the bis-thiocyanate ruthenium(II) complexes is specific for Hg^{2+} . Previous work³² about the selectivity of N719/ TiO_2 films remarked that none appreciable optical changes were observable at *naked eye* from different anions and metal ions, especially those catalogued by the Environmental Protection Agency as *drinking water contaminants*. Herein, we focused in a more detailed study of N719 in solution with other ions that can possibility form a complex with NCS groups. Therefore, in order to determine the most interfering metal ions for the ruthenium complex probe, a stock solution of 0.1 mM N719 in ethanol was prepared. Thereafter, the relative response of the dye to different metal ions was observed by adding 5.5 mg L^{-1} of each metal ion

to separate samples. Thus, the spectral absorbance of the N719 samples was recorded in the presence of Hg^{+2} , Ni^{+2} , Cd^{+2} , Pb^{+2} , Sn^{+2} , Co^{+2} , Mn^{+2} , Cu^{+2} and Zn^{+2} .

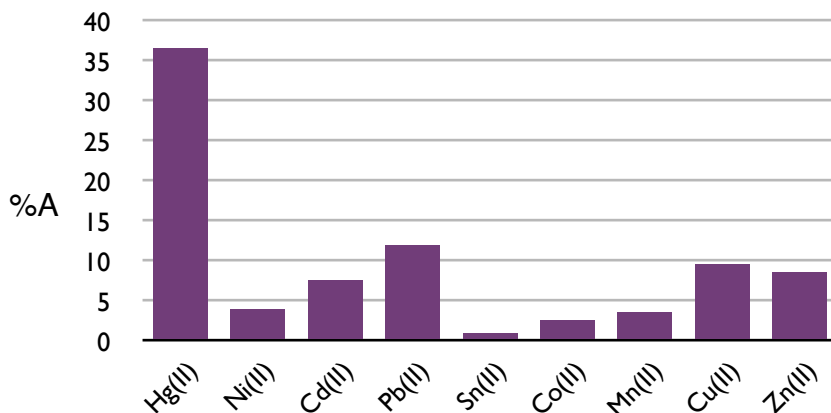


Figure 3.8. Relative absorbance response (%) of N719 ($\lambda=520, 530$ nm) for several ions at 5.5 mg L^{-1} of each one.

Figure 3.8 shows the relative response with respect to the N719 blank for each metal ion. A remarkable specific response to mercury is observed if compared to the rest of metal ions. Finally, the ions that lead to changes in the response above five per cent relative to the N719 blank have been selected as potential interferences. Consequently, the metals that will be considered in the calibration procedure are: cadmium, lead, copper and zinc.

3.3.2 Data sets

3.3.2.1 Calibration and training data sets

Ten titrations of mercury covering a range between 0 and 3.31 mg L⁻¹ and registered at intervals of five minutes constituted the calibration data set. Moreover, additional mercury titrations were performed for four different settings, classified according to the overall concentration of the interfering metal ions: no presence, low concentration, medium concentration and high concentration.

A stock solution of the target molecule N719 (84 μM) buffered to pH 7 in a ethanol HEPES (10 mM) solution was prepared. The interferential metal ions were dissolved separately in pure water to end concentrations of 1 mM. A mercury stock solution (5 mM) in 100 mL of pure water was prepared, and four aliquots (3 mL) were taken from the initial stock solution (N719) and mixed in a quartz cuvette with varying amounts of interferential metals. Afterwards, the corresponding mercury titrations were performed, taking into account 4 repetitions for each set (see Table 3-I). The spectral absorbences were recorded in a Shimadzu 1700 spectrometer, at intervals of 0.5 nm throughout the spectral range $\lambda=350-625$ nm. The whole data set consisted of 44x4, i.e. 176 measurements, in which 128 were employed for the model construction (calibration data set). On the other hand, the adjustment of the pre-treatment methods was performed with 12 measurements, which had not

been previously considered for the construction of the calibration model. Each one of these values, hereinafter referred to as training data, is the average value of four repeated measurements.

TABLE 3-I. Calibration data set.

None interference level		Low interference level	
Hg ²⁺ (mg L ⁻¹)	Cd ²⁺ , Pb ²⁺ , Cu ²⁺ , Zn ²⁺ (mg L ⁻¹)	Hg ²⁺ (mg L ⁻¹)	Cd ²⁺ , Pb ²⁺ , Cu ²⁺ , Zn ²⁺ (mg L ⁻¹)
0	--	0	0.13,0.13,0.27,0.27
0.13	--	0.13	0.13,0.13,0.27,0.27
0.33 ^a	--	0.33 ^a	0.13,0.13,0.27,0.27
0.49	--	0.49	0.13,0.13,0.27,0.27
0.66 ^a	--	0.66 ^a	0.13,0.13,0.27,0.27
0.99	--	0.99	0.13,0.13,0.27,0.27
1.49	--	1.49	0.13,0.13,0.27,0.27
1.98 ^a	--	1.98 ^a	0.13,0.13,0.27,0.27
2.48	--	2.48	0.13,0.13,0.27,0.27
2.98	--	2.98	0.13,0.13,0.27,0.27
3.31	--	3.31	0.13,0.13,0.27,0.27
Medium interference level		High interference level	
Hg ²⁺ (mg L ⁻¹)	Cd ²⁺ , Pb ²⁺ , Cu ²⁺ , Zn ²⁺ (mg L ⁻¹)	Hg ²⁺ (mg L ⁻¹)	Cd ²⁺ , Pb ²⁺ , Cu ²⁺ , Zn ²⁺ (mg L ⁻¹)
0	1.35,1.35,2.7,2.7	0	5.62,5.52,5.51,5.7
0.13	1.35,1.35,2.7,2.7	0.13	5.62,5.52,5.51,5.7
0.33 ^a	1.35,1.35,2.7,2.7	0.33 ^a	5.62,5.52, 5.51,5.7
0.49	1.35,1.35,2.7,2.7	0.49	5.62,5.52, 5.51,5.7
0.66 ^a	1.35,1.35,2.7,2.7	0.66 ^a	5.62,5.52, 5.51,5.7
0.99	1.35,1.35,2.7,2.7	0.99	5.62,5.52, 5.51,5.7
1.49	1.35,1.35,2.7,2.7	1.49	5.62,5.52, 5.51,5.7
1.98 ^a	1.35,1.35,2.7,2.7	1.98 ^a	5.62,5.52, 5.51,5.7
2.48	1.35,1.35,2.7,2.7	2.48	5.62,5.52, 5.51,5.7
2.98	1.35,1.35,2.7,2.7	2.98	5.62,5.52, 5.51,5.7
3.31	1.35,1.35,2.7,2.7	3.31	5.62,5.52, 5.51,5.7

^aMeasurements used in the training data set.

3.3.2.2 Validation data set

The goodness of the model prediction should be checked with measurements that have not been considered for model building. To this regard, new titrations of N719 from the previous stock were implemented and constituted an independent test set. The new set of titrations was obtained by adding stepwise incremental quantities of mercury to samples containing different concentrations of interferential metals (see Table 3-II). In order to check the general ability of the model, the concentrations of foreign metal ions must differ from the calibration data, provided that all of these values are in the concentration range of the measurements used for model building.

TABLE 3-II. Validation data set.

SET 1		SET 2	
Hg ²⁺ (mg L ⁻¹)	Cd ²⁺ , Pb ²⁺ , Cu ²⁺ , Zn ²⁺ (mg L ⁻¹)	Hg ²⁺ (mg L ⁻¹)	Cd ²⁺ , Pb ²⁺ , Cu ²⁺ , Zn ²⁺ (mg L ⁻¹)
0	--	0	0.59, 0.62, 1.35, 1.33
0.26	--	0.13	0.59, 0.62, 1.35, 1.33
0.49	--	0.33	0.59, 0.62, 1.35, 1.33
1.16	--	0.66	0.59, 0.62, 1.35, 1.33
		1.16	0.59, 0.62, 1.35, 1.33
SET 3		SET 4	
Hg ²⁺ (mg L ⁻¹)	Cd ²⁺ , Pb ²⁺ , Cu ²⁺ , Zn ²⁺ (mg L ⁻¹)	Hg ²⁺ (mg L ⁻¹)	Cd ²⁺ , Pb ²⁺ , Cu ²⁺ , Zn ²⁺ (mg L ⁻¹)
0	1.98, --, 0.59, 0.6	0	4.87, 4.83, 4.83, 5
0.66	1.98, --, 0.59, 0.6	0.33	4.87, 4.83, 4.83, 5
1.16	1.98, --, 0.59, 0.6	1.16	4.87, 4.83, 4.83, 5
1.98	1.98, --, 0.59, 0.6	1.98	4.87, 4.83, 4.83, 5

3.3.3 Pre-processing method adjustment

All results have been obtained from algorithms programmed in scripts for MATLAB® additional toolboxes. The PLS-Toolbox 2.0.1 from EigenVectors was used for the OSC and PLS functions. The wavelet compression was programmed with the Wavelet Toolbox for MATLAB v6, and the genetic algorithm was inspired in the version developed by R. Leardi³³. Finally, the statistical feature selection was programmed entirely using standard Matlab code. All models were tested in a Pentium D (3 GHz) platform.

Since the spectral data sets comprise as many as 551 wavelengths, the adjustment of the parameters for each particular pre-processing method is likely to be complex, and thus, a decimation process was envisaged. The fact that the N719 absorbance patterns present low frequency features should allow for reducing the number of variables by decimation without a significant loss of information. When decimating, a low-pass filter for preventing aliasing components is required, which should allow for reducing the number of initial spectral data to such an extent that the best performance of the selected pre-treatment method is achieved. In the first step, the parameters of each specific pre-processing technique and the number of latent variables employed by the PLS models are fine tuned as follows. The measurements in the calibration dataset are used to build a given PLS model (i.e., one that employs a particular setting of a pre-processing technique). Then, the optimal setting is found by a cross-

validation procedure using the measurements from the training dataset (i.e., different from those used to build the PLS models). In other words, the optimal setting for a given pre-processing technique is the one that leads to the lowest root mean squared error of cross validation (RMSECV) computed on training measurements. An important aspect of building PLS models is determining the number of latent variables to be used. Selecting a low number of latent variables should maintain regression coefficients with reduced variances and hence, reduced variances for predictions of future samples. However, if the dimensionality of the model is too small, not enough information would have been included and the bias of the model may increase³⁴. Consequently, the determination of an acceptable balance of bias and variance could provide more parsimonious models. One possible solution is to plot the RMSECV against the number of latent variables and select the minimum number of variables after a sharp decrease in the RMSECV plot. Additionally, the model performance for the training set has been presented by the predicted cross-validated variance of \mathbf{Y} , expressed as

$$Q^2 = 1 - \frac{\sum (y_{pred} - y)^2}{\sum y^2} \quad (3.15)$$

where y_{pred} corresponds to predicted values of the training set and y to the respective known concentrations.

In the second step, once the optimization process had been conducted, the performance of the PLS models built was estimated in terms of root mean squared error of prediction (RMSEP). The measurements employed in this procedure are within the validation dataset. These measurements are different and independent from those employed for building the optimized PLS models. Due to the high amount of metals present in the mixtures, saturation effects may appear above 2.5 mg L⁻¹ of mercury. Therefore, model performance has been estimated employing validation data in the 0 to 2 mg L⁻¹ mercury concentration range. The RMSEP percent has been expressed accordingly

$$\%RMSEP = \frac{100}{r_m} \sqrt{\sum \frac{(y - y_{pred})^2}{N}}$$

(3.16)

where r_m represents the mercury concentrations range (0-2 mg L⁻¹) and N is the number of measurements.

In the following sub-section the results reached with the different pre-processing techniques are shown. Aspects such as the decimation factor applied, the optimal settings for each technique (i.e. those that led to best results on training data) and, finally, the performance estimated using validation data are discussed.

3.3.4 Results and discussion

3.3.4.1 PLS without pre-treatment

As starting point, the performance of the direct PLS has been observed and the parsimonious criterion explained above has been applied for the selection of the PLS factors. The test throughout the training data showed that, as the model dimensions increased, the results obtained were more likely to be over-fitted. Therefore, 3 PLS components were considered as optimum. Moreover, the performance of direct PLS calibration was compared with the whole data (551 variables) and decimated by a factor of 12 (46 variables). The coherency of root mean squares on prediction in both cases (RMSEP without decimation=10.48 and RMSEP with decimation=10.46) indicates that not noticeable effect has been introduced by decimation. Figure 3.9 shows the calibration plot corresponding to the validation data for the simple PLS. The non-linear effects introduced by the interferential metals cause a noisy response of the prediction model, especially in the validation data sets 2 and 4. Consistently, as these samples contain a higher amount of foreign metal ions, these measurements are surely out of scope of a linear regression calibration. The following section tries to broaden the scope of the PLS model by considering the non-linearities caused by the other metals through a suitable pre-processing technique.

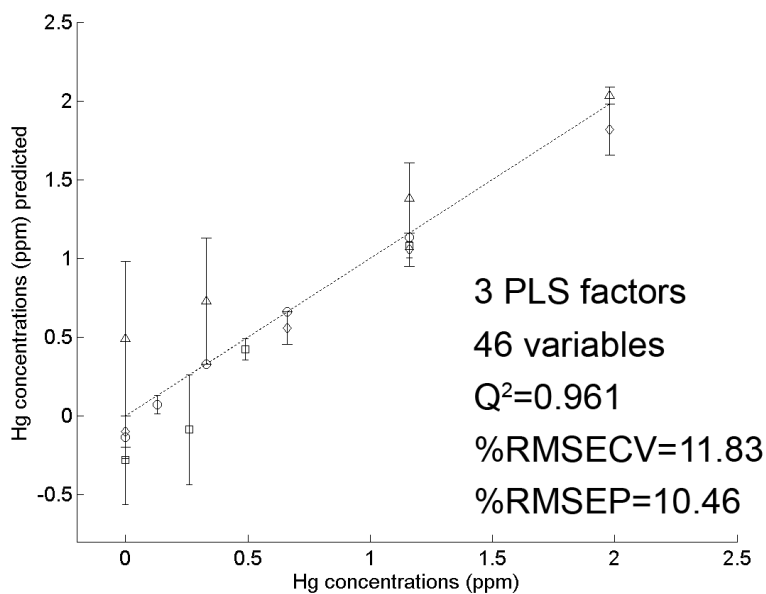


Figure 3.9. PLS with decimation. Prediction plots for validation data sets: (o) set 1, (□) set 2, (◇) set 3, (△) set 4.

3.3.4.2 PLS with wavelet compression

Apart from decimation, the wavelet-based technique can also reduce the number of X-data, and thus it can be evaluated for its suitability over the predictive ability of the PLS model. The multi-resolution analysis has been employed as wavelet transformation technique (Matlab function 'wavedec'), the wavelet coefficients representing the details of the signal at a given level. This technique is based on DWT transformation; the simplicity and computation speed of DWT probably renders this method as the most popular for spectral analysis. It is a prerequisite of DWT that

the signal should be of length 2^n . For this reason, the spectral data have been trimmed in such a way that the length is a potential of two (dyadic), yielding 512 variables. In order to determine up to which extent the trimming process could affect the PLS prediction, a PLS model was built using the trimmed data.

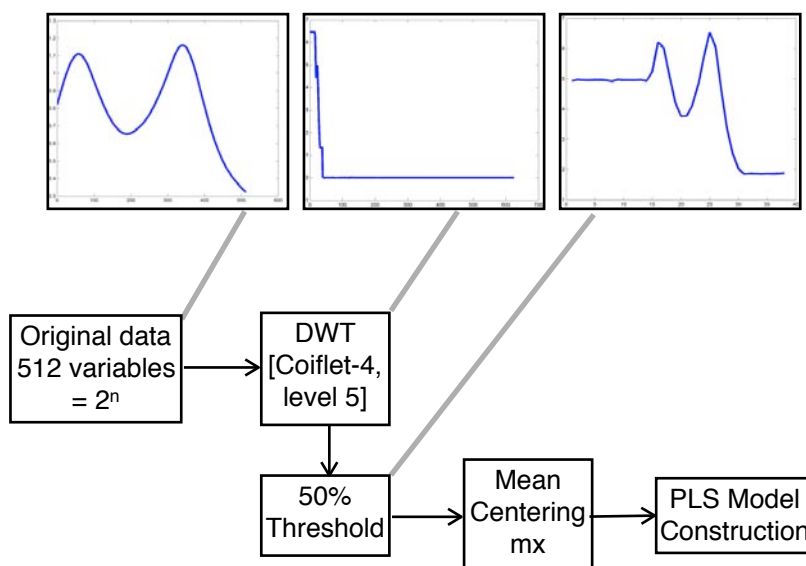


Figure 3.10. Wavelet-PLS model construction.

No significant difference in its predictive ability was found (in comparison to the model that used all variables). After wavelet decomposition, compression is achieved by removing the wavelet coefficients below 50% of the wavelet vector variance. The resulted vector is subjected to mean centering and the PLS model is constructed. Different decomposition levels and wavelet functions were tested, being

Coiflet-4 at five-level the best wavelet structure for this application. On the other hand, the adjustment of the model for the training data was optimum considering 4 PLS components. Figure 3.10 shows the procedure for the PLS wavelet pre-treatment-based, meanwhile the scheme for processing new incoming data is shown in Figure 3.11. In summary, the wavelet process offered a similar compression order than decimation, but no improvement on the PLS model predictive ability was observed (see Figure 3.12). Indeed, the high computational cost of wavelet makes the adjustment process difficult and the resulting model is highly biased both for training and validation data.

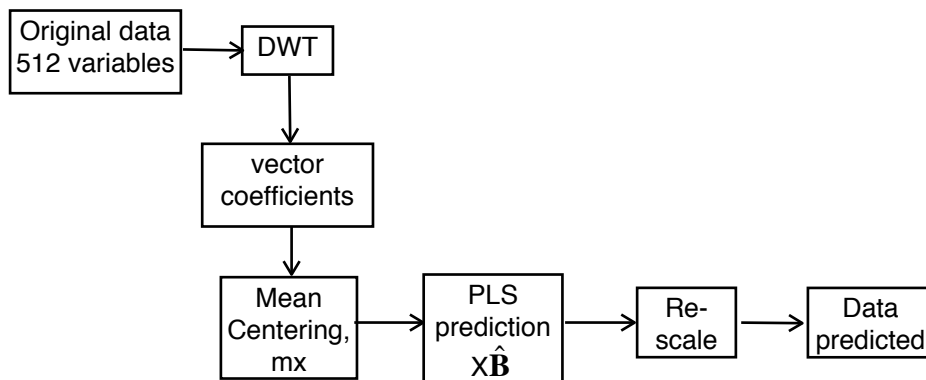


Figure 3.11. Wavelet-PLS prediction of incoming data.

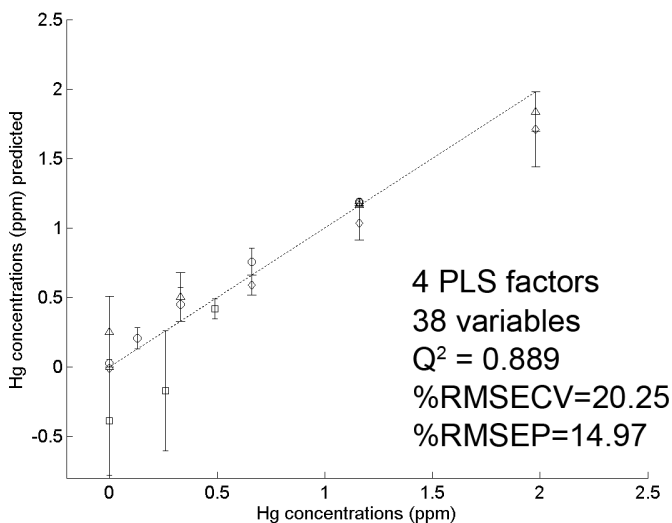


Figure 3.12. PLS with wavelet compression. Prediction plots for validation data sets: (o) set 1, (□) set 2, (◇) set 3, (△) set 4.

3.3.4.3 PLS with OSC filtering

OSC is a PLS-based solution incorporating an objective function aimed at removing the X -data variation that is unrelated to Y . The internal latent variables are similar to factors in a PLS model. The resulting processed data is obtained by subtracting from the X matrix the product of the scores orthogonal to the concentration (T) and the loading matrices (P'):

$$X_{OSC} = X - \sum_{i=1}^N T_i \cdot P'_i \quad (3.17)$$

being N the number of iterations that the treatment is applied. The steps necessary to apply an OSC-PLS model-based are shown in the schemes

of Figure 3.13 and Figure 3.14 corresponding to the OSC-PLS model construction and prediction procedure for new data. First, the data has been decimated to 46 wavelengths by applying a decimation factor of 12. After mean centering, the OSC model reached an optimum with one component and 100 iterations with a tolerance of 99.5 per cent as additional parameters. Thereafter, a further mean centering is necessary in order to obtain the PLS model.

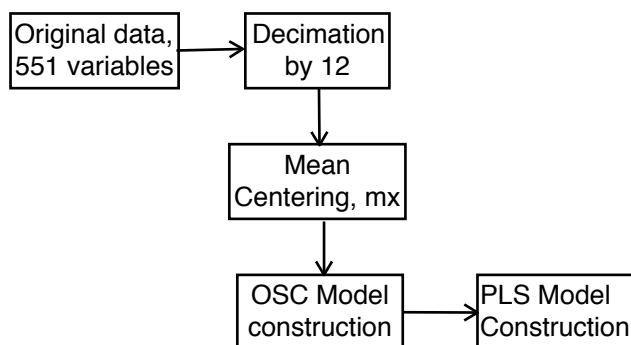


Figure 3.13. Scheme of OSC-PLS model construction.

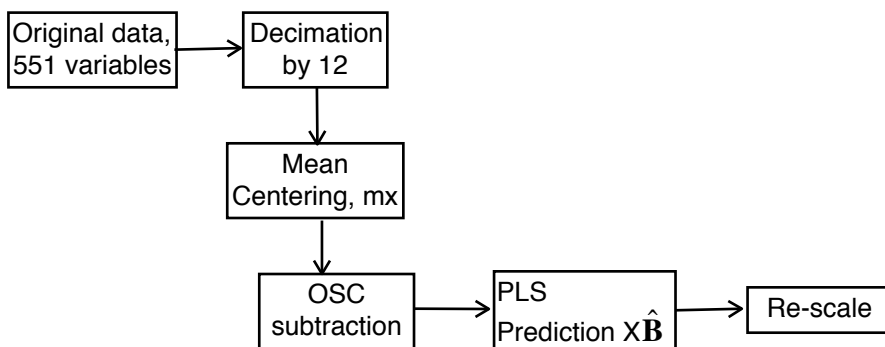


Figure 3.14. OSC-PLS prediction for new data.

The extraction procedure of factors in the RMSECV plot indicates a slight over-fitting between 4 to 7 factors, so that the low error of prediction for the training data resulted in biased models for new samples. A more parsimonious model was achieved considering 2 PLS factors. This fact corroborates that the OSC forces to concentrate larger variance in the first factors, reducing the dimensions of the model if it is compared with a direct PLS processing. However, in this case by applying the orthogonal signal correction the model performance reveals a slight over-fitting of the training data, which causes a bias on the prediction of validation data, see Figure 3.15.

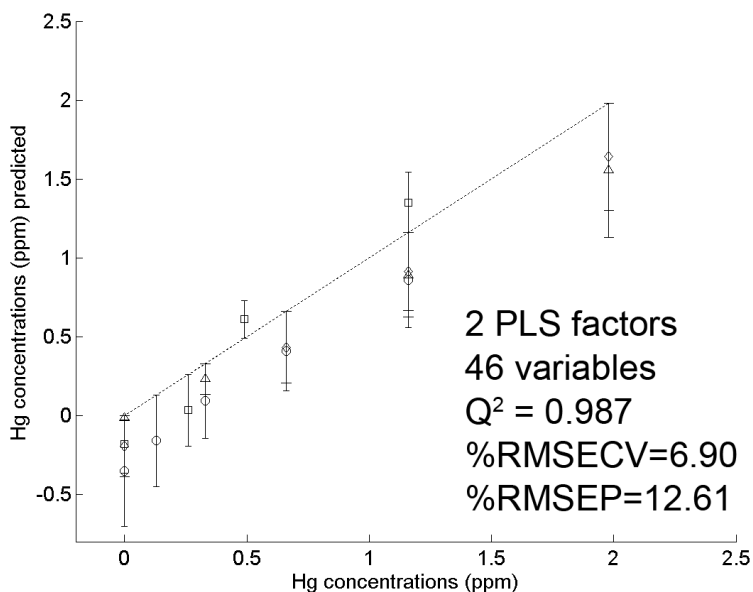


Figure 3.15. Prediction plots of the OSC-PLS model for the validation data set: (o) set 1, (\square) set 2, (\diamond) set 3, (\triangle) set 4.

In Figure 3.15b, the signal spectra of the OSC model corresponding to the validation data set is represented, wherein two spectral regions at $\lambda=350\text{-}400\text{ nm}$ and $\lambda=520\text{-}560\text{ nm}$ may be identified as highly influenced by non-correlated information. Note that the OSC signal is inverted progressively as the concentration of foreign cations increases. This interesting effect could be beneficial in order to check the presence of interferential effects in mercury measurements.

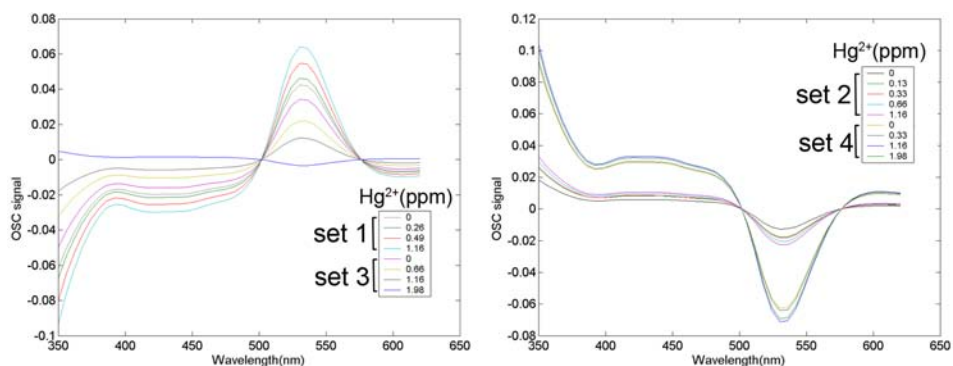


Figure 3.15b. Representation of the OSC signal for mercury titrations in the presence of interferences (left profiles, low concentrations of other metal ions; right profiles, high interferences).

3.3.4.4 PLS with wavelet + OSC filtering

As previously described, the wavelet compression followed by orthogonal signal correction was explored. Therefore, two relevant pre-processing techniques have been combined prior to the construction of the calibration model, in an attempt to improve of the resulting prediction ability by signal compression and removal of irrelevant information³⁵. In

this case, the Symlet-8 at 5 level was the optimum choice for wavelet mother function. The wavelet compression provided 38 coefficients. Afterwards, a mean centering and an orthogonal signal correction were performed. The RMSECV evaluation of the PLS model was adjusted considering two OSC factors and 3 PLS components. Less over-fitting was observed in comparison to the use of OSC only. Additionally, the RMSEP was obtained for the validation data. A considerable gap between the predictions for training data and those of validation data occurred (see Figure 3.16). This fact may result from a low consistency of the model with a high variance in the prediction of new samples.

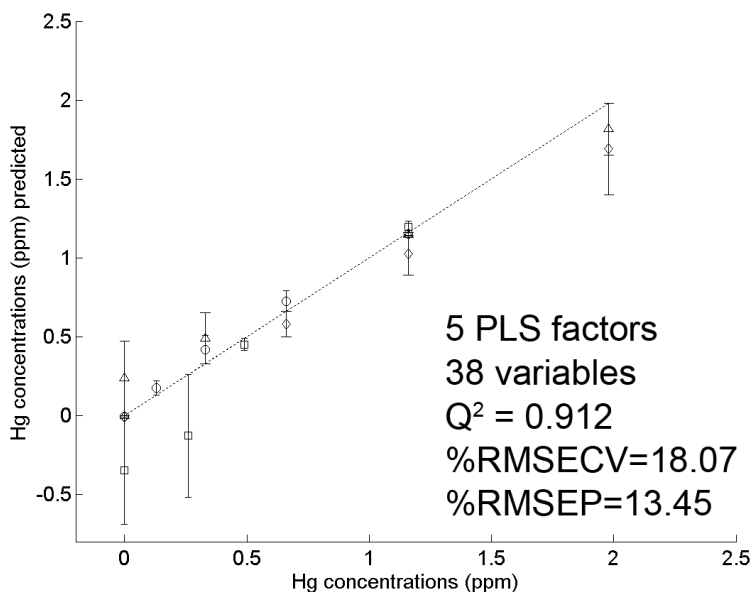


Figure 3.16. Prediction plots of the walet+OSC PLS model-based for the validation data set: (o) set 1, (□) set 2, (◇) set 3, (△) set 4.

3.3.4.5 PLS with genetic algorithm

The heuristic variable selection has been carried out using the calibration dataset. Initially, the number of variables of the whole spectrum was reduced to 111 by a decimation factor of 5. If the variables/objects ratio is very high, GA may not be used since it would model noise instead of information³⁰. After decimation, the compromise between the number of variables and object measurements is met, and this allows for a fine control of the algorithm. Several configurations with a varying number of chromosomes, number of variables within each chromosome and deleting groups were tested with PLS predictions using data from the training dataset.

Figure 3.17 resumes the steps involved in the genetic algorithm pre-treatment and PLS model construction. The initial results emphasized that the number of chromosomes and the maximum number of variables per chromosome were the most influencing parameters on model performance. Therefore, a fine control of these parameters provided the best choice: 20 chromosomes considering up to 30 variables, an average of 5 selected variables in the chromosomes for the starting population and 5 deleting groups. The mutation probability was set to 1%, the cross-over probability to 50%. The number of iterations for a given search (i.e. the number of generations) was set to 100 and 50 evaluations per generation were performed.

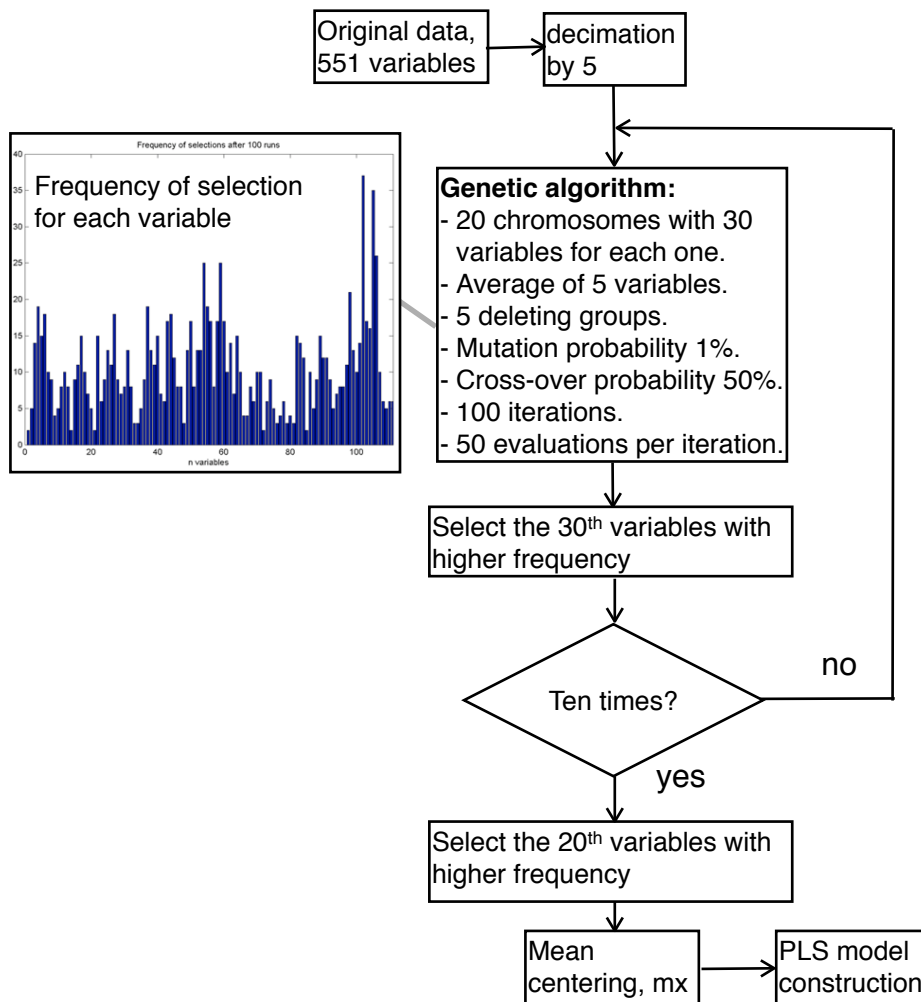


Figure 3.17. Scheme of the GA-PLS model construction.

Due to the stochastic nature of this search, results (i.e. the variables selected after a search process is conducted) would not be necessarily the same for different search runs. For this reason, ten runs of the algorithm were performed. After each run, the 30 variables with higher selection frequencies are retained. At the end of the tenth run, only the 20 most

frequently selected wavelengths (over the ten runs) were finally identified as those to be employed for building the PLS calibration model. The computational time of the heuristic-searched process was 20 minutes. The RMECV versus the PLS factors was computed on training data. The optimum model was achieved with 5 latent variables. Subsequently, the model was tested using validation data. The use of the GA for variable selection results in a PLS model with improved prediction ability compared to the previous PLS models developed (see Figure 3.18b).

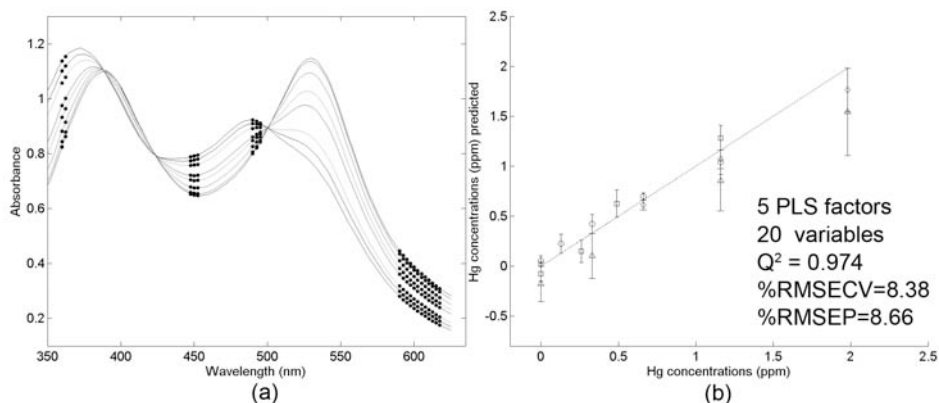


Figure 3.18. (a) Hg²⁺ titration and selected wavelengths by genetic algorithm. (b) Prediction plots for GA-PLS model corresponding to validation data set: (o) set 1, (□) set 2, (◇) set 3, (△) set 4.

The spectral subset provided by GA seems to be a logical interpretation from the spectroscopic point of view. In Figure 3.18a three regions have been highlighted: the band at $\lambda=500\text{-}625$ nm which corresponds to the characteristic N719 absorbance peak, the band at $\lambda=425\text{-}500$ nm,

assigned to the mercury complexation, and the selected variables located at the band at $\lambda=350-400$ nm which matches most part of data removed by OSC. The latter region is more influenced by interferential effects and also needs to be considered in the quantification process.

3.3.4.6 PLS with wavelet + OSC + GA

The combination of compression, signal correction and heuristic variable selection has been tested. The genetic algorithm was performed with the same parameters described above; in parallel, several runs were tested for different wavelet functions. Finally, Coiflet-4 at five level carried out a compression to 38 wavelet coefficients. Subsequently, the data was properly scaled by *mean-centering* before applying orthogonal signal correction. Prior to the GA process the calibration data was rescaled. Thus, after ten runs the 21st variables with higher frequency of selection were considered as the subset for building the PLS models. The calibration data was subjected again to mean centering before model building.

From the RMSECV employing training data, it was derived that the optimal adjustment corresponded to 2 PLS components. The RMSEP for the validation data is shown in Figure 3.19. Both RMSECV and RMSEP emphasize the consistency of the model and show a slight improvement in its predictive ability (compared to the one reached with the GA only). This combination of techniques constitutes the most complex solution evaluated in this work.

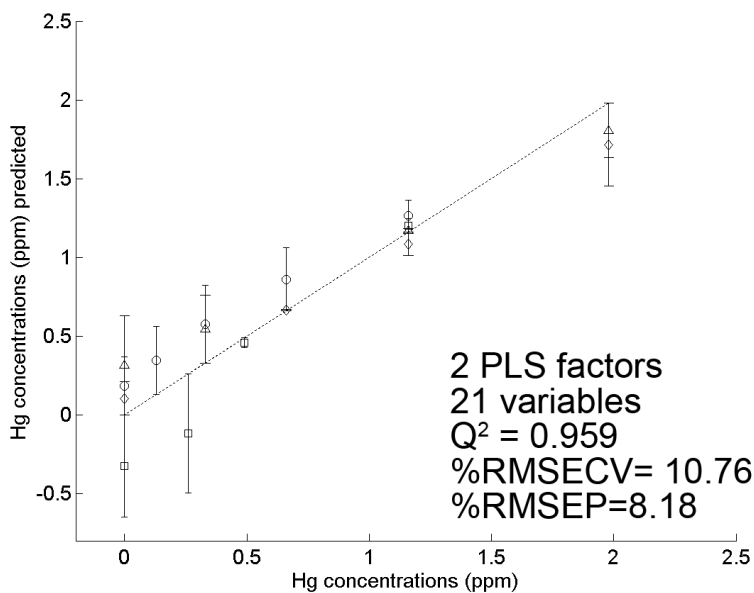


Figure 3.19. Prediction plots of the wavelet-OSC-GA-PLS model for the validation data set: (o) set 1, (□) set 2, (◇) set 3, (△) set 4.

3.3.4.7 PLS with statistical feature selection

Going ahead with the last technique studied, the calibration set was redistributed into four categories according to different mercury levels (0, 0.49, 1.49 and 2.98 mg L⁻¹), and considering also the whole concentration levels of other metals. This classification data is used only for the SFS construction, meanwhile, the whole calibration data set described in Table 3-I is employed for the PLS model construction. In both cases, the data was decimated by a factor of 5, giving rise to 111 variables.

TABLE 3-III. Classification of the calibration data for the SFS treatment.

	Analyte concentration	Interferential mixtures
Category 1	--	Several measurements with none, low and high concentration of interferential elements
Category 2	Low	
Category 3	Medium	
Category 4	High	

Next, the discrimination function (DF) was obtained considering the two types of variance calculated (intra-category and inter-category variance). A fine adjustment of the discrimination factor may modify the number of wavelengths selected from different regions of the spectra. Therefore, a comparison between the results obtained using several DF thresholds and the performance of their corresponding PLS models (employing data from the training dataset) was performed. An optimum threshold provided a selection of 69 wavelengths, but the large amount of contiguous variables observed pointed out the existence of some redundant features. In fact, as Figure 3.20a shows, the DF plot reveals that by applying only one threshold masks local peaks that may contain important information. The technique employed here for reducing redundant features consisted in the use of weighted Gaussian kernels centered on the peaks located above the DF threshold applied. Consequently, the contribution of the variables (λ_k) around each DF peak

$(\lambda_{peak,i})$ have been modeled by symmetric Gaussian functions, which have a peak width (σ^2) that is proportional to the value of the DF :

$$G = e^{-\frac{(\lambda_k - \lambda_{peak,i})^2}{2\sigma^2}} \quad (3.18)$$

Hence, four peaks were modelled at 360, 475, 520 and 575 nm, giving rise to a new DF vector represented in Figure 3.20b.

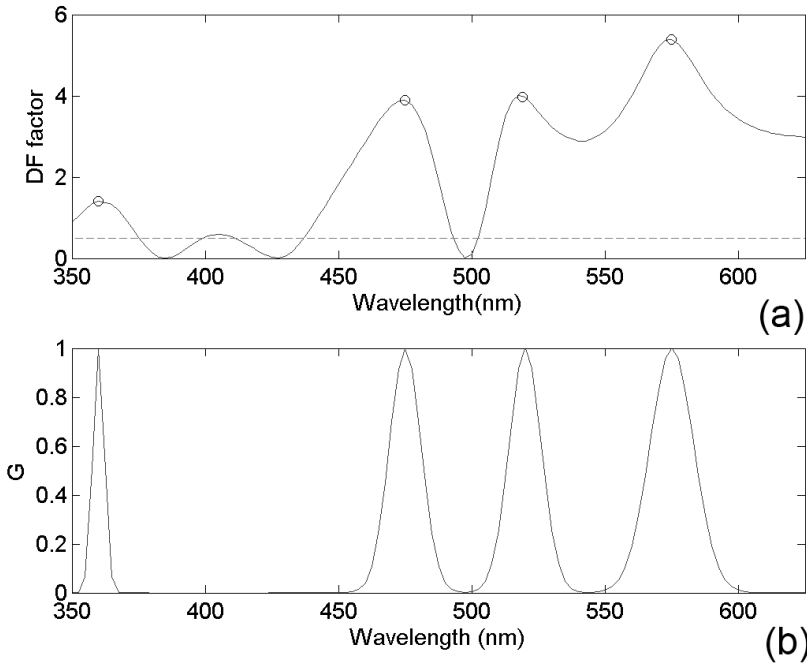


Figure 3.20. (a) Discrimination factor function with local peaks, and (b) weighted Gaussian kernels plot used for reducing spectral variables in SFS.

Now, the control of the variable selection is finely adjusted by varying the maximum width of the Gaussian functions. Next, a fixed threshold (at 50% of the vector values) on the kernel functions provided the variable subsets. Finally, the optimal adjustment was obtained through $\sigma_{max}= 3.3$, resulting in only 20 wavelengths being selected (see Figure 3.21a). This subset was tested with PLS predictions on the training data and the optimum model corresponded to 7 PLS factors. The results obtained using SFS (see Figure 3.21b) on the validation set show that this solution is closer to the global optimum. Additionally, the method results in a reduction of the prediction variance within the measurement range. Moreover, the computational simplicity of the method enables a fast search to be conducted (0.26 seconds), thus facilitating the adjustment procedure.

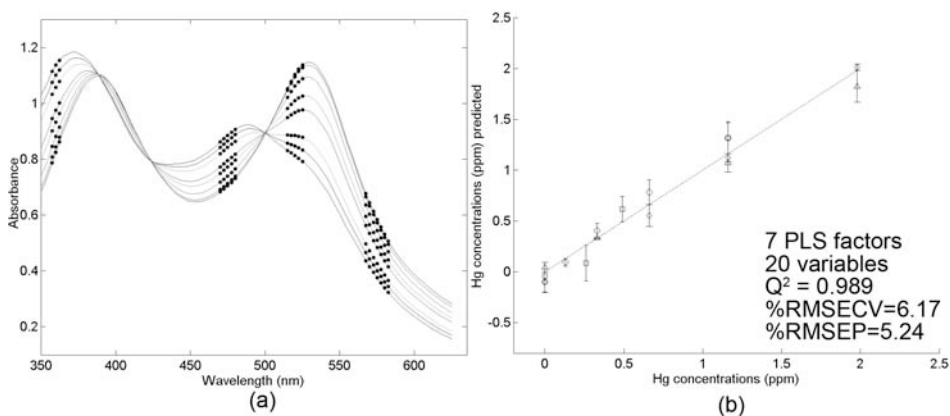


Figure 3.21. (a) Hg^{2+} titration and selected wavelengths by SFS. (b) Prediction plots for SFS-PLS model corresponding to validation data set: (o) set 1, (\square) set 2, (\diamond) set 3, (\triangle) set 4.

3.3.4.8 PLS with extended statistical feature selection

In order to explore whether synergic effects between variables exist and their contribution to the analyte determination, the method proposed is based on the same statistical rules employed above but considering all pair combinations of spectral variables. Figure 3.22 illustrates an hypothetical case, wherein the spectral absorbance of paired wavelengths is projected into a two-dimensional plane, the mean values corresponds to centroids, and Euclidean distances provide for the category variances.

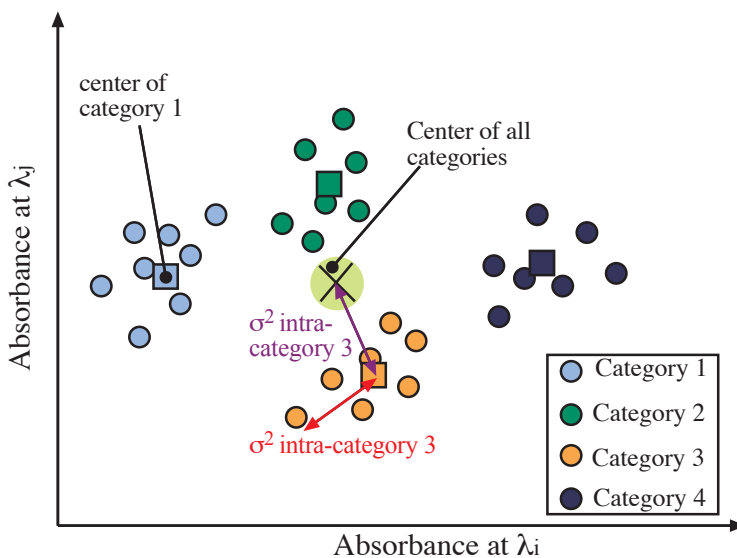


Figure 3.22. Geometrical interpretation of the extended feature selection.

Initially, 111 wavelengths were obtained after decimating by a 5 factor, so that a total of 5995 combinations generated a vector in which each element was associated to the corresponding wavelength pair. In each

cycle, a variable is combined with the rest, so that a signal variation appears due to the changes of intra-variance distance. DF is calculated for all the variable combinations, and finally, the peaks of each cycle generate the envelope of interest. Similarly to the univariate SFS, a fixed DF threshold provided a large subset of contiguous variables. Also in agreement with the univariate SFS, Gaussian Kernels were used to reduce redundant variables. In order to achieve this reduction, the kernels were located at DF peaks corresponding to the paired wavelength locations: $\lambda=415-535$ nm, $\lambda=547-622$ nm, $\lambda=620-622$ nm. The training set adjustment gave as a result a maximum kernel width (σ_{max}) of 3.3, yielding a subset of 20 variables. The searching procedure, which took into account all possible combinations of two wavelengths, was also fast (i.e., time of calculus was 8.8 seconds). As a consequence of this analysis, a new spectral region, located at the $\lambda=400-425$ nm, emerged as important (see Figure 3.23a). The PLS model reached an optimum performance on training measurements when 6 components were used. The evaluation of the model using the validation dataset resulted in a RMSEP slightly higher to the one obtained when the univariate SFS approach was employed. However, the multivariate SFS performs better than the other pre-processing methods studied (see Figure 3.23b).

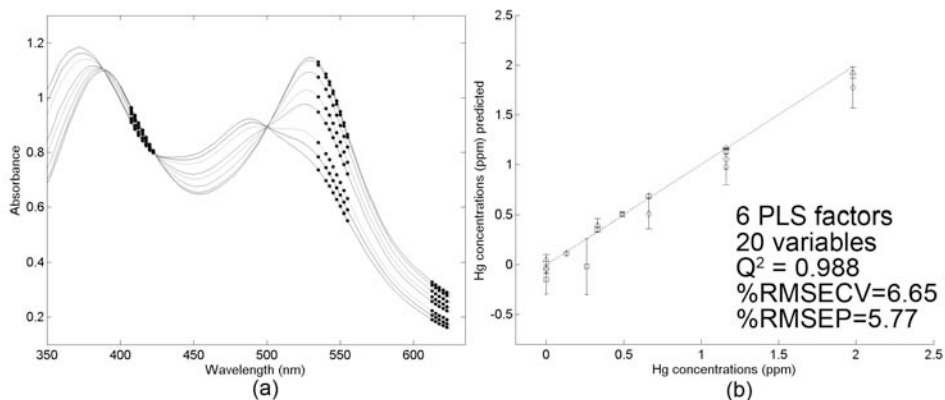


Figure. 3.23. (a) Hg²⁺ titration and selected wavelengths by extended statistical feature selection. (b) Prediction plots for extended SFS-PLS model corresponding to validation data set: (o) set 1, (□) set 2, (◇) set 3, (△) set 4.

Among the different pre-treatment applied before PLS modeling, the statistical features selection can deal best with the spectral interferences introduced by foreign metal ions. Table 3-IV resumes all the pre-treatment, wherein both SFS methods shows clearly a low error of prediction, and fast time of computing if it is compared with the other techniques.

TABLE 3-IV. Pre-processing methods comparison and their PLS prediction for validation data set.


	Number of variables	PLS factors	Q ²	%RMSECV	%RMSEP
None pre-treatment	551	3	0.961	11.93	10.48
Decimation by 12	46	3	0.962	11.83	10.46
Wavelet	38	4	0.889	20.25	14.97
OSC	46	2	0.987	6.90	12.61
Wavelet+OSC	38	5	0.912	18.07	13.45
GA	20	5	0.974	8.38	8.66
Wavelet+OSC+GA	21	2	0.959	10.76	8.18
SFS	20	7	0.989	6.17	5.24
Extended SFS	20	6	0.988	6.65	5.77

3.4 References

- (1) Bro, R. *Analytica Chimica Acta* **2003**, *500*, 185-194.
- (2) Walczak, B. *Analytica Chimica Acta* **1996**, *322*, 21-29.
- (3) Gulbag, A.; Temurtas, F. *Sensors and Actuators, B: Chemical* **2006**, *B115*, 252-262.
- (4) Dieterle, F.; Busche, S.; Gauglitz, G. *Analytica Chimica Acta* **2003**, *490*, 71-83.
- (5) Andrew, K. N.; Rutan, S. C.; Worsfold, P. J. *Analytica Chimica Acta* **1999**, *388*, 315-325.
- (6) Gemperline, P. *Practical Guide to Chemometrics*, second edition ed.; Taylor & Fancis Group, 2006, 139-140.
- (7) de Jong, S. *Chemometrics and Intelligent Laboratory Systems* **1993**, *18*, 251-263.
- (8) Wise, B. M.; Gallagher, N. B.; Bro, R.; Shaver, J. M.; Winding, W.; Kotch, R. S.; Eigenvector, pp 147-149.
- (9) Geladi, P. *Chemometrics and Intelligent Laboratory Systems* **2002**, *60*, 211-224.
- (10) Real, B. D.; Ortiz, M. C.; Sarabia, L. A. *Talanta* **2007**, *71*, 1599-1609.
- (11) Hubert, M.; Vanden Branden, K. *Journal of Chemometrics* **2003**, *17*, 537-549.
- (12) Moeller, S. F.; von Frese, J.; Bro, R. *Journal of Chemometrics* **2006**, *19*, 549-563.

- (13) Capron, X.; Walczak, B.; de Noord, O. E.; Massart, D. L. *Chemometrics and Intelligent Laboratory Systems* **2005**, *76*, 205-214.
- (14) Xu, L.; Jiang, J.-H.; Lin, W.-Q.; Zhou, Y.-P.; Wu, H.-L.; Shen, G.-L.; Yu, R.-Q. *Talanta* **2007**, *71*, 561-566.
- (15) Dieterle, F.; Busche, S.; Gauglitz, G. *Analytical and Bioanalytical Chemistry* **2004**, *380*, 383-396.
- (16) Trygg, J.; Wold, S. *Chemometrics and Intelligent Laboratory Systems* **1998**, *42*, 209-220.
- (17) Walczak, B.; Massart, D. L. *Chemometrics and Intelligent Laboratory Systems* **1997**, *38*, 39-50.
- (18) Walczak, B.; Bouveresse, E.; Massart, D. L. *Chemometrics and Intelligent Laboratory Systems* **1997**, *36*, 41-51.
- (19) Wold, S.; Antti, H.; Lindgren, F.; Ohman, J. *Chemometrics and Intelligent Laboratory Systems* **1998**, *44*, 175-185.
- (20) Esteban-Diez, I.; Gonzalez-Saiz, J. M.; Pizarro, C. *Analytica Chimica Acta* **2004**, *514*, 57-67.
- (21) Eriksson, L.; Trygg, J.; Johansson, E.; Bro, R.; Wold, S. *Analytica Chimica Acta* **2000**, *420*, 181-195.
- (22) Esteban-Diez, I.; Gonzalez-Saiz, J. M.; Pizarro, C. *Analytica Chimica Acta* **2005**, *544*, 89-99.
- (23) Yuan, M.; Lin, Y. *Journal of the American Statistical Association* **2005**, *100*, 1215-1225.
- (24) Tadesse, M. G.; Sha, N.; Vannucci, M. *Journal of the American Statistical Association* **2005**, *100*, 602-617.
- (25) Setarehdan, S. K. *Journal of Chemometrics* **2007**, *20*, 239-246.

- (26) Norgaard, L.; Saudland, A.; Wagner, J.; Nielsen, J. P.; Munck, L.; Engelsen, S. B. *Applied Spectroscopy* **2000**, *54*, 413-419.
- (27) Xu, L.; Jiang, J.-H.; Zhou, Y.-P.; Wu, H.-L.; Shen, G.-L.; Yu, R.-Q. *Chemometrics and Intelligent Laboratory Systems* **2007**, *87*, 226-230.
- (28) Andersson, F. O.; Aberg, M.; Jacobsson, S. P. *Chemometrics and Intelligent Laboratory Systems* **2000**, *51*, 61-72.
- (29) Hoerchner, U.; Kalivas, J. H. *Analytica Chimica Acta* **1995**, *311*, 1-13.
- (30) Leardi, R.; Lupianez Gonzalez, A. *Chemometrics and Intelligent Laboratory Systems* **1998**, *41*, 195-207.
- (31) Llobet, E.; Gualdron, O.; Vinaixa, M.; El-Barbri, N.; Brezmes, J.; Vilanova, X.; Bouchikhi, B.; Gomez, R.; Carrasco, J. A.; Correig, X. *Chemometrics and Intelligent Laboratory Systems* **2007**, *85*, 253-261.
- (32) Palomares, E.; Vilar, R.; Durrant, J. R. *Chemical Communications (Cambridge, United Kingdom)* **2004**, 362-363.
- (33) Leardi, R.; www.models.kvl.dk.
- (34) Kalivas, J. H. *Analytica Chimica Acta* **2001**, *428*, 31-40.
- (35) Esteban-Diez, I.; Gonzalez-Saiz, J. M.; Gomez-Camara, D.; Millan, C. P. *Analytica Chimica Acta* **2006**, *555*, 84-95.



4 Immobilization Of The Molecular Probe

CONTENTS

- 4. 1 Introduction to meso-porous metal oxide films
- 4. 2 Optical support preparation and characterization
- 4. 3 N719/Al₂O₃ film response
- 4. 4 References

4.1 Introduction To Mesoporous Metal Oxide Films

In the construction of a chemical sensor, the support structure plays an important role because it allows the molecular probe to be incorporated into a fully integrated device. In the first place, it must serve as the liquid-solid or gas-solid interface allowing the transmission of the analytical signal, so far as possible without any disturbance addition. Secondly, it must facilitate an efficient coupling to the transduction platform, such as optical fibers or waveguides. Thirdly, working in solid-liquid phase simplifies the measurement process, making it easier and faster, as the functionalized surface saves the researchers several intermediate steps.

Nowadays, there is an increasing demand of multiphase and nanostructured materials for multiple applications such as smart sensors, photovoltaic devices, and organic light emitting diodes (OLED's). There is a number of materials that may be used as molecular supports, such as polymers, membranes, and films. First of all, we have selected metal oxide films as optical support due to the ability of N719 to anchor to their nanocrystalline particles. The good physical properties, such as mechanical resistance and optical transmittance, and the easy preparation by sol-gel of these films, makes this kind of material good candidates to play with an optical fiber platform. Moreover, the use of transparent, high

surface area, mesoporous semiconductor metal oxide films allows not only the use of optical detection systems but also the use of electrochemical methods. In this chapter we will discuss the most common methods for the synthesis of the nanocrystalline particles that we have employed during the experimental work.

1.1 Sol-gel method

The sol-gel method is a low temperature process used to produce optically transparent thin films obtained from a colloidal suspension of solid particles (normally metal alkoxides) in a liquid (sol), which undergoes polymerization and gelation to produce a homogeneous metal-oxide network (the gel). After heating to remove organic solvents or water inside the gel, a solid structure with small pores is generated. Several deposition techniques are available for coating with sol-gel such as dip-coating, spin coating and screen printing. Paste viscosity, gravity forces, particle size and other factors that depend of the coating technique employed control the film thickness. Moreover, the response time of the sensitive material may be affected by the thickness, pore size, and hydrophobicity of the film. The dye can be incorporated within the gel, or adsorbed or grafted (covalently attached) onto the film surface after annealed. Compounds such as tetraorthoethylsilicate (TEOS) and other alkoxides (titanium iso-propoxides, etc...) are generally used as starting materials which act as template.

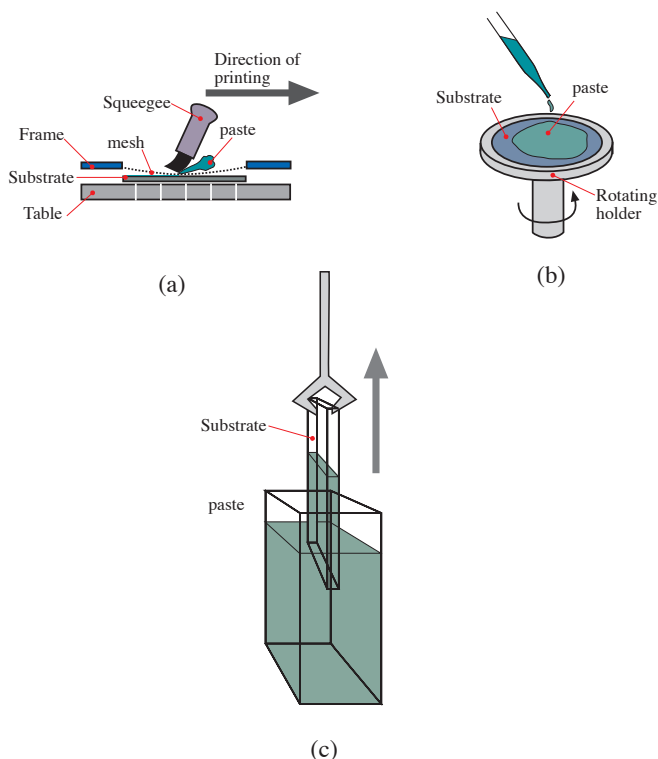


Figure 4.1.
Deposition
techniques for
coating
materials. a)
screen printing,
b) spin coating,
and c) dip
coating.

The sol-gel technique has extensively used for applications such as glasses, ceramics, catalysis, etc. A closed application field is dye solar cells, wherein the light energy absorbed by the dye is transferred into the semiconductor through the injection of electrons that will be transported by the semiconductor metal oxide, such as TiO_2 , to the external contacts. In fact, dye solar cells constitute the main application of the N719, because it was designed for that purpose. Herein the interaction of the carboxylic groups of N719 with Ti ions on the surface is likely to lead to the formation of covalent C-O-Ti bonds¹.

On the other hand, there is an extensive work on the immobilisation of small molecules for cation detection in organic polymer matrices (see examples in Chapter 2). Advantages attributed to the sol-gel films over organic polymers are: (1) transparency, (2) chemical durability and (3) better stability of the trapped molecules².

In resume, a solid support suitable for anchoring small molecules and absorbance measurements must fulfil:

- ▶ Optical transparency.
- ▶ Homogeneity.
- ▶ Suitable structure for supporting the molecules.
- ▶ Permeable to the analyte.
- ▶ Reproducibility.
- ▶ Stability.

Thus, all of the above requirements have been achieved with the sol-gel technique, whereas stability constitutes the main drawback in many applications due to leaching of the reagent from the inorganic support. The same occurs using TiO₂-N719 as mercury sensor in aqueous medium, where the first inconvenient can be molecule desorption. This fact is due to the strong polarity of water that can be “break” titania-dye bonds. In this sense, a great contribution of this work in order to overcome dye-desorption problems consists in the use of acid treated Al₂O₃ films as immobilisation support of the dye. An advance of these results can be seen in Figure 4.2 where the stability of N719/TiO₂ films

and N719/Al₂O₃ is compared. We would like to notice that a few drops of nitric acid were added to the alumina paste. Next sections describe the paste preparation and characterization of aluminium oxide films showing their good properties as optical support for small molecular probes.

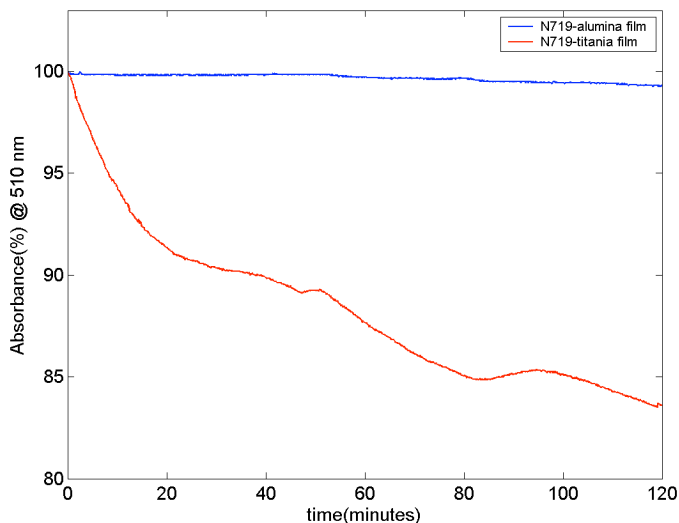


Figure 4.2. Stability comparison of N719/Al₂O₃ and N719/TiO₂ films immersed in pure water.

4.2 Optical Support Preparation And Characterization

In this work alumina films have been employed as a mesoporous transparent support for N719. The performance of the sensitized Al₂O₃ films was compared to TiO₂ films in order to check the benefits of the former for mercury sensing in water.

4.2.1 Preparation of thin films

Aluminium oxide nano-particles with a diameter of 50 nm in aqueous (20%) colloidal dispersion were purchased from Alfa Aesar. Hydroxypropyl cellulose, Mw 370.000, was provided by Sigma Aldrich. The TiO₂ paste was purchased from Solaronix. Following the sol-gel method procedure, aluminium oxide nano-particles were used as starting material. Nano-crystalline particles are very difficult to disperse in an organic phase due to their tendency to form aggregates. In order to break the aggregates into separate particles, 15 mL of Al₂O₃ collide was put into a flask and 0.35 gr. of hydroxypropil cellulose was slowly added under vigourous stirring. The hydroxypropyl cellulose prevents the re-aggregation of the particles. The mixture in the flask was stirred for at least seven days at 60-70 °C. Sometimes, shaking up and down by hand allows to dissolve the polymer completely prior film deposition. Finally, the resulted paste was cooled down prior to keep it in the refrigerator or use. Several experimental results published on the scientific literature³ show that controlling optimal reaction conditions, such as the pH value of hydrolysis, temperature and the time during the heat treatment, can optimise the metal oxide particle size. In our case, the main variables involved were only the temperature and heating time during the stirring.

A preliminary characterization of the paste was done with the alumina and the titania films prepared onto a transparent glass support. The preparation of the thin films was conducted following a technique

commonly know as *doctor blade* which consist on spreading with a glass rod sliding over two parallel edges with adhesive tape (~40 μm thick) the metal oxide paste as shown in the Figure 4.3. After that, the films were annealed at 450 $^{\circ}\text{C}$ during 90 minutes.

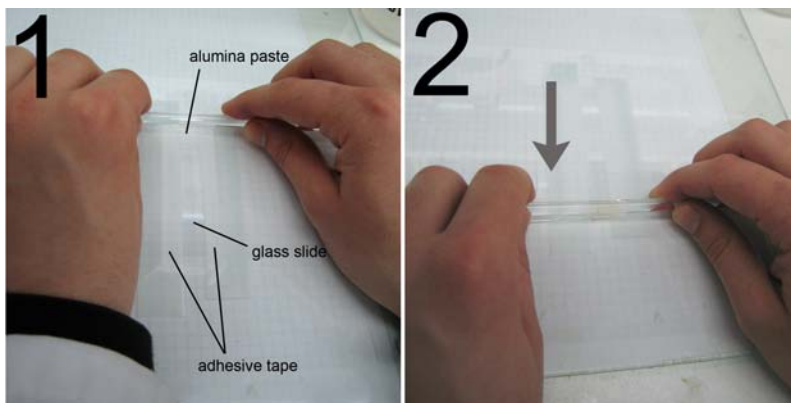


Figure 4.3. Doctor blade deposition of alumina paste onto glass support.

The final thickness of alumina films was 8.34 micrometers thick (see Figure 4.4a). An identical procedure was employed for the TiO_2 films being the commercial paste suitable for dispersing directly on the glass substrate. See in Figure 4.4b the scanning electron microscope image of the Al_2O_3 film, wherein the porous structure may allow to bind dye molecules inside the cavities, and thus the surface are is strongly increased.

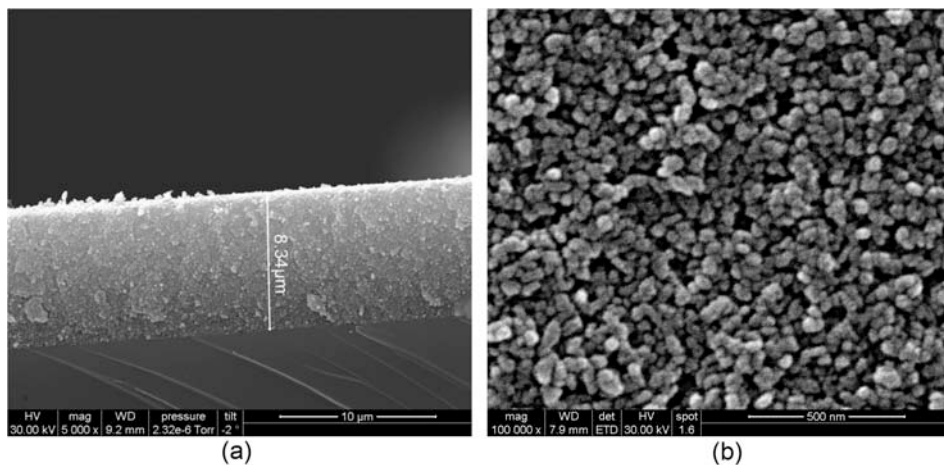


Figure 4.4. Scanning electron microscope (SEM) image of cross section of alumina film deposited on glass support.

4.2.2 Physical characterization of Al_2O_3 films

The nanocrystalline mesoporous alumina films is an appealing material due to its properties such as non-toxic, stable, insulating and transparent, which it makes interesting for applications in many different areas such as in glassmaking, cosmetics, medicine, ceramics, etc. Alumina exists in a number of crystalline phases (polymorphs), three of the most important being γ , θ , α . The common alumina polymorphs can all be formed from room temperature up to about 1000 °C, see Figure 4.5.

Some properties of the different alumina phases are:

- γ -alumina. This kind of structures is widely used as catalyst support. The principal features are low surface energy, being stabilized when the surface area is high. Cubic crystals compose

gamma alumina with aluminium ions more or less randomly distributed between octa- and tetrahedral sites⁴.

► θ -alumina. The θ phase is metastable being highly ionic and insulating with a well-defined crystal structure, in contrast to gamma phase. Half of the aluminium ions occupy octahedral interstitial sites and half occupy tetrahedral sites.

► α -alumina. This phase is also known as corundum. It is transparent and uncoloured. Similarly to the case of θ -alumina is highly ionic, thus the chemical bonds are almost purely ionic. The aluminium ions occupy two thirds of the octahedral interstices with six oxygen nearest neighbours. The alpha alumina has high thermodynamic stability and it is chemical inertness and high hardness with more density than θ -alumina. This makes α -alumina feasible for wear-resistant coatings.

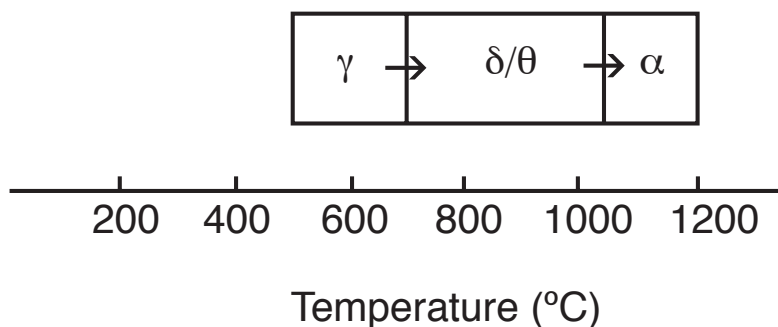


Figure 4.5. Transition sequences of the principal alumina phases.

On the other hand, the size of the metal oxide nano-particle has significant influence on the amount of the dye that can be adsorbed onto the mesoporous film. If the size of particle is too small and the pore size of the metal oxide is not large enough to hold the dye molecule, the amount of the dye adsorbed will be low. In contrast, if the particle is too big the ratio of the surface area to the volume of metal oxide will be reduced. Moreover, the structure of the film has a great effect on the diffusion time and interaction with the analyte; hence the response time and sensitivity of the probe will be affected. Several characterization techniques were employed in order to estimate the structure and particle size of the meso-porous alumina films.

4.2.2.1 X-ray diffraction

Probably the most important technique to determine the crystal structure of a sample is the x-ray diffraction (XRD). A beam of x-rays is projected into the sample and the resulting diffracted beams are detected. A crystalline structure will show a diffraction pattern of beams that vary in different directions depending on the orientation of the crystal planes. Finally, the diffraction pattern characteristic of the crystal structure is obtained from both incident (ω) and detected angles (θ) with respect to the sample surface. The phase composition of the Al_2O_3 crystalline nanoparticles was determined using x-ray diffraction technique. The peak positions and relatively intensities of the powder pattern were identified by comparison with powder diffraction reference data. Figure 4.6a shows

the diffraction pattern obtained for the alumina films, which indicates that the crystalline structure formed is bohemite- $\alpha\text{-Al}_2(\text{OOH})_2$. This structure differs from γ -alumina, which was the phase with more probabilities to be formed due to the employed annealing temperature of 450°C. Hence, the aqueous environment may have an important role in the final structure of alumina. Studies performed by Park and co-workers⁵ further explain this structure formation as a consequence of an exothermic hydrolytic reaction of Al particles with H₂O molecules. In the case of the nano-crystalline mesoporous titania films that were annealed also at 450 °C we observed a crystalline structure composed by a mixture of anatase and rutile phases as expected from previous literature reports, see Figure 4.6b.

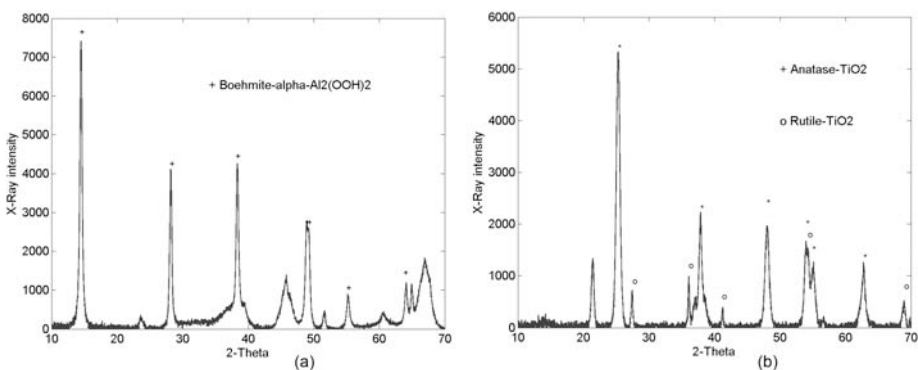


Figure 4.6. XRD pattern of: (a) alumina nano-particles, and (b) titania nano-particles, after annealing at 450 °C during 90 minutes.

4.2.2.2 Specific surface area

A useful method to measure the specific surface area and pore size distribution of powdered or solid materials is the gas sorption technique. This method employs an inert gas, such as nitrogen, which is adsorbed on the surface of the sample at low temperature. The specific surface area is provided by the Brunauer-Emmett-Teller (BET) method that establishes the volume of gas needed to form a mono-layer on the surface of the sample. Therefore, the surface area can be calculated from knowledge of the size and number of the adsorbed gas molecules. The average particle size D_{BET} can be obtained by assuming that the powders are consisted of separated spherical particles, following the next equation⁶:

$$D_{BET} = \frac{6}{S_{BET} \cdot \rho} 10^{-6} \quad (4.1)$$

where S_{BET} is the superficial area and ρ is the density of the material. The S_{BET} of alumina nano-particles measured in an Autosorb 1-MP of Quantachrome was 219.7 m²/g. Moreover, from the theoretical alumina density provided by the manufacturer (=1.06 g/cm³), the resulting average particle diameter from the alumina films was 25.7 nm, and an average pore diameter of 7.3 nm.

On the other hand, the superficial area of titania paste was 156.5 m²/g, and an average pore diameter of 17.6 nm. The average size of particle considering a titania density of 3.98 g/cm³ was 96.63 nm.

TABLE 4-I. Characteristics of alumina and titania films obtained from BET method.

	Al ₂ O ₃	TiO ₂
S _{BET}	219.7	156.5
Density (g/cm ³)	1.06	3.98
Average particle diameter (nm)	25.7	96.63
Average pore size (nm)	7.3	17.6

4.2.2.3 Transmission electron microscopy (TEM)

The TEM operates in the same manner of conventional microscopes but using an electron beam instead of light. In this manner, this technique can observe objects in the order of angstroms (1 Å= 10⁻¹⁰ meters). Some sample treatments are needed in order to achieve a sample thin enough to be electron transparent. Depending on the density of the material some of the electrons are scattered or directly projected into the sensitive screen. The result is an image with varied grey levels according to density of the sample. In our case, a powder composed by nano-crystalline Al₂O₃ particles was dissolved in ethanol and stirred with ultrasound. After that, a TEM image of the solution containing the Al₂O₃ nano-particles dispersed on a grid was captured. As illustrated in Figure 4.7, there is agglomeration present which difficulties an accurate estimation of the particle size, but some of them were identified with a diameter around 20-30 nm.

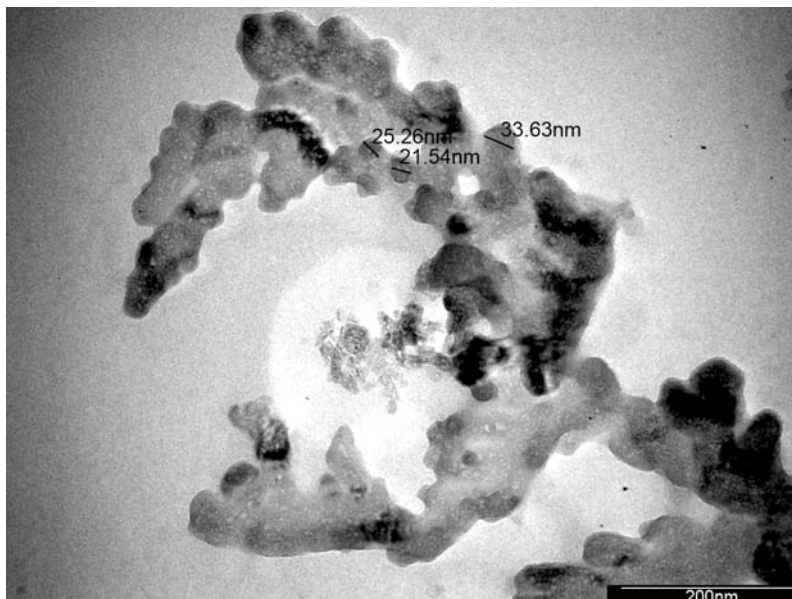


Figure 4.7. TEM image of Al_2O_3 nanoparticles.

4.2.2.4 Atomic force microscope (AFM)

In this technique the movements of a cantilever tip scan the sample surface. Several forces (electrostatic, capillary, magnetic, etc.) are involved on the deflections of the cantilever, but the principal methods for detecting the cantilever deflections are carried out by laser or capacitance measurements. Consequently, the AFM was used in order to observe the alumina film in the nanometer scale with higher resolution than the one obtained using the TEM. Figure 4.8 shows both thin mesoporous films of alumina and titania nano-particles, which enclose cavities that allow dye diffusion through the nano-porous and subsequent formation of the covalent bond to attach the dye onto the nano-particle

surface. It is appreciable that the alumina films have more uniformity in the particle size around 30-40 nm, while TiO₂ films are a mixture of different particle sizes.

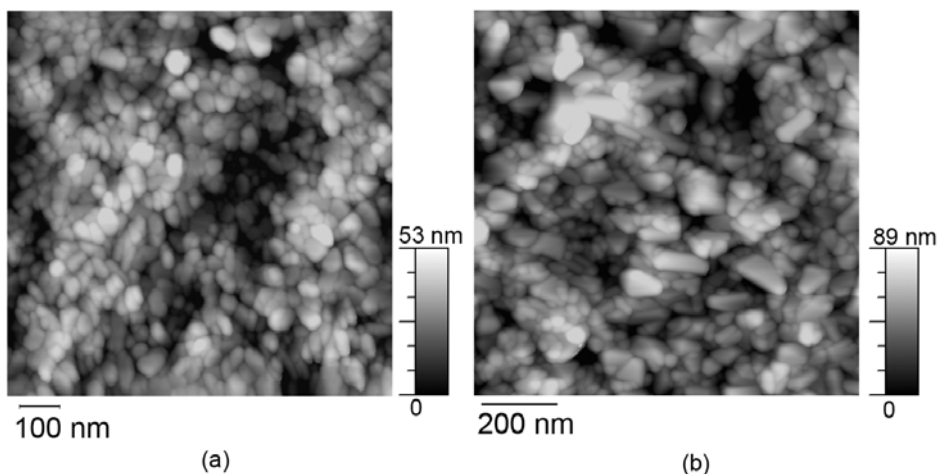


Figure 4.8. AFM images; (a) alumina film, (b) titania film.

4.2.2.5 Optical properties

Absorbance measurements were made on a double beam UV-Visible Shimadzu 1700 spectrometer. The low absorbance measured for the alumina coating reveals the good transparency of the film compared with the titania film which has a strong absorption at the near Visible region of the spectra (below 400 nm), see Figure 4.9. Therefore, the better optical transmission of alumina films allows to observe more spectral information of the anchored indicators in the uv-visible spectrum than titania films.

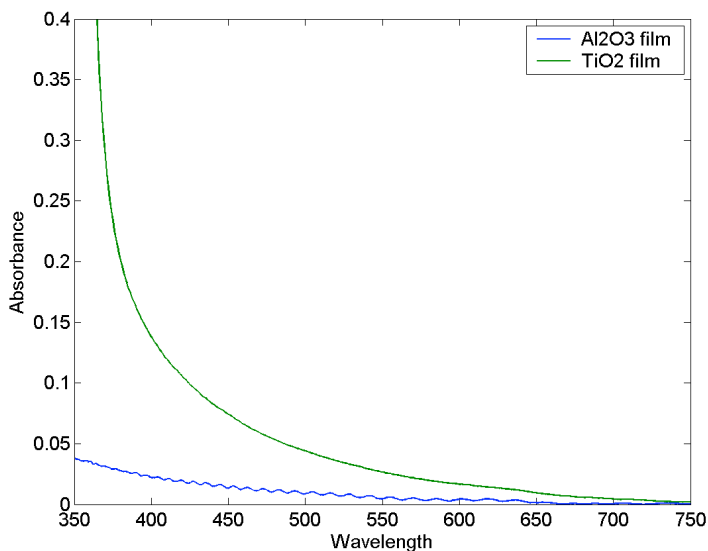


Figure 4.9. Absorbance measurements of alumina and titania thin films

4.2.3 N719 adsorption onto Al₂O₃ films

The N719 molecules can be directly attached to the nano-particle surface through covalent bonds such as the ones observed between the carboxylate groups of the N19 dye and the hydroxyl groups at the surface of the nano-crystalline TiO₂ particles⁷. In general, a low concentration of molecules adsorbed onto the film can lead to a low detection limit, but saturation and desorption effects are more remarked and will have a negative effect on the measure too. In our case, the sensitized films can be obtained dipping the films in ethanolic solution of N719. The optimum dye concentration for the nanocrystalline mesoporous alumina films was obtained following the same procedure applied by Zhi-xue³ to

titania films. In brief, this experiment consists of a number of measurements focussed on the achievement of the proper concentration of molecule in the ethanolic solution by observing the dye concentration adsorbed onto film. Moreover, due to the fact that the dyes can be completely desorbed in alkaline solutions due to the rupture of the covalent bonds in basic solutions, we have an easy method to measure the amount of adsorbed dye onto the mesoporous film. For this reason, an aqueous solution of sodium hydroxide (pH 10) was used to study the dye desorption from the alumina thin films. Several concentrations of N719 dissolved in ethanol were mixed with sodium hydroxide water solutions, and the maximum peak of absorbance ($\lambda=500$ nm) was registered for each solution (see Figure 4.10a). Thereafter, alumina films were dipped in several ethanol solution of N719 at concentrations of: 84, 130, 170, 250, 340 and 420 μM . The alumina films were immersed in these solutions for 16 hours. Finally, all these films were desorbed in 3mL of water solution at pH 10, and the absorbance at $\lambda=500$ nm of the residual solution was registered. The amount of dye adsorbed onto the alumina film was calculated by the standard curve represented in Figure 4.10a. From Figure 4.10b it can be observed that the film is nearly saturated when the dye concentration reached above 300 μM , so this concentration level was selected as reagent stock solution for next sensitized films.

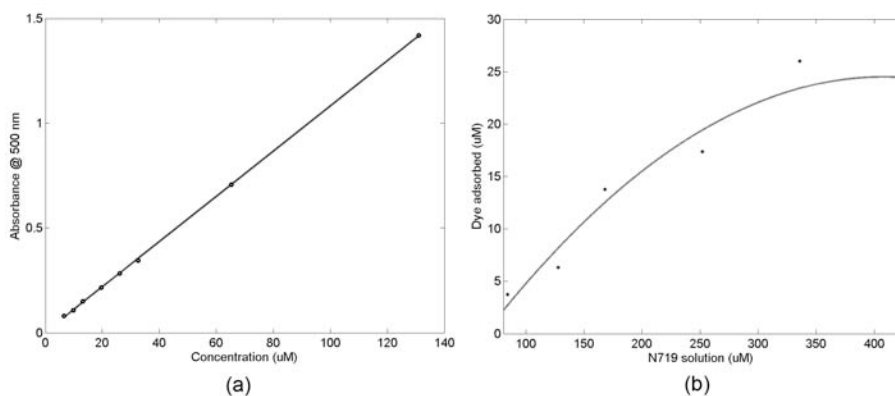


Figure 4.10. (a) Calibration plot of dye dissolved at pH=10 vs. absorbance measured at 500 nm. (b) Dye concentration and adsorption effect relationship of alumina films.

4.2.4 Stability of Al_2O_3 films

Previously to the use of hydroxypropil cellulose in the paste preparation, nitric acid (chemical formula HNO_3) was used as coagulant agent in order to prevent the re-aggregation of nano-particles. After that, when the nitric acid was substituted by hydroxypropil cellulose we observed that the former films, containing nitric acid, were more stable with less dye desorption issues in water. Therefore, if lower pH values may help to the formation of covalent bonds between the metal oxide film and carboxylic groups of the dye, several acid treatments on the alumina surface were experimented in order to prove the aqueous stability of the N719 sensitized mesoporous Al_2O_3 films. Accordingly, alumina films were prepared by spreading a viscous dispersion of Al_2O_3 particles on a glass

support with heating under air for 90 minutes at 450 °C. These films were soaked during 20 minutes in several acidic solutions at pH~1: boric, acetic, citric, sulphuric, phosphoric, hydrochloric and nitric acid followed by an additional annealing at 450°C were used. The stability measurements were performed by registering during 2 hours the absorbance spectrums of the sensitized alumina films immersed in pure water at room temperature. Figure 4.11 represents the dye desorption percentage corresponding to the absorbance changes at $\lambda=530\text{nm}$ of the films treated with the diverse acids. The results reveal that films treated with sulphuric acid were the most stables with a dye desorption below 3%.

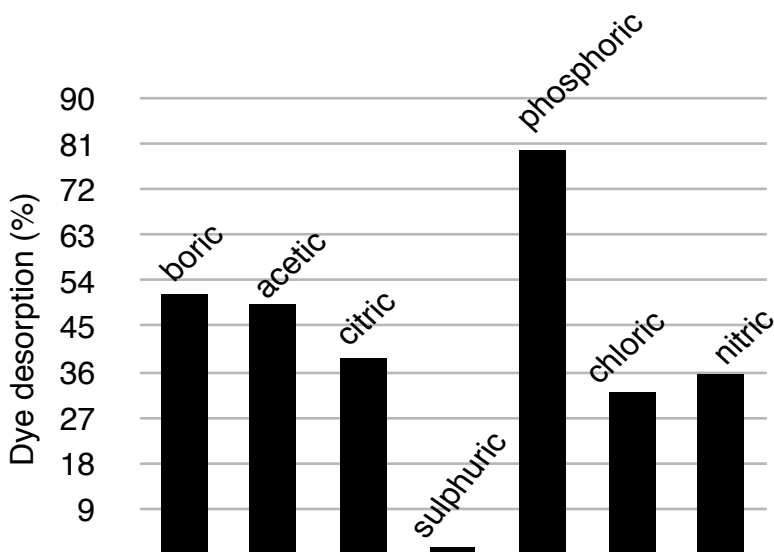


Figure 4.11. Desorption percentage of N719 anchored onto mesoporous alumina films treated with boric, acetic, citric, sulphuric, phosphoric, chloric, and nitric acid.

Moreover, another interesting effect was the shift observed in the first minutes when the dyed films were immersed in water. Figure 4.12 represents the absorbance spectrums registered for alumina films treated with sulphuric acid immersed in a quartz cuvette in pure water. From these plots, it can be observed two effects. First, the excess of dye that has not been anchored onto the film is lost in the solution during the first ten minutes, and second; we observe a shift on the Visible region of the spectra must surely due to the water pH. Consequently, we can only consider the sensitized films as stable for analytical measurements after 45 minutes when the UV-Visible spectra of the sensitized films does not change.

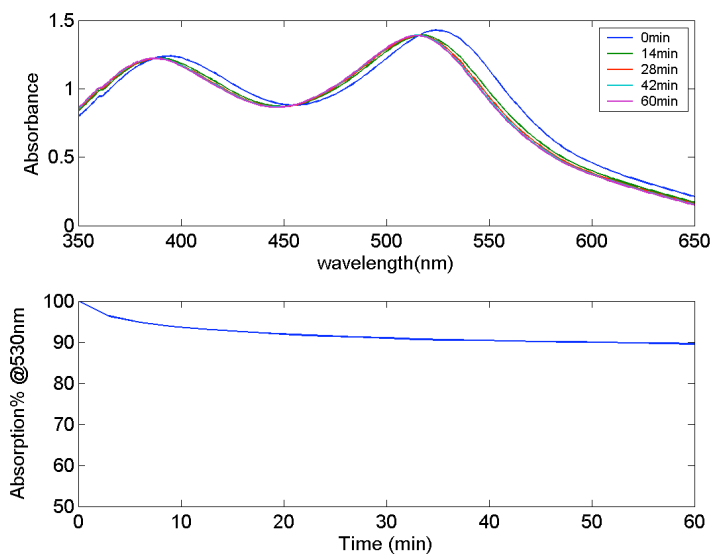


Figure 4.12. Above: representation of the absorbance spectra registered during the first 60 minutes of several sensitized films immersed in water. Below: absorbance kinetics at $\lambda=530$ nm.

After the time conditioning, the water stability of the sensitized films is guaranteed for more than 3 hours, as can be shown in Figure 4.13, wherein the aqueous stability improvement of the N719/Al₂O₃ films with and without acid treatment is compared.

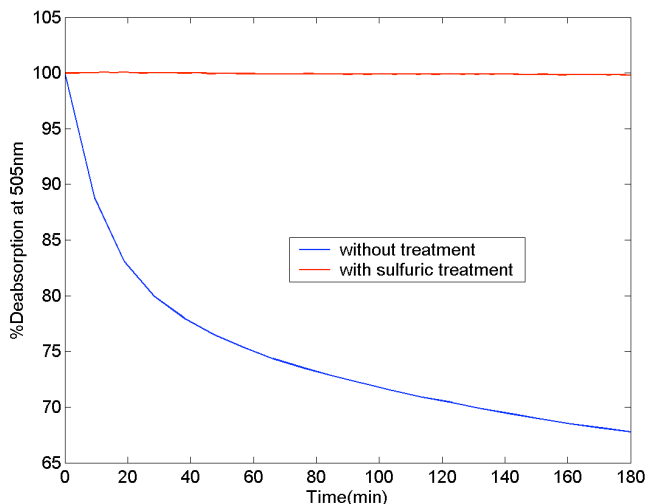


Figure 4.13. Absorbance kinetics at $\lambda_{\text{abs}}=530$ nm of N719/Al₂O₃ film treated with sulphuric acid (red line) and N719/Al₂O₃ film without acid treatment (blue line).

Furthermore, the infrared spectrum of alumina films with sulphuric acid treatment is presented in Figure 4.14. Following the correlation table of the FTIR spectrometer (Thermo Nicolet 5700), the absorption band nearest to 1150 cm⁻¹ in the treated film with acid may indicate the formation of S-O bounds on the alumina surface. We believe that the inclusion of the sulphur atoms in the alumina surface is reinforcing the chemical bonding between the dye and mesoporous Al₂O₃ film.

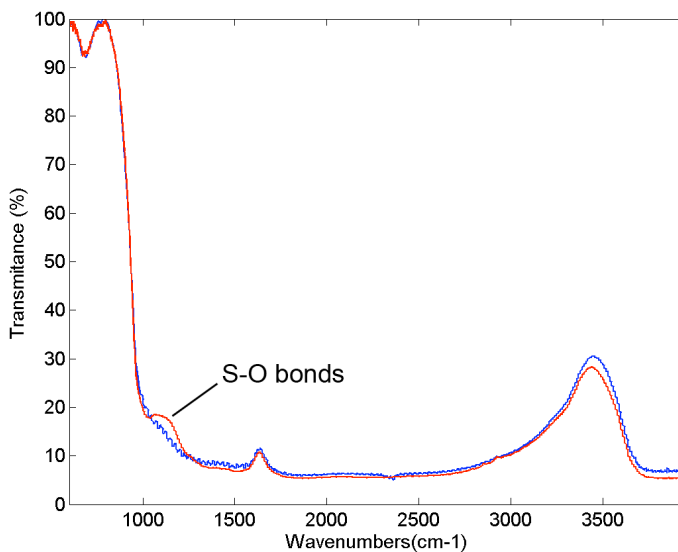


Figure 4.14. FTIR spectra of alumina films: without acid treatment (blue line) and with sulphuric treatment (red line).

4.2.5 Sensitivity and detection limits

The sensitivity towards mercury as well as the mercury detection limit is dependent of the amount of N719 anchored onto the surface of the nanoparticles. An excess of dye adsorbed onto film with high absorbance will lead a poor sensitivity, because the large amount of molecules can mask the few portion of the total reagent that interacts with mercury ions, and thus low concentrations of mercury cannot be optically detected. However, low concentrations of dye may detect mercury concentrations at low levels, but the upper limit of mercury concentration to be quantified will be lower. In this work, if mercury determination levels in

the 0-10 ppm range are desired, the best performance of the sensitive material will be achieved by a complete complexation of the reagent when mercury concentrations reach up to 10 ppm approximately. Figure 4.15 shows the absorbance spectra of mercury titration (0 -15 ppm) corresponding to N719-alumina films, wherein a complete complexation of anchored dye is observed for 15 ppm of mercury. Therefore, an initial absorbance peak at $\lambda=520$ nm around 0.3 – 0.4 (absorbance units) will produce a better excursion signal of the dyed alumina films.

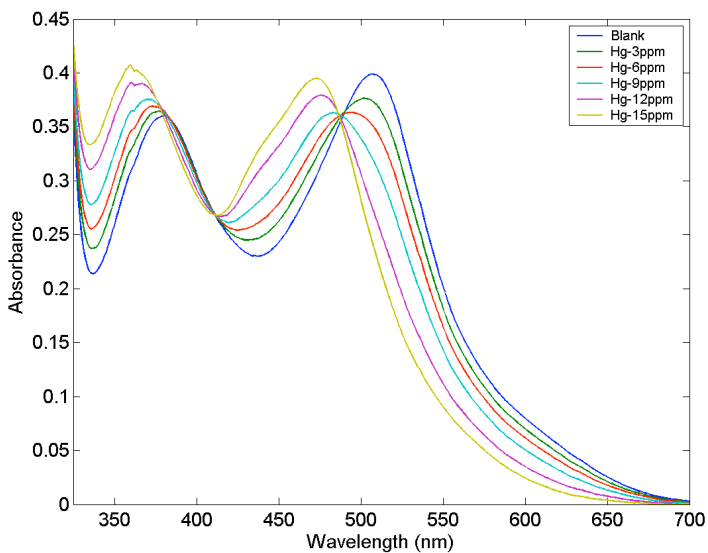


Figure 4.15. Mercury(II) titration plot of N719-Alumina film.

Varying the dipping time in the N719 film coloration procedure at a fixed temperature, the absorbance of the film can also be controlled. Therefore, in order to select the proper absorbance level of the sensitized film, several immersion times from 30 to 180 minutes for the alumina films in

N719-ethanol solution were performed at 30 °C. An increment of 0.1 absorbance units per 30 minutes was observed, see Figure 4.16. Finally, a dipping time of 90 minutes was selected so as to obtain absorbance peaks around 0.35 in absorbance units, which localizes the mercury range between 0-10 ppm approximately.

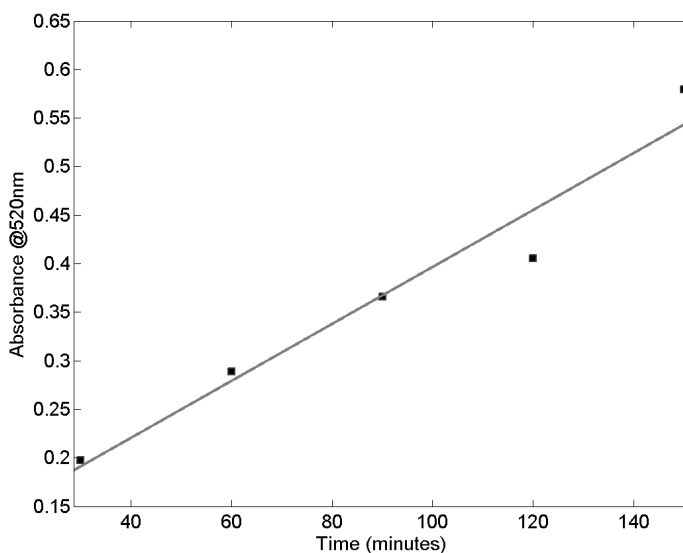


Figure 4.16. Absorbance at 520nm of alumina film vs. immersion time in N719 solution.

Therefore, the upper limit (saturation) of these films was about 15 mg L⁻¹ of mercury, meanwhile, the limit of detection, considering 3 times above the standard deviation of the blank, was around 0.5 mg L⁻¹ of mercury concentration.

4.2.6 Response time

The response time defined as the optical changes in time of the reagent N719 anchored onto alumina films due to mercury addition was tested. The experiment was performed by an Ocean Optics USB-4000 spectrophotometer where the absorbance at 530 nm was registered during the addition of 5 mg L⁻¹ of Hg²⁺ to a water solution with a total volume of 3 mL. Moreover, the response time of mercury detection in the liquid phase was measured too. Evidently, the mercury recognition in liquid phase is faster and reaches the plateau level during the first minute of the experiment (see Figure 4.17). After 15 minutes a slight variation of the measuring signal occurs due to the slow interaction of free mercury ions with N719 molecules. On the other hand, the response of N719/Al₂O₃ takes at least five minutes in order to reach a plateau. Yet after 2 minutes, the reaction continues due to the slow diffusion of mercury ions through the alumina pores until reaching a complete interaction between mercury ions and the N719 molecules. Therefore, the mercury measurements in N719/Al₂O₃ films needs to be time controlled. During our experiments we considered an interval time of measurement of 5 minutes after the addition of Hg²⁺ ions.

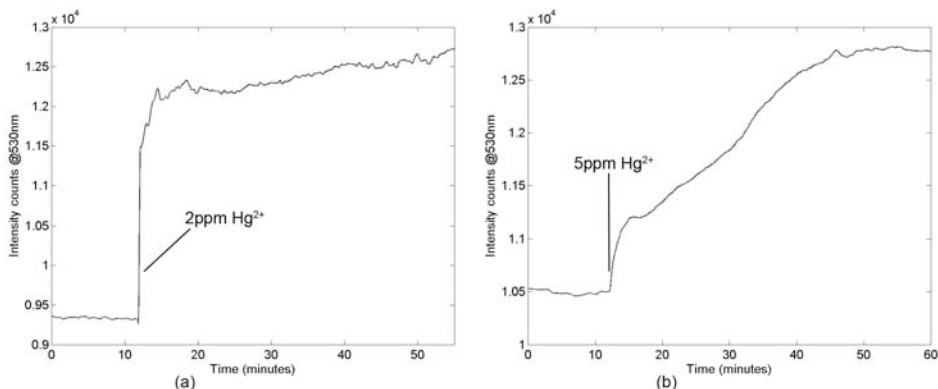


Figure 4.17. Kinetic responses at 530 nm: (a) N719 in ethanol solution upon 2 ppm of Hg^{2+} , and (b) N719/ Al_2O_3 film upon 5 ppm of Hg^{2+} .

4.2.7 Temperature influence

As detailed in Chapter 3 the temperature effect over the molecular response in liquid solution was measured and studied. The results showed no appreciable changes in the mercury determination for a wide temperature range (5 – 35 °C). Apparently, the same results for the synthesized alumina films should be expected. But if temperature increases may increase the diffusion effect of the analyte inside the mesoporous film, and thus the temperature can affect the measurement. For this reason, four N719-alumina films were prepared and mercury titrations were registered at different temperatures ranging: $T = 20^\circ\text{C}$, 30°C and 35°C . The absorbance spectrum was registered in a spectrophotometer Shimadzu UV-2401PC with a thermo stated sample holder. Figure 4.18 shows the small variations on the temperature

experiments (relative absorbance from blank) in the presence of 6 ppm of mercury.

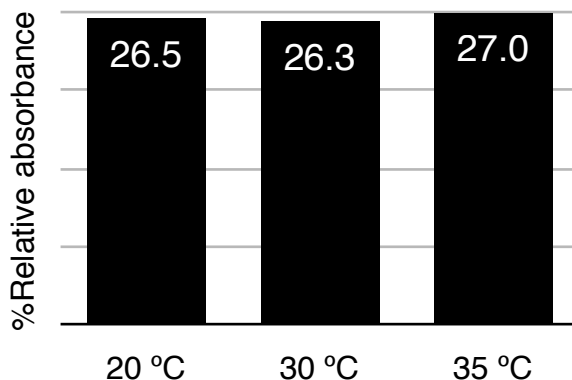


Figure 4.18. The temperature effect over the sensitized films in the presence of 6 ppm of Hg^{2+} monitoring at $\lambda = 530$ nm.

4.2.8 Reversibility

An important aspect in the field of chemical sensors, apart from sensitivity and selectivity, is the reversibility of the analyte binding, because it allows reutilizing the films for new measurements. Mercury ions form stable complexes with chlorides and acetates. Moreover, the capability of other anions to break these complexes and bind to mercury can be ordered as follows⁸:

$\text{SCN}^- \gg \text{I}^- > \text{HSO}_4^- > \text{NO}_3^- > \text{Br}^- > \text{CN}^- > \text{HSO}_3^- > \text{Cl}^- > \text{HCO}_3^- > \text{HPO}_4^{2-} > \text{Acetate} > \text{F}^-$

Thiocyanate groups have strong affinity for mercury ions. The next anion with major affinity to mercury is iodide, thus mercury could be extracted from the N719 when iodide solution reaches a certain concentration

value. The mechanism by which this process occurs is likely to involve the formation of a stable mercury-iodide complex that displaces the mercury from the thiocyanate groups⁹. In order to perform the assay a water solution of 20 mM KI was prepared. Several cycles of absorbance measurements of a N719/Al₂O₃ film immersed in a quartz cuvette were registered with a Shimadzu UV spectrophotometer. The reversibility cycles obtained are shown in Figure 4.19. Consequently, a reversibility process occurs when the mercury contaminated sensitized film is dipped in the iodide solution. In contrast, the signal progressively decreases as the number of cycles increases, being after first cycle the most notably change. This fact produces a sensitivity lost, which makes difficult the quantification process with the renewed films. Other possibility could be a regeneration process of the dye from alumina film, by desorbing the molecule in a solution at pH 10, and immersing the film in fresh N719 solution.

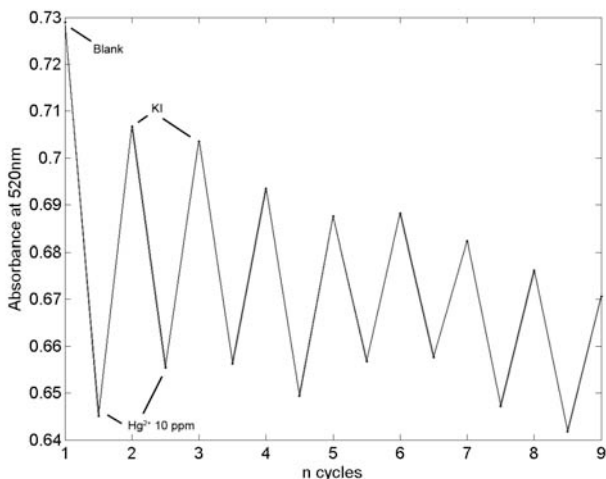


Figure 4.19. Reversible cycles for a N719/Al₂O₃ film exposed to 10 ppm mercury in an aqueous solution and after being immersed in a 1mM KI solution.

4.2.9 Durability of the sensitized Al₂O₃ films

The sensitized film stability was studied for several dyed films. The experiment was carried out as follow: (1) we measured a N719 sensitized Al₂O₃ mesoporous film immediately after being immersed in water during 45 minutes, and (2) other mesoporous sensitized films prepared at the same time were stored in a dry chamber for 24 hours, one week, and one month, respectively. It is worthy to notice that the alumina films were synthesized keeping the same conditions and controlling the temperature at T= 30 °C with a dipping time in N719 (0.3 mM) of 90 minutes. The results illustrate that a minor absorbance decrease at $\lambda= 510$ nm was observed in parallel to the storage time used in our experiment. This effect causes slight variations on the response of the sensitized films, as can be seen en Figure 4.21, wherein a decrease of the signal blank forces a minor mercury saturation limit.

As conclusion, the films can be used after storing at least one month, but the response of these films should be taken into account in the calibration procedure. Herein, for simplicity we have tested the films just after being sensitized.

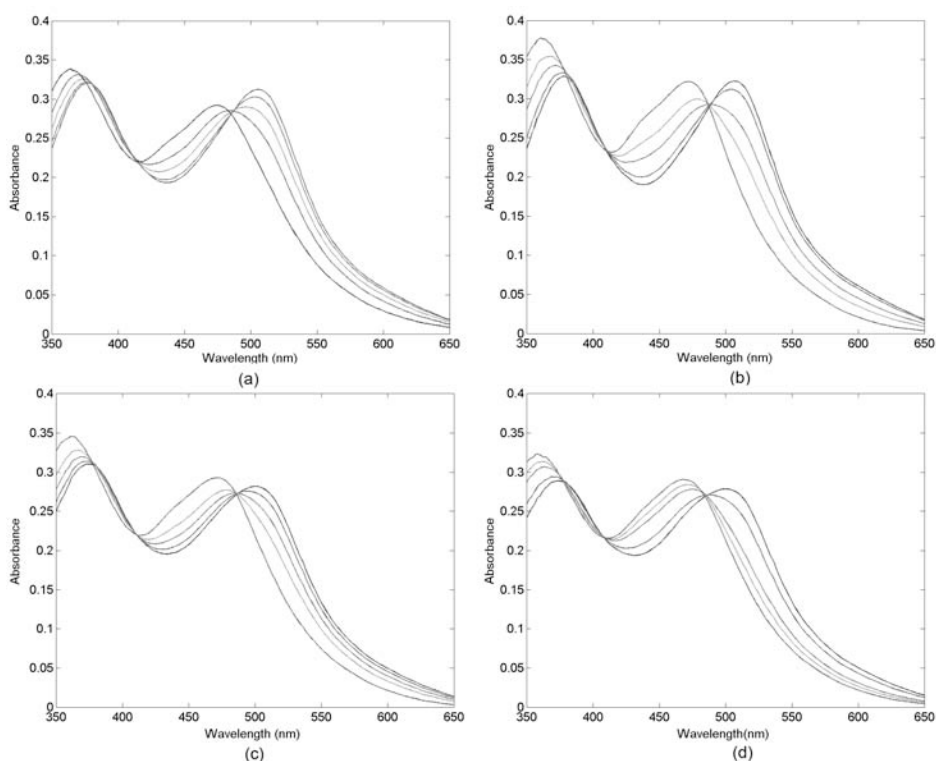


Figure 4.21. Mercury titrations (blank, 2, 4, 6, and 8 ppm of Hg^{2+} in pure water) and their absorbance spectra of N719- Al_2O_3 films: (a) immediately measured, (b) one day stored, (c) one week stored, and (d) one month stored.

4.3 N719/ Al_2O_3 Film Response Characterization

Analogously to the detailed study of the of PLS pre-treatment techniques applied for mercury recognition by N719 in solution, the calibration response of dye sensitized alumina films was performed too. Precisely, the direct PLS model prediction has been compared with PLS models

with previous statistical feature selection, and genetic algorithm pre-treatments. Other methods, such as orthogonal signal correction and wavelets, employed in Chapter 3 were discarded due to the amount of variance between measurements and the poor accuracy that their constructed models provided.

4.3.1 Data sets

The alumina films were prepared in the same manner described as in section 2.2 followed by a sulphuric acid treatment. After, an ethanol solution of N719 (0.3 mM) was utilized as stock solution for the film sensitization, after being immersed during 90 minutes at 30 °C. The absorbance measurements were registered immersing the films in a quartz cuvette with 3mL of water, wherein the optical absorbance from $\lambda=350$ nm to $\lambda=650$ nm was registered using a Shimadzu UV-1700 spectrophotometer. Each mercury titration experiment corresponds to a new N719/Al₂O₃ film after an immersion time in water of 45 minutes.

4.3.1.1 Calibration and training data sets

The response of N719/Al₂O₃ films was studied upon mercury exposure taking into account interferential effects of competitive cations. As previously described, the interferential metals considered in the multivariate calibration were: Cd²⁺, Pb²⁺, Cu²⁺, Zn²⁺. In order to minimize the diffusion effects during a large mercury titration, two titrations (0 – 5 mg L⁻¹ and 6 -10 mg L⁻¹) for each metal covered the full

range (0-10 mg L⁻¹) of mercury quantification. The titrations described in Table 4-II constitute binary concentration levels considered for metal ion mixtures. Moreover, a mercury titration in absence of interferential ions was also included in the calibration data set. An interval time of 5 minutes was considered between measurements within each mercury titration, and five repetition of each titration were performed. Three of these repetitions formed the calibration data set, and one repetition was employed for the algorithm adjustment (training data set). Finally the whole calibration data set was composed by 124 measurements with 301 spectral variables.

TABLE 4-II. Calibration and training data sets for the N719/Al₂O₃ film mercury response^a.

Titration A		Titration B	
Hg ²⁺ (mg L ⁻¹)	Other metals (mg L ⁻¹)	Hg ²⁺ (mg L ⁻¹)	Other metals (mg L ⁻¹)
0	3	0	6
1	3	6	6
2	3	7	6
3	4.5	8	6
4	4.5	9	6
5	4.5	10	6

^aFive repetitions of each titration: three for calibration data and two for training data. Moreover, the same mercury titrations were performed in absence of other metals.

4.3.1.2 Validation data set

To ensure the correct performance of the model for new samples, we carried out experiments apart from the used for the calibration. Table 4-III describes the mercury concentration values for another set of metal ions considered for validating the calibration models.

TABLE 4-III. Validation data sets for N719/Al₂O₃ films.

Set 1		Set 2	
Hg ²⁺ (mg L ⁻¹)	--	Hg ²⁺ (mg L ⁻¹)	--
0	--	0	--
4	--	3	--
8	--	6	--
10	--	9	--
Set 3		Set 4	
Hg ²⁺ (mg L ⁻¹)	Cd ²⁺ (mg L ⁻¹)	Hg ²⁺ (mg L ⁻¹)	Pb ²⁺ (mg L ⁻¹)
0	2	0	4
4	2	4	4
8	4	8	6
10	4	10	6
Set 5		Set 6	
Hg ²⁺ (mg L ⁻¹)	Cu ²⁺ (mg L ⁻¹)	Hg ²⁺ (mg L ⁻¹)	Zn ²⁺ (mg L ⁻¹)
0	4	0	4
3	4	2	4
6	6	5	7
9	6	8	7

4.3.2 Results and discussion

Following the procedure applied in Chapter 3, the parameters of the algorithms were fitted using the training data in order to achieve the lowest root mean squared error of cross validation (RMSECV). Thereafter, the capability of prediction was evaluated in terms of root mean squared error of prediction (RMSEP) considering the validation data set. In order to minimize the reproducibility variance in the film fabrication, all the measurements have been referred to the spectrum of N719/Al₂O₃ blank.

4.3.2.1 Direct PLS

Previously to the construction of the PLS model, several decimation factors were attempted in order to reduce the initial number of spectral variables (301). However, a slight deterioration in the accuracy of the multivariate linear regression model was observed as the decimation factor increases. Hence, no decimation was employed for the analysis of the molecular dye anchored onto the alumina film. In the adjustment procedure, the selection of the proper number of PLS factors was promoted by 10 iterations, wherein the predictive ability of the model is represented as a function of PLS components and the root-mean-square error for training data. The valley between 2 and 4 PLS factors shown in Figure 4.22a induces to attempt with 3 PLS factors as the best rank of the model so as to achieve good capabilities to predict new samples.

Moreover, the high error, as the number of factors increases, indicates that a great variance is present in the measurements. Additionally, the good correlation in the prediction plot for the training data set (Figure 4.22b) indicates a proper construction of the PLS model. The results for validation data considering 3 PLS factors are depicted in Figure 4.23

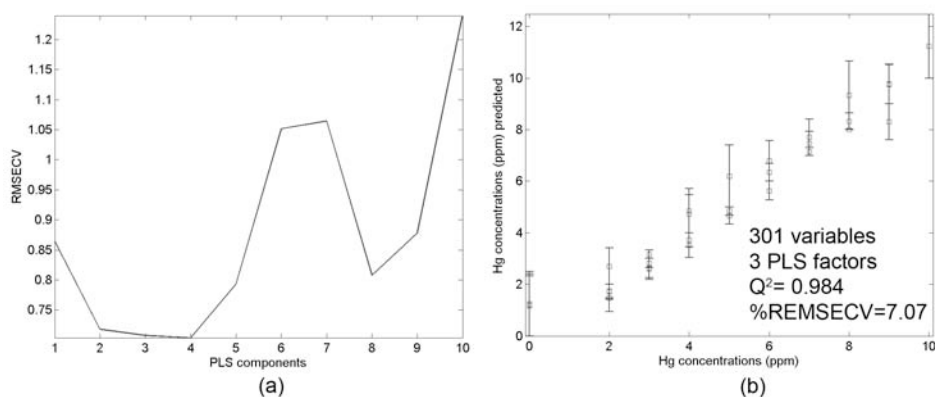


Figure 4.22. (a) Number of PLS components and their root mean squared cross validation error. (b) Prediction plot for training data considering 3 PLS factors.

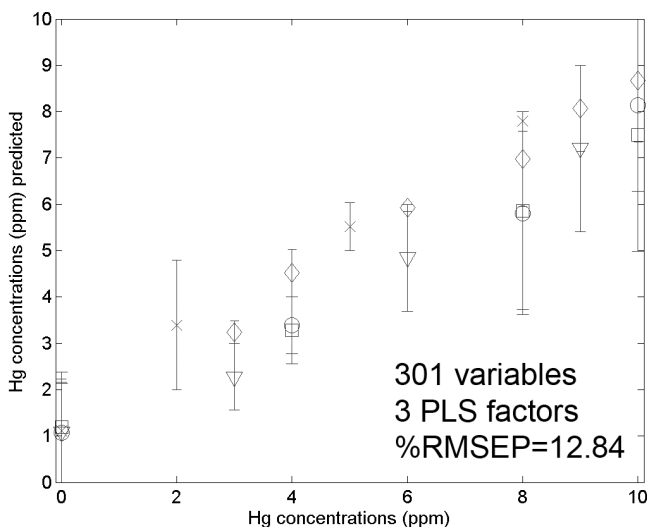


Figure 4.23. Prediction plot for validation data: (\diamond) set 1 and set 2, (\square) set 3, (\circ) set 4, (∇) set 5, and (\times) set 6.

4.3.2.2 PLS with Statistical Feature Selection

A fine adjustment of the statistical feature selection PLS model-based was achieved with a decimation factor of 5 (61 variables). Taking into account the Gaussian refinement ($\sigma=2.5$) of the selected variables (see Chapter 3), three spectral regions ($\lambda_1\sim 395$ nm, $\lambda_2\sim 445$ nm, and $\lambda_3\sim 520$ nm) were remarked as input variables for the PLS model construction (see Figure 4.24a). The optimal rank of the PLS model was 2, considering that an overfitting may appear as the number of PLS factors increases. Finally, the prediction error for validation data was rather superior to the direct PLS processing (see Figure 4.24b).

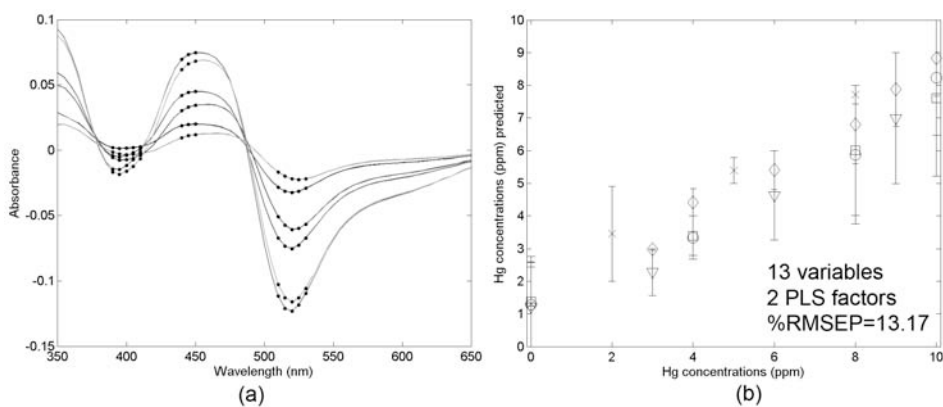


Figure 4.24. (a) Selected variables (in dot points) for the model SFS-PLS model construction, (b) prediction plot for validation data: (\diamond) set 1 and set 2, (\square) set 3, (\circ) set 4, (∇) set 5, and (\times) set 6.

4.3.2.3 PLS with Genetic Algorithm

The selection of spectral variables have been also explored with genetic algorithm in order to investigate the prediction error of the constructed PLS model. First, a decimation factor of 3 was applied providing 15 variables, which it made easier the algorithm adjustment. Due to the fact that N719- Al_2O_3 films have similar spectral response to solution-based samples, the intrinsic parameters used (number of chromosomes, variables per chromosome, etc.) are the same that employed in Chapter 3. Following that, the heuristic search provided 15 variables (Figure 4.25a), in which the PLS model was constructed. As the same case that statistical feature selection, the error of prediction for validation data is superior to the direct PLS, see Figure 4.25b.

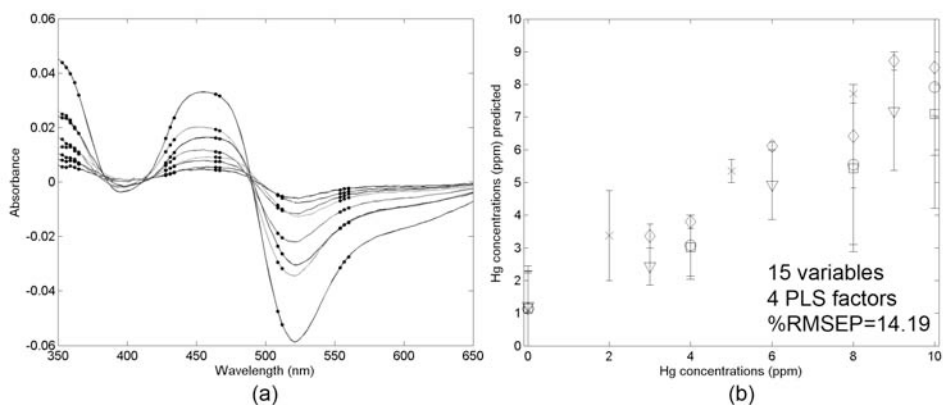


Figure 4.25. (a) Selected variables (in dot points) by genetic algorithm, (b) prediction plot of the model corresponding to validation data: (\diamond) set 1 and set 2, (\square) set 3, (\circ) set 4, (∇) set 5, and (\times) set 6.

Table 4-IV shows the results of the multivariate calibration applied to N719-Al₂O₃ films. In this case, the minor error of prediction was achieved with direct PLS, but SFS-PLS provided a comparable result with a great reduction of variables too. As it was expected the error of prediction increases from the experiment of dye in liquid phase, because herein the error in the reproducibility of the films has a great effect. In this situation, the direct PLS prediction provides the model that better fits the sample predictions. Overall, the response of the dyed alumina matrix, tested in the presence of other metal ions, has shown good correlation with mercury concentration, and it can be concluded that the Al₂O₃ nanoparticles do not disturb the mercury measurements.

TABLE 4-IV. Comparison of the multivariate calibration techniques applied to N719/Al₂O₃ films for the mercury determination.

	Variables	PLS factors	Q ²	%RMSECV	%RMSEP
Direct PLS	301	3	0.984	7.07	12.84
SFS	13	2	0.983	7.32	13.17
GA	15	4	0.983	7.31	14.19

4.4 References

- (1) Nazeeruddin, M. K.; Di Censo, D.; Humphry-Baker, R.; Gratzel, M. *Advanced Functional Materials* **2006**, *16*, 189-194.
- (2) Rottman, C.; Ottolenghi, M.; Zusman, R.; Lev, O.; Smith, M.; Gong, G.; Kagan, M. L.; Avnir, D. *Materials Letters* **1992**, *13*, 293-298.
- (3) Zhi-xue, H.; Song-yuan, D.; Kong-jia, W. *Plasma Science & Technology* **2002**, *4*, 1475-1480.
- (4) Vijay, A.; Mills, G.; Metiu, H. *Journal of Chemical Physics* **2002**, *117*, 4509-4516.
- (5) Park, J. H.; Lee, M. K.; Rhee, C. K.; Kim, W. W. *Materials Science & Engineering, A: Structural Materials: Properties, Microstructure and Processing* **2004**, *A375-A377*, 1263-1268.
- (6) Tok, A. I. Y.; Boey, F. Y. C.; Zhao, X. L. *Journal of Materials Processing Technology* **2006**, *178*, 270-273.
- (7) Campbell, W. M.; Burrell, A. K.; Officer, D. L.; Jolley, K. W. *Coordination Chemistry Reviews* **2004**, *248*, 1363-1379.
- (8) Dedkova, V. P.; Shvoeva, O. P.; Savvin, S. B. *Journal of Analytical Chemistry (Translation of Zhurnal Analiticheskoi Khimii)* **2003**, *58*, 230-235.
- (9) Coronado, E.; Galan-Mascaros, J. R.; Marti-Gastaldo, C.; Palomares, E.; Durrant, J. R.; Vilar, R.; Gratzel, M.; Nazeeruddin, M. K. *Journal of the American Chemical Society* **2005**, *127*, 12351-12356.

5 Development Of The Optical Fiber Mercury Probe

CONTENTS

- 5. 1 Sensor operating principle
- 5. 2 Optical fiber probe fabrication
- 5. 3 Measurement set up
- 5. 4 Results and discussion
- 5. 5 References

5.1 Sensor Operating Principle

A common feature of the optical fibers used in the chemical sensor field is its ability to transmit optical signals over long distances with minimal power losses, avoiding possible electrical interferences and, moreover, a high degree of integration. The concept is based on the optical changes of a reagent that can be attached onto the fiber optic whereby the light is transmitted. In particular, the design is based on the N719 indicator supported by an alumina cladding that surrounds the silica core of the optical fiber. The light interacts onto the sensing material likewise an evanescent field, which is modulated by the absorbance changes of N719 when mercury is present.

It is worthy of consideration that the sensing behaviour of a functionalized optical waveguide is not always trivial, and in some cases, the results are not easy to discern. There are many theoretic studies of evanescent optical fibers that are focused on a particular research case. For example, Stewart and Culshaw described some results that enable the design of sensors with optimum sensitivity¹. Their analytical expressions are based on a ray optics approach whereby can be derived for planar and multimode fiber sensors. Veldhuis² et al. expose an analytical study about the sensitivity enhancement in evanescent optical waveguide sensors. They found an optimum waveguide thickness for the maximum

sensitivity to changes in the cover for an otherwise fixed set of waveguide parameters.

However, many of the theoretical studies are approximations that in certain cases may assist in the optode design parameters. After all, the final results are dependent on several factors in which the constrictions of the chemical reagent and the optical properties of the immobilisation support are decisive for the proper performance of the sensor.

The probe configuration selected in this work is based on the evanescent wave effect created in a modified cladding of the optical fiber. The selection of optical fiber as a waveguide element is based on its facility to couple to light sources and photodetectors, instead planar optical microsensors that suffer from injecting light losses into the waveguide². Herein, the sensitive material is formed by N719-Al₂O₃ sensitised nanocrystalline particles. A small section of the passive cladding of the optical fiber is removed and replaced by the chromogenic film, as can be seen in Figure 5.1. The propagation of the light is carried out through a multimode optical fiber. A mirror placed at the end of the tip provides the return path to the photo-detector. Therefore, the interrogation of the tip is performed by the reflected light intensity that is modulated by the absorbance changes of the indicator. In this manner, a chromophore within the evanescent field attenuates the power of transmitted light at its absorbing wavelengths.

The advantage of the evanescent wave technique is a major interaction of the light probe with the sensitive material that surrounds part of the core, instead of a direct measurement, wherein the interaction only occurs in the area projected by the light beam. In liquid measurements, this fact is not very relevant because the optical path length takes place along the cuvette length, normally 1 cm. Nevertheless, in solid-state phase the optical path of the thin film is reduced to a few microns, and thus the sensitivity dramatically decreases. Theoretically, increasing the sensitive cladding length along the optical core, higher sensitivity will be achieved. However, the power losses of the propagated light are directly proportional to the increase of the modified cladding length. In this sense, power attenuation of the light transmitted through a lossless core and a treated cladding is³

$$P_z = P_0 \cdot e^{-\gamma L} \quad (5.1)$$

where L is the distance of the modified cladding along the fiber longitudinal axis z , and γ is the evanescent absorption coefficient that is proportionally related with the absorption coefficient α of the chromophore and the fraction of optical power outside the fiber core. Other advantage is that the small penetration depth of the evanescent field, of the order of one micron, results in a measurement technique which is found to be insensitive to light-scattering in those cases when significant concentrations of suspended particles are present in the liquid sample⁴.

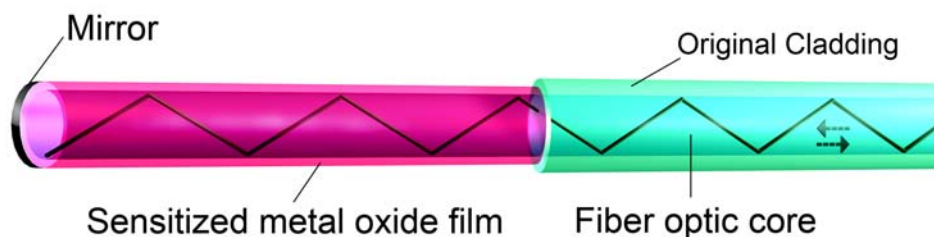


Figure 5.1. Overview of the optical fiber probe configuration for Hg^{2+} ions.

Particularly, when Hg^{2+} ions react with the sensitive cladding an absorbance change occurs modifying the transmission properties of the optical fiber. Mainly, these variations have a great dependence with the refractive index of the sensitized material given by

$$n_{fc} = n_{real} + ik \quad (5.2)$$

being n_{fc} the complex refractive index of the functionalized clad, n_{real} the real part, and k complex part related to the absorbance of the material that keeps a constant modulus during light propagation⁵. Basically, the refractive index of the modified cladding can be derived in two operating modes⁶:

- **Evanescent mode** usually appears when the refractive index of the core is greater than the functionalized cladding. A change in the refractive index of the sensitized cladding will result in a change of the intensity of the light transmitted through the optical fiber.

► **Leaky mode** is more appreciated when the refractive index of the modified cladding is greater than the core. In this case, part of the incident light radiates from the core by refracting through the functionalized coat. Furthermore, if the modified cladding is very thin (less than 1 μm), the outer medium (air or water) acts as a second layer of the cladding, and a total internal reflection can take place if the external media has lower refraction index than the modified cladding. In this case some light is reflected back into the core and the functionalised region may act as a waveguide. The resulting optical intensity is modulated by the absorption of a portion of light, and the evanescent field may be also present in the modified cladding. Hence, the critical angle must be calculated using the following notation⁷:

$$\theta_c = \cos^{-1}(n_{\text{core}}/n_{\text{fc}}) = \sin^{-1}(1-(n_{\text{core}}/n_{\text{fc}})^2)^{1/2} \quad (5.3)$$

being the depth of penetration of the electric field described as:

$$d_p = \frac{\lambda}{2\pi\sqrt{\cos^2 \theta - (n_{\text{core}}/n_{\text{fc}})^2}} \quad (5.4)$$

The two situations can be illustrated as shown in Figure 5.2.

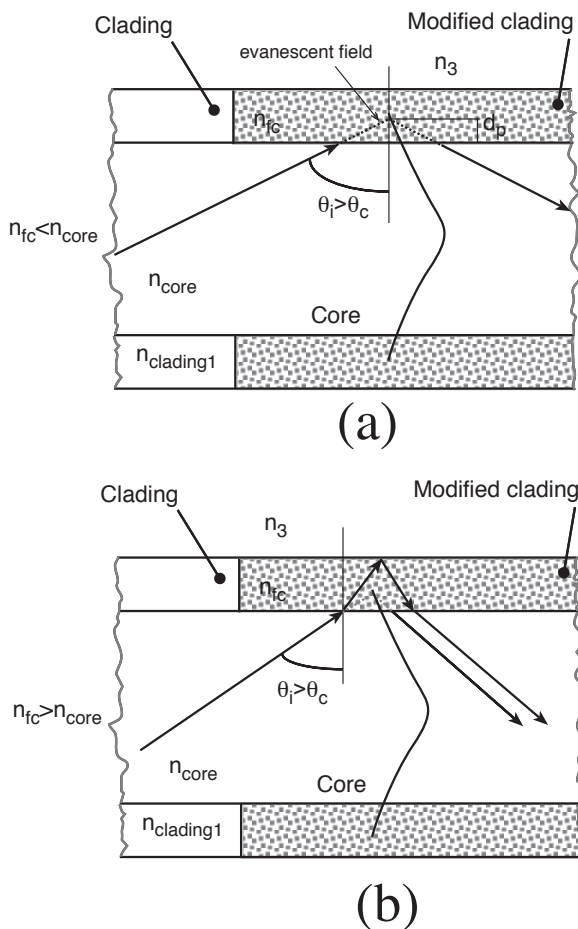


Figure 5.2. Modes of operation of an optical fiber with a modified clad. a) When the refractive index of the modified cladding (n_{fc}) is minor than n_{core} , the total internal reflexion occurs for optic rays with an incidence angle θ_i greater than the critical angle θ_c , and, therefore, an evanescent field appears. b) If n_{fc} is greater than n_{core} , the interaction of the light at the interface of sensitive material/core is governed by a leaky mode. A fraction of the light is refracted on the modified cladding indeed for $\theta_i > \theta_c$ and the rest is reflected allowing also an evanescent field.

Following with our particular case, considering a standard optical fiber with a silica core with refractive index of 1.4, and water as external medium with $n_w = 1.33$, the mode of operation of the system is controlled by the refractive index of the alumina cladding. Studies⁸ on the optical properties of aluminium oxide reveal a refractive index of 1.7 for γ - Al_2O_3 . Herein, we consider that bohemite phase has similar optical

properties than gamma phase because the crystallization conditions are almost identical. Hence, the final refractive index of the functionalized cladding will be higher than 1.5, with a great component of variation in its imaginary part promoted by the absorbance changes of the N719 when mercury is present. This situation appoints to the leaky mode operation whereby the N719-Al₂O₃ cladding absorbance changes, modulate the transmitted light through the optical fiber. Numerically, applying the equation 5.4 and considering $n_{jc}=1.7$ the distance that the light travels across the alumina clad for a wavelength of 700 nm reaches 0.7 μm .

As mentioned above, we have found several theoretical studies focussed on optical fiber sensors, but in general considering only the evanescent mode. However, there is a lack of references that expose a theoretical study for optical fiber sensors based on the leaky mode. From the explanation afforded by Yuan and El-Sharif⁹, we can extract some guidelines for the operation principle of the mercury probe.

As the alumina cladding has higher refractive index than the core, total internal condition does not satisfy in this region. Part of the incident light at the alumina/core interface is refracted and the rest is reflected. The reflection depends on the refractive indices of the core and alumina cladding as well as the light incident angle. The light propagated inside the chromogenic cladding is partially absorbed and the rest refracts back into the core. The total energy losses follow equation 5.1. Moreover, another fraction of light is totally reflected at the core/alumina cladding

interface generating an evanescent field, which penetrates into the modified cladding. Therefore, the resultant optical signal is modulated by both phenomena.

A thin layer of alumina cladding (around 1 micrometer) will facilitate the back refraction into the core of the reflected light at the alumina/water interface. Moreover, some water interferences, such as refractive index or absorbance changes, may cause optical variations in the propagation mode across the N719-alumina clad. Consequently, a thicker coating will result in better performance and reduce the external interferences¹⁰. For this reason, we decided to work with a thicker alumina clad to reduce external interferences and improve the mechanical properties of the film. The details of the optical fiber probe fabrication for mercury sensing is given below.

5.2 Optical Fiber Probe Fabrication

The probe head was fabricated at the laboratory of Communications Department of the Public University of Navarra in a similar way to the one reported by J. Moreno et al.¹¹. The construction is simple and low cost, which we believe that are important advantages. A hard polymer-clad multimode optical fiber with silica core (200 μm , $n_{\text{core}}=1.457$) from Thorlabs was employed. This fiber has a polymer-clad with a thickness of 25 μm (TEQS, $n_{\text{clad}}= 1.404$) that can be removed using a non-toxic

solvent such as acetone. Later, the polymer claddings were stripped from the fibers in lengths of 6 cm. The same alumina paste prepared and characterised in Chapter 4 was utilised, but diluted with ethanol (0.6 ml ethanol for each 0.5 grams of alumina paste) in order to achieve the proper viscosity for the coating process. The paste was deposited onto the fiber core by the *dip-coating* technique, where the velocity down/up is controlled by a robot to ensure reproducibility. Depending on the viscosity of the paste, the velocity must be varied in order to obtain the desired thickness. The film thickness was proportionally controlled by the robot, wherein thinner films are achieved with slow velocities. Several tips were coated in order to find the parameters that provide a film thicker than 1 μm . Curing the fiber at 100 °C during 20 minutes was carried out to ensure the complete evaporation of solvent in the paste. After that, the fiber was annealed at 450 °C during 90 minutes to achieve the solidification of the paste. Because of the fact that the original cladding of the optical fiber does not resist high temperatures, the alumina coating was placed in a piece of the de-cladded optical core, and, the resulting tip was continuously welded with an original optical fiber piece of 15 cm. However, the ideal solution would consist in a low temperature annealing, as this procedure could afford the coating process without the fusion requirement. We tried to anneal the alumina coating at $T=125$ °C during three days, but the resulting film was too soft and it brook down when it was immersed in water. An alternative way may be possible by employing a hard silica-clad optical fiber, which is resistant

to high temperatures. In this case, a common etching process consists of soaking the optical fiber in a HF solution (hydrofluoric acid) which removes the glass cladding of the optical fiber. However, this method produces an irregular core surface, which reduces the reproducibility of the fabricated sensors¹³. Therefore, we decided to weld the piece of silica core coated with alumina with an origin optical fiber by fusion splicing, which is the most permanent and the method with lower losses for connecting optical fibers¹². We used the Ericsson FSU-905 fusion machine, which can be fully manual controlled. Stepper motors precisely align the two fibers, and a CCD camera assists the position adjustment of the two optical fiber extremes. Finally, a high arc voltage about 7000 volts is responsible of the welding.

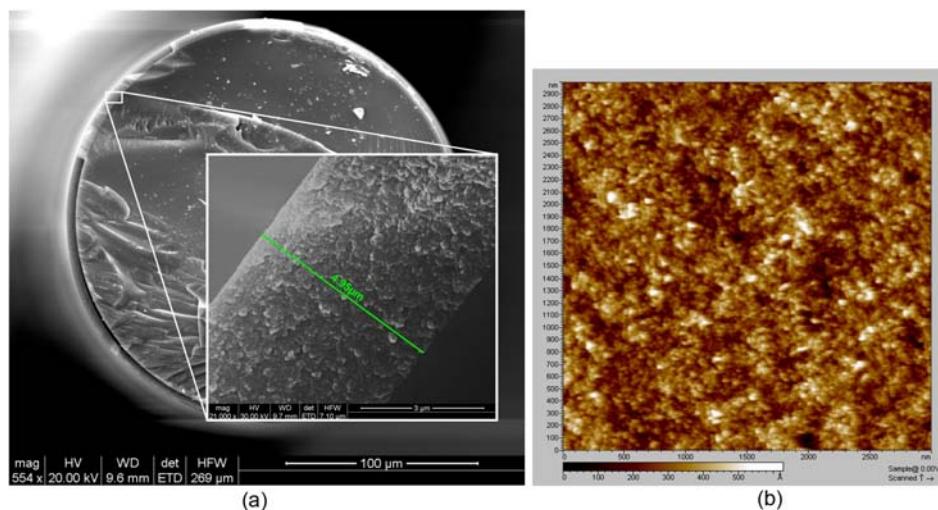


Figure 5.3. a) Cross-section of the optical fiber probe tip, b) atomic force microscope image of alumina surface deposited onto silica core of the optical fiber.

At least, sixty optodes were fabricated in order to characterise the sensing properties of the optical fiber probe. The prepared fibers showed a transparent and homogeneous alumina cladding at the sensitive tip. The cross-sectional view of the alumina coated onto the optical fiber is shown in Figure 5.3a, wherein the scanning electron microscope image reveals a film thickness of around 5 μm , which is much greater than the evanescent path (0.7 μm). Moreover, the mesoporous morphology of the *in-situ* deposited alumina cladding can be examined by Atomic Force Microscope (AFM) spectroscopy, as shown in Figure 5.3b.

Once the fibers were obtained, in order to improve the water stability of the film explained in Chapter 4, each optical fibers were immersed by the alumina cladding size in a sulphuric acid solution during 20 minutes. Thereafter, the fibers were dried at 125 $^{\circ}\text{C}$ for three hours. Finally, the N719 indicator was adsorbed by immersing the optical fiber tips in a N719 (0.3 mM) ethanol solution. The excess of core without alumina clad was cut and the mirror was positioned using silver paint. As stated above, the optical losses increased, as the length of the surrounding clad was larger. Thus, we estimated that the length of the sensitive element along the fiber core should be 2 cm. Figure 5.4 shows the resulted optical fiber probe for mercury detection. Note that the molecule is homogeneously adsorbed onto the alumina coating, meanwhile, the transparent side corresponds to the welded optical fiber piece with its original cladding. The high integration level of the detector tip constitutes one of the challenges achieved by this research work.

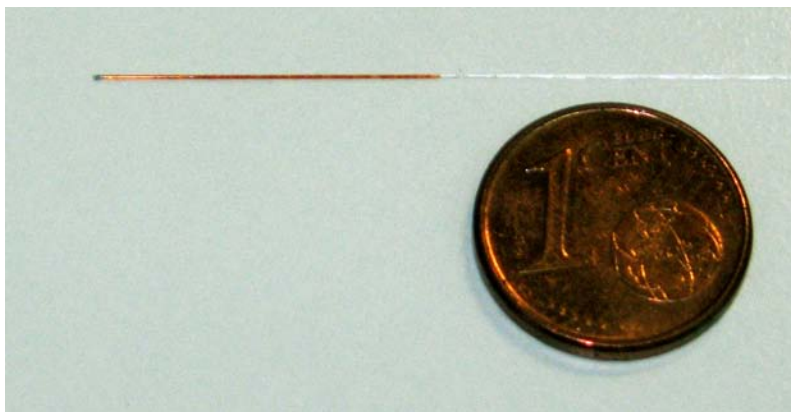


Figure 5.4. Aspect of the mercury optical fiber probe.

5.3 Measurement Set Up

The spectroscopic instrumentation consisted on a DH-2000-BAL light source and an USB-4000 spectrophotometer both of them purchased from Ocean Optics. The light was supplied by a halogen lamp and focused onto one branch of a bifurcated optical fiber, and the other branch is connected to the miniaturised spectrophotometer. An SMA ('SubMiniature A') connector adapter physically attached the experimental optical fiber to common branch of the bifurcated fiber. The multimode operation of the optical fiber makes suitable a readout process in real time. The sensing surface localized at the tip of the optical fiber was immersed in an aqueous solution, wherein the mercury titrations were measured. The reflected light was led through the other arm of the bifurcated system to the spectrophotometer. In Figure 5.5 we depicted the

components involved in the measurement process and in Figure 5.6 we illustrate the experimental setup for mercury determination. In order to minimise the influence of ambient light, the measurements were taken by covering the sample holder with a black box.

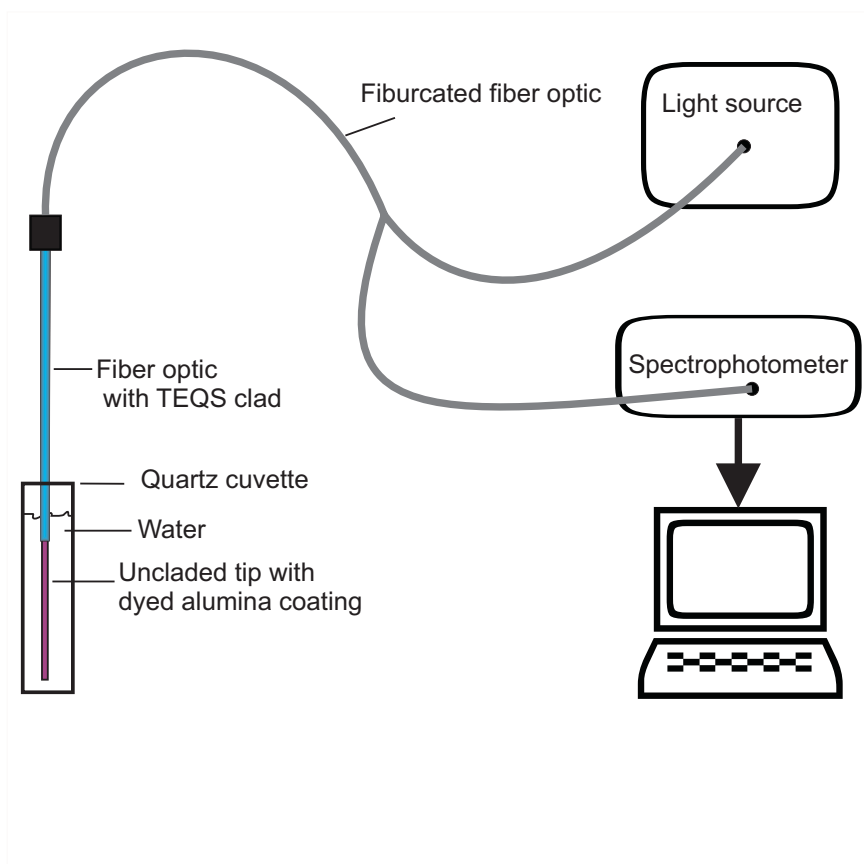


Figure 5.5. Scheme of the optical fiber setup for mercury determination.

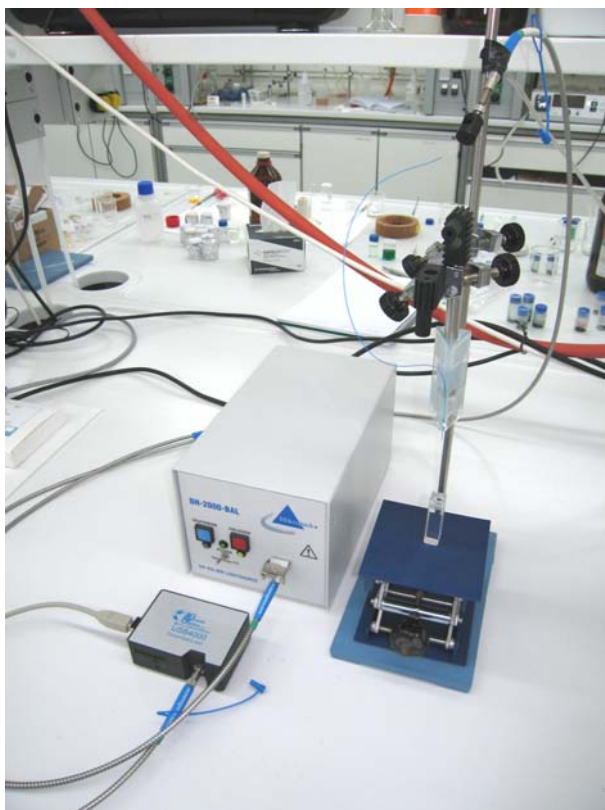


Figure 5.6. Experimental setup of the optode for mercury measurements. The optical fiber with the sensitive head is connected to a bifurcated optical fiber: one branch transmits the light from the DH-2000 lamp, and the returned modulated light travels through the other branch.

5.4 Results And Discussion

5.4.1 Working conditions

The results presented in this section are the consequence of many measurements carried out to find the proper operating conditions of the optode and to discern the nature of the optical behaviour of the transduction mechanism. Herein, the study is focused on the spectral

range of the molecular probe that shows the greater change when mercury is present. This region is $\lambda=450-700$ nm, which can be studied with our halogen lamp. At the beginning, several measurements were performed in order to check the experimental system. In this way, the spectrum of the lamp was registered by two different modes. One mode correspond to an original optical fiber with a silver mirror at the end (Figure 5.7a), and the other spectrum scope was achieved with a modified fiber optic with the alumina clad but without chromophore and immersed in water (Figure 5.7b). By comparing the amplitudes in both cases, the attenuation of the modified fiber along the spectral range $\lambda=450-750$ nm is -14.8 ± 0.09 dB. Moreover, we experimented that the attenuation caused by the immersion of the probe in water was -1.05 ± 0.7 dB. Therefore, it can be considered that the major optical losses are caused by the refraction of a considerably part of the light through the alumina cladding (radiative mode) plus the attenuation introduced by the welding region.

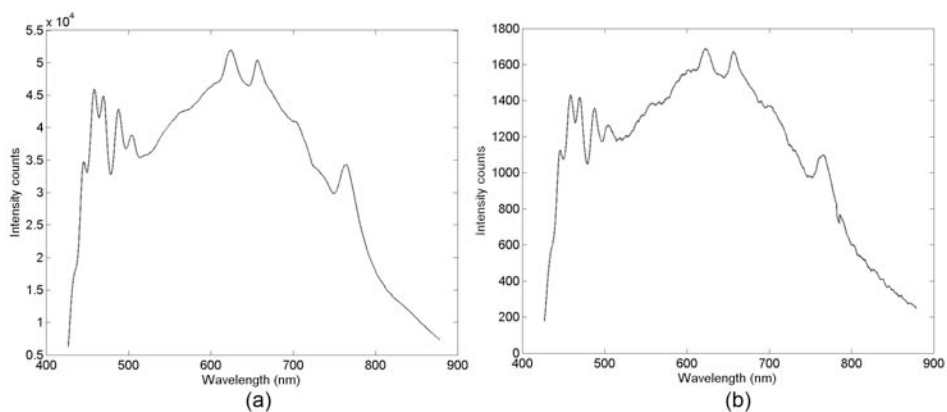


Figure 5.7. Reflectance spectrum of: a) original fiber optic with silver mirror at the end, b) fiber optic with alumina cladding and silver mirror at the end immersed in water.

Moreover the possible effects of the mercury ions over the refractive index of water were tested too. A blank was carried out using an optical fiber with uncoloured alumina cladding was immersed in water. Once the optical signal is stabilized (after 5 minutes if no dye is present) the reflected intensity of this blank is registered and 5 mg L⁻¹ of Hg²⁺ was added. The non-variations on the registered data concluded that no spectral changes were introduced by the addition of mercury ions to water, and thus the measurement is not under the water refraction index change condition.

On the other hand, the optimal dye concentration adsorbed on the alumina clad of the optode was tested and its influence on the sensitivity was observed too. Alumina-coated fibers were immersed in the N719-ethanol solution (0.3 mM) at 30 °C at different interval times: 5, 30, 60 and 90 minutes. Mercury titrations were performed in order to determine the sensitisation conditions. Similarly to the alumina mesoporous films previously described at Chapter 4, in order to obtain a stable response, each optode was immersed in pure water during 45 minutes before the measurement process. Hence, any excess of the adsorbed molecular indicator in the sensitive medium was removed. By observing the spectral mercury titrations of the optode with a sensitised time of 90 minutes, it appears several spectral features at $\lambda=800$ nm that should be constant, see the spectral scope represented in Figure 5.8a. This behaviour suggests that an excess of dye is present onto the alumina

cladding and a de-sorption process occurred, which makes difficult the signal stabilization.

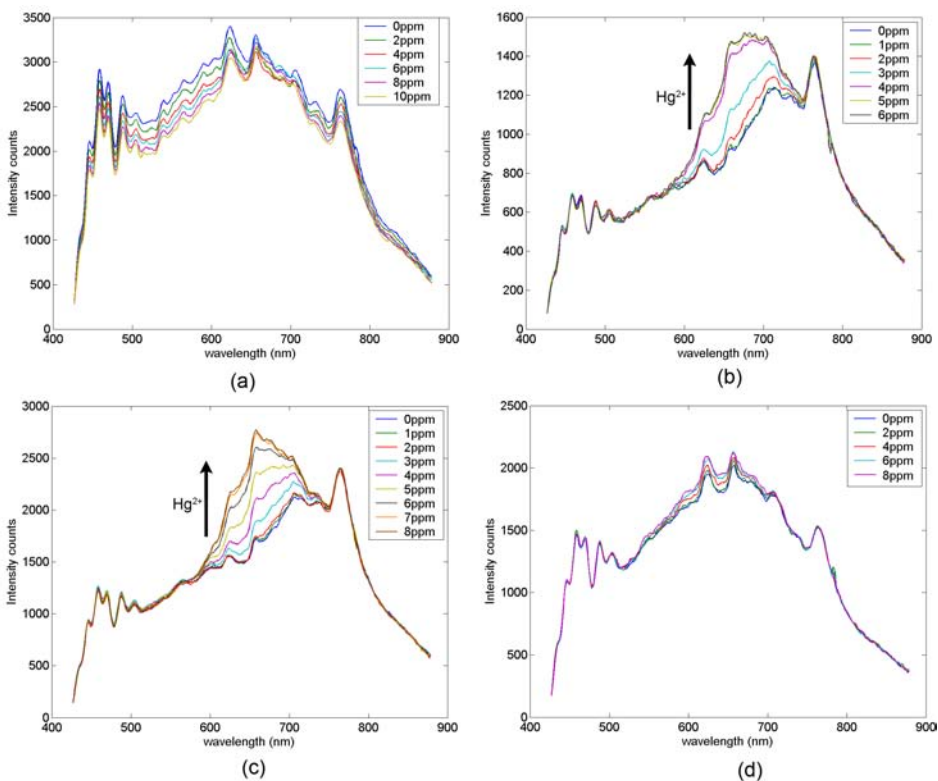


Figure 5.8. Intensity counts of the optical fiber probe with different sensitization times in N719 ethanol solution: a) 90 minutes, b) 60 minutes, c) 30 minutes, and d) 5 minutes. The reflected light is registered after a conditioning time of 45 minutes whereby the optodes has been immersed in buffered water solution at ph 7. After that, titrations were performed by adding Hg^{2+} drops with an interval time between measurements of five minutes.

Sensitisation times of 60 and 30 minutes provided a clearly spectral signal correlated with mercury additions, being the optode slightly more stable in the later case as illustrated in Figure 5.8b and Figure 5.8c

respectively. Whereas, low immersion times produce poor spectral changes because the poor coloration of the alumina cladding hardly absorbs the corresponding fraction of light that emerges from the core to the dyed alumina cladding, see Figure 5.8d. Note the attenuation on the spectral region from the 450 to 720 nm of the blank when the proper concentration of the reagent is present onto the alumina cladding (see Figure 5.8b and Figure 5.8c). Meanwhile, if the alumina cladding of the optode has an excess or insufficient dye concentration, the final spectrum is remarkable comparable to the original spectrum of the lamp. Thus, the proper working conditions of the optode are also controlled by the dye concentration adsorbed onto the alumina cladding. Additionally, we must to consider a variance in the light intensity counts, which is dependant of the fabrication process for each optical fiber probe. Representing the scope of the spectral signal from Figure 5.8c in terms of absolute absorbance, as can be seen in Figure 5.9, the maximum peak of the observed spectral changes are localised at $\lambda \sim 680$ nm. This result notably differs from mercury titrations performed either in liquid or alumina film measurements with the N719, wherein the maximum peak was localised around $\lambda = 530$ nm.

In order to check the origin of this mismatch, the direct absorbance measurements of mercury titrations with N719-ethanol solution were carried out. In this experiment, an adapted cuvette holder for optical fiber measurements connected between the lamp and the spectrophotometer was employed.

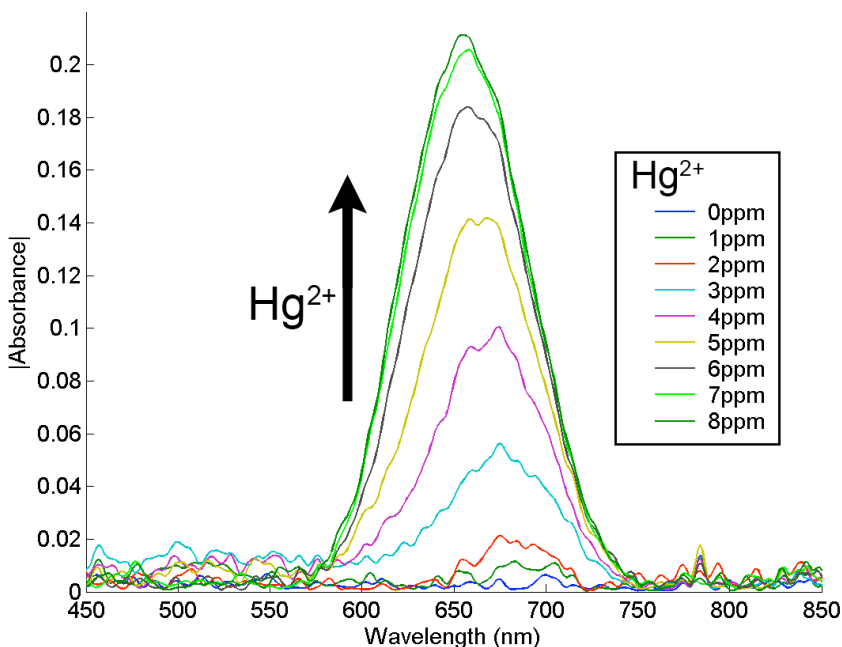


Figure 5.9. Absolute spectral absorbance of Hg^{2+} titrations corresponding to an optical alumina cladding-based fiber with a sensitization time in N719 ethanolic solution of 30 minutes. The absorbance is related to the blank of the optode immersed in pure water.

As it was expected, from Figure 5.10a, it can be observed that spectral changes, induced by the mercury addition, appear in a wide range from $\lambda=450$ nm to 750 nm, with a maximum peak localised at $\lambda=530$ nm. After all, regarding Figure 5.10b represents the absolute value of absorbance. Therefore, the observed spectral absorbance changes are in agreement with previous measurements realised by using conventional equipment, and thus the optical fiber measurement system is correctly working.

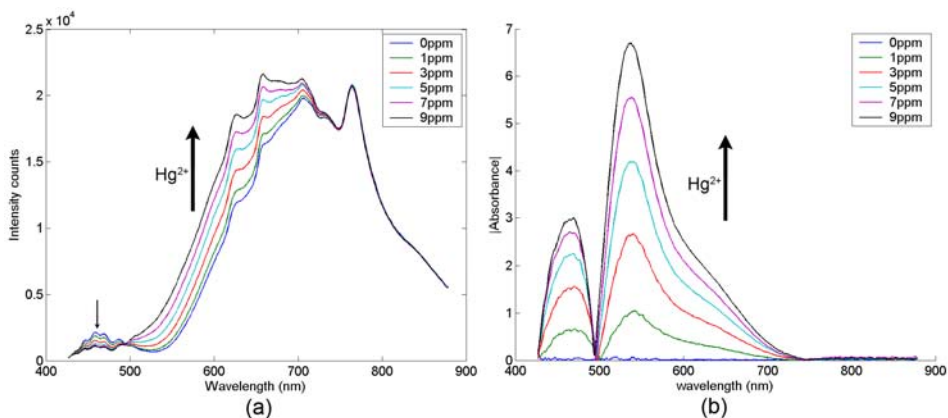


Figure 5.10. Mercury titrations in N719-ethanol liquid measurements registered by the optical fiber system using a cuvette holder: a) intensity counts, and b) its absolute absorbance representation.

Moreover, one of the aspects that may influence the spectral shift of the fabricated optode can be extracted by observing the light transmitted by the direct measurement of the reagent (Figure 5.10a). As can be seen, a great attenuation of light is produced in the region of $\lambda=430-550$ nm and it is progressively less remarked as the wavelength increases. Obviously, this effect is inherent to the N719 transmittance because this is the spectral region wherein the more dye absorbs. In contrast, this effect may be responsible of the major attenuation of this part of spectrum light once this is refracted through the alumina cladding. Therefore, the dye may attenuate the spectral region of the around $\lambda=530$ nm in which the the sensitivity is larger. This fact reduces the features of the optode in order to improve the sensibility in solid state, but anyway a high level of integration is achieved with this optode configuration. It would be expected that augmenting the power of the light source it could observe

changes in the $\lambda \sim 530$ nm region, but an excess of light may produce photodegradation problem in the molecule.

5.2 Reproducibility and multivariate calibration

The reproducibility is a lack of most of this kind of optodes. According to Alabbas¹⁴ et al. sometimes the major source of non-uniformity of the response is generated by the sensor construction rather than sensor operation. We tested the mercury response with diverse optodes. Figure 5.11 shows the response in both intensity counts and absolute spectral absorbance corresponding to mercury titrations of three optodes with the same fabrication conditions: alumina cladding length of 2 cm, thick of 5 μm , and a N719 sensitisation time of 30 minutes at 30°C. The optodes were immersed in the cuvette with 3 ml of HEPES water solution at pH 7 for a conditioning time of 45 minutes. Thereafter the mercury drops were added and the optical reflectance intensity were registered. The amplitude of the optical signal varies significantly from each optode. At a first time, this fact may suppose an inconvenient so as to predict mercury levels at a fixed wavelength. But observing the spectral intensity of the optode response, some useful information may be extracted from comparing different parts of the spectrum. This can be a good challenge to be solved by multivariate linear regression, wherein spectral synergies can contribute to find linear relationships for predictions of mercury levels.

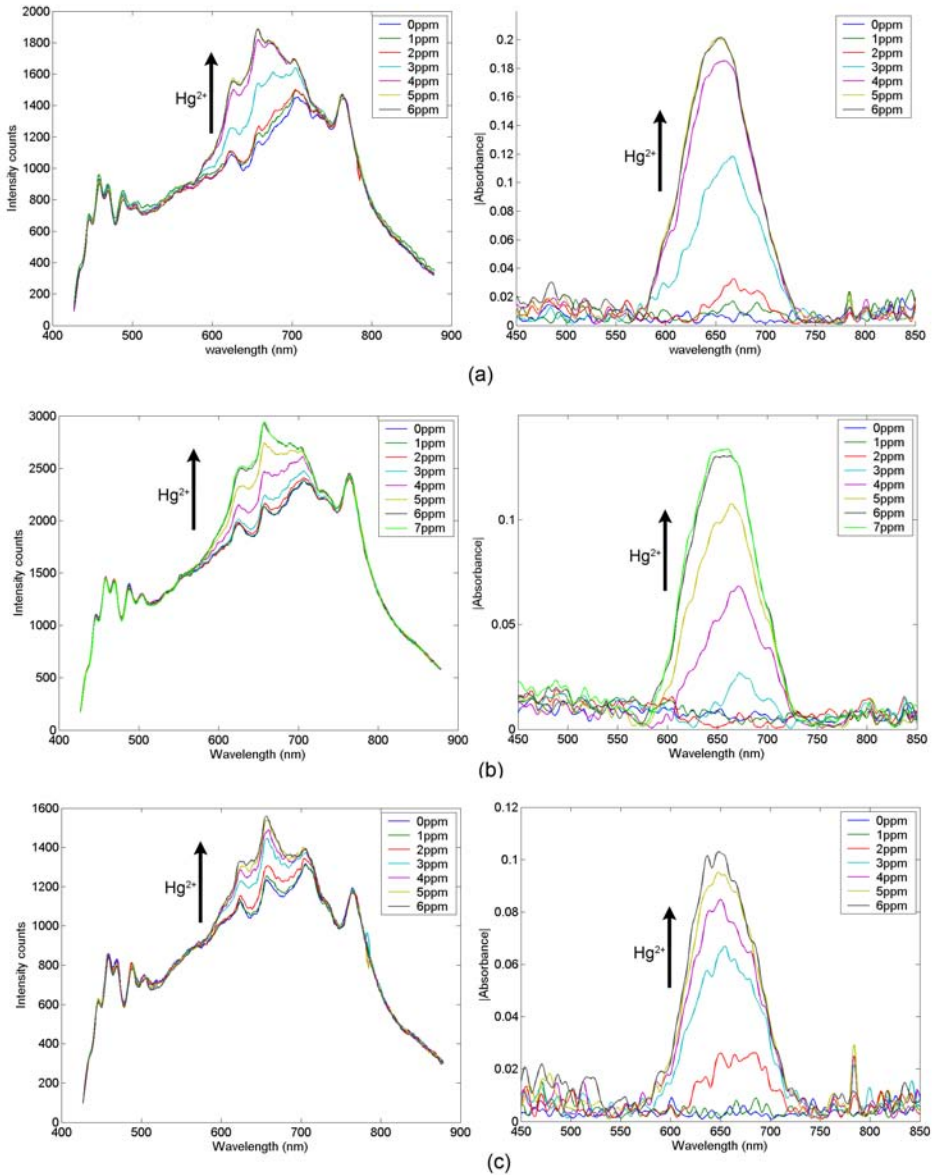


Figure 5.11. a), b) and c) represents the intensity counts (on the left) and their absolute spectra absorbance (on the right) corresponding to three different mercury probes with the same fabrication conditions. After the conditioning time of 45 minutes immersed in buffered water (pH 7) for each optode, the mercury additions have been carried out with an interval time between measurements of five minutes.

Therefore, in order to calibrate the mercury probes PLS processing was carried out. As the analytical signal, the intensity counts response was selected because it contains more relevant information, which can serve to predict mercury concentrations. Precisely, the spectral variables arises from 525 to 780 nm, which contains the most significant optical changes when mercury is present, and also it includes invariant regions that can serve as reference signal for the PLS model. A moving average filter was applied in order to smooth out the high frequency fluctuations. The moving average is similar to the low pass filter whereby each element is replaced by the average of a certain number N of neighbouring elements.

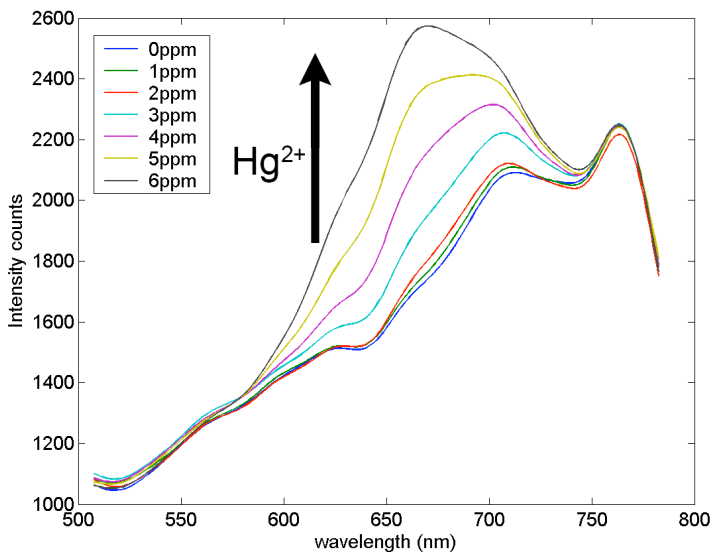


Figure 5.12. Smoothed spectral mercury response of an optode used in the calibration of the mercury probes.

The difference equation of this process is defined by

$$y(k) = \frac{1}{2N+1} [y(i+N) + y(i+N-1) + \dots + y(i-N)] \quad (5.5)$$

where $y(k)$ is the smoothed value for element k corresponding to the whole elements within the span $2N+1$. In practice, this difference equation is easily programmable with MATLAB as a convolution with a finite impulse response filter (FIR), wherein the vectors are ones. Figure 5.12 shows the smoothed spectral response of a mercury probe obtained considering a filter span of 20 elements.

The construction of the PLS model was carried out with the mercury responses from six optical fiber mercury probes. Mercury titrations were performed for each optode in a concentration range from 0 to 6 ppm of Hg^{2+} . The whole calibration data was composed by 44 measurements and 291 spectral variables, which resulted after decimating by a factor of 5.

The behaviour of the PLS model was observed with other 3 N719/ Al_2O_3 optical fiber probes which had not involved in the calibration process. One of these probes was used for training the model and choosing the correct number of PLS factors. The other two probes were used to validate the PLS model with new mercury samples. Herein, the adjustment and evaluation criterion applied was similar to PLS modelling in previous chapters. Figure 5.13 shows the mercury predictions of the PLS model corresponding to training and validation measurements. A

good fitting was achieved for the training probe response considering 4 PLS factors. The root mean square error of prediction percent (% RMSEP) for the other two mercury probes was 11.56 (%) was achieved, considering a mercury measurement range of 0-6 ppm. Moreover, statistical feature selection pre-treatment was also applied. The discrimination factor plot showed a unique peak localized at 665 nm. Several Gaussian kernels with different σ were applied, but any reduction of the spectral variable set assisted by SFS did not improve the performance of the PLS model. As in Chapter 4, the performance of the direct PLS model was more robust when the variance was mainly caused by the fabrication procedure.

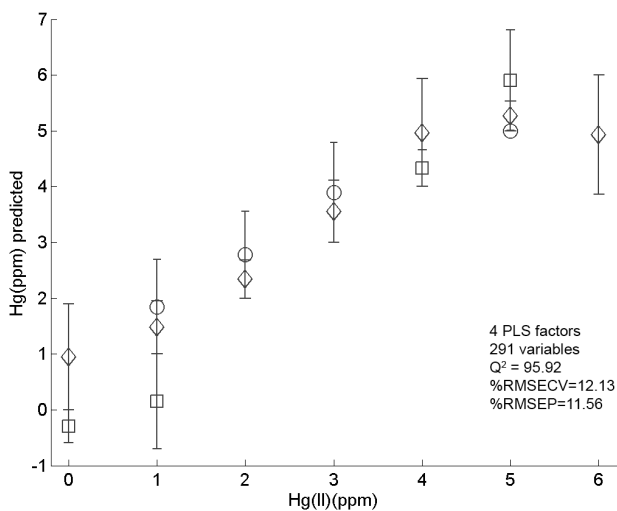


Figure 5.13. Mercury predictions of the PLS model with 4 PLS factors from three different optical fiber probes: (\diamond) training data set, (\circ) validation data set 1, (\square) validation data set 2.

As discussed above, the optical response of this kind of sensors show a remarked dependence on the cladding homogeneity. Any variation regarding thickness, particle distribution, porosity, humidity,

contamination due to dust particles, etc, may cause variations in the response among probes. Therefore, it is of utmost importance that the manufacture process be directed to reducing all these factors that may introduce changes in the sensitive layer. Many of these factors are not considered in the usual laboratory conditions, unless all steps of the manufacture process are performed inside a special room that can guarantee a clean and controlled environment. Moreover, the fact that the probe does not show an optimal regeneration, forces a single use of the probes, thus making it necessary to obtain a generic model with a greater error instead of a tailored individual calibration model for each probe, which could be obtained from repetitive measures. Even though, the mercury predictions yielded by the PLS model present a good linearity regarding the real mercury values, making it possible to obtain a general calibration model that allows to quantify the response of new probes. Future improvements of this system, aimed to broaden its applicability, should be directed to enhance the system sensitivity or to increase the dynamic range. These factors are directly related to the concentration of the adsorbed indicator. However, this parameter cannot be increased to a considerable extent, as there is a balance between the dye concentration and the stability of the probe response. It still remains to explore the film thickness and the nanoparticle diameter, which parameters are more closely related to the analyte diffusion through the film, and which could have impact over the sensitivity and measurement range.

5.5 References

- (1) Stewart, G.; Culshaw, B. *Optical and Quantum Electronics* **1994**, *26*, 249-259.
- (2) Veldhuis, G. J.; Parriaux, O.; Hoekstra, W. M.; Lambeck, P. V. *Journal of Lightwave Technology* **2000**, *18*, 677-682.
- (3) Snyder, A. W. *Optical Waveguide Theory*; Chapman and Hall: London, **1983**.
- (4) Bunganaen, Y.; Lamb, D. W. *Journal of Physics: Conference Series* **2005**, *15*, 67-73.
- (5) Chartier, G. *Introduction to Optics*; Springer: Grenoble, France, **1997**, 359.
- (6) Bansal, L., Drexel University, **2004**.
- (7) Keller, B. K.; DeGrandpre, M. D.; Palmer, C. P. *Sensors and Actuators, B: Chemical* **2007**, *B125*, 360-371.
- (8) French, R. H.; Mullejans, H.; Jones, D. J. *Journal of the American Ceramic Society* **1998**, *81*, 2549-2557.
- (9) Yuan, J.; El-Sherif, M. A. *IEEE Sensors Journal* **2003**, *3*, 5-12.
- (10) Janotta, M.; Karlowatz, M.; Vogt, F.; Mizaikoff, B. *Analytica Chimica Acta* **2003**, *496*, 399-348.
- (11) Moreno, J.; Arregui, F. J.; Matias, I. R. *Sensors and Actuators, B: Chemical* **2005**, *B105*, 419-424.
- (12) Crisp, J. *Introduction to Fiber Optics*; Reed Educational and Professional Publishing Ltd: Oxford, **2001**.

- (13) Elosua, C.; Matias, I. R.; Bariain, C.; Arregui, F. J. *Sensors* **2006**, *6*, 1616-1678.
- (14) Alabbas, S. H.; Ashworth, D. C.; Narayanaswamy, R. *Analytical Proceedings* **1989**, *26*, 373-375.

UNIVERSITAT ROVIRA I VIRGILI


DEVELOPMENT OF AN OPTICAL FIBER PROBE FOR MERCURY DETECTION

Javier Pérez Hernández

ISBN: 978-84-691-9474-4/DL-T-2205-2008.

218

Development of an optical fiber probe for mercury detection



6 Conclusions

6. Conclusions

Nowadays, much increasing research efforts are devoted on the chemical sensor field. Although chromogenic probes have been popular in last decades, the molecular design tends to use fluorescence detection systems, often combined with recent advanced materials, such as quantum dots. In general, the fluorimetric detection provides higher sensitivities. However, the use of this type of molecules involves certain working constrictions; for example, working in aqueous solution may not be feasible because the fluorescence of some molecules is only possible with organic solvents. Moreover, the attachment of the molecule to an optical support may change its emission properties. In contrast to this kind of sensors, colorimetric sensors are widely used in combination with supporting matrices and with simpler and low cost measurement instrumentation. Accordingly, N719 dye has been selected because of its suitable affinity to mercury, its wide spectral response and the possibility of being anchored onto metal oxide films, making its integration into an optical device feasible.

An important part of this thesis has been dedicated to multivariate analysis of spectral data. A number of pre-processing techniques coupled to a defined calibration method have been applied, showing that it is feasible to reduce the effect of chemical interferences present when using a molecular probe. In this context, concentrations of mercury from 0 to 2

mg L⁻¹ have been quantified even in the presence of 19.5 mg L⁻¹ of interferential metals. In order to improve the prediction ability of PLS calibration models, a comparison of several pre-treatment techniques has been carried out, all these methods being tested and validated on the same data sets. The results showed that the lower prediction error was obtained by employing variable selection techniques. Indeed, we have demonstrated that the variable selection can overcome interference effects in the mercury quantification. Initially, the genetic algorithm was expected to be the best technique of this group. However, the adjustment of the algorithm towards an optimal solution with less over-fitting was tedious and entailed long computation times (around 20 minutes) if compared to the above-mentioned SFS adjustment (0.26 seconds). On the other hand, the use of statistical feature selection to identify important spectral features provided for the best performance of the PLS calibration model. Moreover, the approach of using Gaussian kernels, together with the SFS algorithm, allowed a considerable reduction of the number of variables to be selected, having a crucial impact on the quality of the final PLS model. Similarly, the extension of the SFS to bi-variate analysis enabled the variable selection technique to identify synergic variables, which also resulted in a low prediction error. A further advantage, of the statistical feature selection approach, relies in its simplicity and very low computational cost. The results of this work can be extended to a wide variety of chemical probes, improving their robustness in quantification tasks. The results also show the potential use

of this particular chemical probe for the production of a chemosensor that would be highly selective to mercury.

On the other hand, great advances have been achieved by immobilizing the indicator on a solid support. Although N719 is susceptible of being anchored onto TiO₂ films, this support is not suitable for measuring mercury in aqueous solution because leaching problems occur upon exposure to water. Herein, we have demonstrated a great improvement by immobilizing the indicator onto Al₂O₃ nanoparticles films. This material is optically more transparent than titania films, and on the other hand its high surface area allows a better control of the dye concentration in the mesoporous films. Higher mercury levels could be detected by increasing the concentration of indicator adsorbed onto the films. The stability in water has been improved by changing the acidity conditions of the film. Among the several acid treatments tested, the choice of sulphuric acid showed a superior performance in terms of reagent leakage, while maintaining the sensitivity performance of the N719/Al₂O₃ films. However, the lack of reversibility reduces the possibility of online mercury monitoring and forces to make a single use of the sensitive film. Nevertheless, the dye of the alumina support can be renewed by a first immersion of the film in a basic solution (for example NaOH solution at pH 10), and a subsequent immersion in a N719 ethanol solution. The calibration of the Al₂O₃ films showed a good correlation with mercury concentrations, even in the presence of most important interferential metal ions. These results corroborate a similar behaviour as

the experiments in liquid solutions, and thus the adsorption onto alumina films is innocuous to the mercury binding. In this set of experiments, there is a great variance introduced by the error of reproducibility of the films. Under these circumstances, the direct PLS solution has provided for the best fitting to mercury predictions. The better performance of the PLS model with the whole spectral variables concludes that a higher variable number shall be recommended when a great signal variance is present. Furthermore, several deposition techniques are compatible with this alumina paste, such as screen-printing, spin coating and dip coating, what makes the production of different types of optical sensors feasible.

This is the first time that an optical fiber probe based on a functionalized cladding for mercury(II) determination in water samples has been obtained. This novel type of optical probe allows a high level of integration of the molecular indicator, whereby the measurement process is further simplified. A simple and low cost fabrication procedure makes the N719/ Al_2O_3 films suitable to be sensitive towards mercury. By using the alumina cladding, we have observed an unusual situation in the literature, related to the fact that the outer cladding has a refractive index greater than the optical core, what may give rise to the combination of evanescent field and radiative mode. A similar response time has been observed regarding the sensitive films supported onto glass, but with a different spectral response when compared to the direct absorbance measurements of the sensitised films. The narrower spectral range and the peak shift in the optical fiber implementation may be due to an

attenuation of the most significant spectral regions of the N719. In this sense, the sensitivity is not enhanced as it was expected with this type of optical fiber design. The mercury response between different sensors have significant variance, but applying PLS calibration the reproducibility error is reduced, allowing a mercury prediction error of 11.5 per cent. Some problems are still to be solved regarding the sensitivity and reproducibility. There are many variables involved in the optical fiber probe design, which will require to set some of those parameters in order to discern the principle-of-proof in the experiment. Moreover, further studies can be performed in order to observe the particle size and thickness of the alumina thin film and its role regarding sensitivity. Finally, the application of this optical fiber implementation to mercury screening in food, wherein the sensitivity requirements are minor, is feasible.